University of Bath

CONTROL OF LOW REYNOLDS NUMBER FLOWS BY MEANS OF FLUID-STRUCTURE INTERACTIONS

I. Gursul, D.J. Cleaver, Z. Wang
University of Bath
Department of Mechanical Engineering
Bath BA2 7AY, United Kingdom

ABSTRACT

There is great interest in small aircraft known as Micro Air Vehicles and mini Unmanned Air Vehicles due to the wide range of possible applications. This article reviews recent work that aims to exploit the flexibility of the wing structure in order to increase lift and thrust, and delay stall. Wing flexibility has often been considered to be unwanted for large conventional aircraft and measures are taken to limit the deformation. In contrast, very small aircraft flying at low speeds are not necessarily subject to the same limitation. This approach is only applicable to small aircraft because the frequencies of the wing structure and fluid flow instabilities are close to each other. Consequently, small amplitude and high-frequency motions will be considered.

We first start with rigid airfoils and wings in forced plunging motion, which mimics the bending oscillations. The main advantage of this approach is the freedom to vary the frequency within a wide range. Two mechanisms of high-lift production on the oscillating rigid airfoils are discussed. In the first one, leading-edge vortex dynamics and different modes of vortex topology play an important role on the time-averaged lift and thrust at post-stall angles of attack. Existence of optimal frequencies and amplitudes are demonstrated, and their relation to other phenomena is discussed. In the second mechanism of high-lift, trailing-edge vortex dynamics leads to bifurcated/asymmetric flows at pre-stall angles of attack. Deflected wakes can lead to time-averaged lift coefficients higher than those for the first mechanism. Some aspects of lift enhancement can be sensitive to the airfoil shape. For three-dimensional finite wings, lift enhancement due to the leading-edge vortices and existence of optimal frequencies are similar to the two-dimensional case. Vortex dynamics of the leading-edge vortex and tip vortex is discussed in detail. Leading-edge sweep is shown to be beneficial in the reattachment of the separated flows over oscillating wings. Oscillating flexible wings can provide much higher lift coefficient than the rigid ones. Amplitude and

phase variation in the spanwise direction result in much stronger leading-edge and tip vortices. Self-excited vibrations of flexible wings, including membrane wings, can excite shear layer instabilities, an thus delay stall and increase lift. Finally, thrust enhancement or drag reduction can be achieved by employing chordwise and spanwise flexibility. The effects of wing flexibility on the vortices and thrust/drag are discussed in relation to the characteristics of wing deformation.

CONTENTS

NOMENCLATURE

a amplitude of plunging motion

A peak-to-peak amplitude, $2a$

b span

c chord length

C_d time-averaged drag coefficient

C_l time-averaged lift coefficient of airfoil

$\hat{C}_l$ time-averaged modified lift coefficient

C_{l0} time-averaged lift coefficient of stationary airfoil/wing

C_L time-averaged lift coefficient of wing

C_T time-averaged thrust coefficient of airfoil/wing

d distance between vortices; depth

E modulus of elasticity

f frequency

h dimensionless plunging amplitude, a/c

I second moment of area

k_G Garrick reduced frequency, $\pi fc/U_\infty$

L_{TED} length of trailing-edge plate

Q Q-criterion

Re Reynolds number

s instantaneous displacement of plunging airfoil

S wing reference area

Sr_c Strouhal number based on chord length, fc/U_∞

Sr_A Strouhal number based on amplitude, fA/U_∞

sAR semi-aspect ratio

t time; thickness

T period

u streamwise velocity

U_∞ free stream velocity

U_{pl} maximum plunge velocity, $2\pi fa$

v cross-stream velocity

V magnitude of velocity in the measurement plane

x streamwise or chordwise distance

y	cross-stream distance
z	spanwise distance
α	angle of attack
δ	flap angle
ϕ	roll angle
λ	dimensionless aeroelastic parameter
θ	pitch angle; phase angle
ρ	density
ω	vorticity
Γ	circulation
Λ	sweep angle

1. Introduction

Recent advances in micro-technology have created an opportunity to mount miniature surveillance equipment on small (wing span less than 15 cm) flying aircraft known as Micro Air Vehicles (MAVs). Such micro-technology includes tiny CCD cameras, infra-red sensors, and computer-chip sized hazard detectors. Micro-flying robots could be suitable for reconnaissance and surveillance, as well as numerous other applications such as coastal surveillance, crop monitoring, telecommunications, news broadcasting, remote sensing and mineral exploration. MAVs have similar dimensions to birds and insects, and similar Reynolds numbers. Mini Unmanned Air Vehicles (UAVs) are slightly larger, with correspondingly larger Reynolds numbers.

As the length scale of small aircraft is small and flight speed is low, the Reynolds number is low, typically $Re = 10^3 - 10^5$. At these low Reynolds numbers, separated and vortical flows are dominant, making lift and thrust generation challenging due to the strong viscous effects as discussed in recent review articles [1-4]. Because of the poor lift generation in cruise flight, it will be necessary for fixed-wing MAVs to fly at relatively high angles of attack, close to stall conditions. In addition, it may be necessary to fly in the poststall regime during vertical gusts. Hence, the delay of stall is necessary for stable MAV flight. High angle of attack flows with large separated regions are also typical for flapping-wing MAVs. Leading-edge vortices are known to enhance lift in unsteady aerodynamics. Periodic excitation of the flow to generate leading-edge vortices for fixed-wing MAVs is therefore a sensible approach.

Consequently, active flow control will be necessary. This can be achieved by means of unsteady blowing, suction, moving surfaces, and plasma actuators. However, these conventional flow control techniques such as blowing are not necessarily practical at these small scales, and often, the space available is insufficient to place actuators or blowing chambers. In addition, weight, volume and power consumption of the potential actuation systems need to be considered. For example, plasma actuators, when the power supply is considered, may not be practical at these small scales. In this review article, we focus on the periodic excitation of separated flows by means of wing oscillations. Fluid-structure interactions can be exploited to control the separated flows, and thus increase lift and delay stall. Small aircraft are inherently light weight and flexible, hence vibrations of the wings can be used to excite the separated flows.

1.1. Frequencies of fluid instabilities and wing structure

Extensive research on active flow control of separated flows around airfoils and wings has shown that partial or full reattachment is possible when the inherent instabilities in the separated flow are excited [5]. Depending on the airfoil shape and excitation characteristics, at least three different instabilities may be important for effective excitation: 1) initial shear layer instability or its subharmonics, although this appears to be more effective for delta wings [6]; 2) instability of the separation bubble [7]; and 3) wake instability [8,9]. Flow control research on separated flows suggests that the optimal Strouhal number of unsteady excitation is on the order of unity, $fc/U_\infty = O(1)$. Typically, the frequencies of the instability of the separation bubble and wake instability are on this order of magnitude. An alternative control strategy relying on much higher frequencies was discussed by Glezer *et al.* [10].

Figure 1 shows the qualitative variation of the frequency of the fluid instabilities (corresponding to $fc/U_\infty = O(1)$) as a function of wing span. As the wing span increases from very small (MAVs) to large (civil transport aircraft), the frequency of flow instabilities does not vary much once variations in the wing chord length and flight speed are taken into account. Also shown on Figure 1 is the qualitative variation of the natural frequency of the wing structure. It decreases substantially with increasing wing span. For a typical civil transport, the structural frequency may be on the order of few Hertz, while typically this quantity is on the order of 10^2 Hertz for micro air vehicles. As illustrated in Figure 1, structural frequencies and fluid instability frequencies are therefore close to each other for small aircraft. This presents an opportunity to exploit wing vibrations for flow control purposes. For small aircraft, small-amplitude wing vibrations could potentially excite characteristic frequencies of the fluid instabilities.

While one tries to suppress the vibrations for large aircraft because of fatigue and passenger comfort issues, this requirement is not necessary for small aircraft (MAVs), because they have limited (much shorter) life time and no passengers. Thus, exploiting the flexibility of the wing structure to excite the fluid for flow control becomes a possibility at low Reynolds numbers. In practical applications, this technique can be achieved by the torsional (pitching) and bending (plunging) vibrations of flexible wings by means of piezoelectric actuators and/or elastic mounting of rigid wings. For example, if a torsional spring used for mounting is tuned correctly, airfoil/wing oscillations are easier to produce. External excitation at

resonant structural frequencies for less power input or self-excited wing vibrations for zero power input can also be considered.

1.2. Small-amplitude high-frequency oscillations

As the main objective is to exploit the fluid-structure interactions for flow control, naturally small-amplitude and high-frequency wing oscillations are relevant. Here we will discuss the range of dimensionless parameters and compare with the biological flows where pitching and plunging motions are observed [11-13]. The first parameter is the Strouhal number based on the chord length,

$$Sr_c = f c / U_\infty \tag{1}$$

which can be considered as the ratio of two time scales (convective time unit and the period of the motion). Since it is related to the convection of the leading-edge vortices, this parameter is important in determining the unsteady lift. In biological flows, one observes large amplitude motion (amplitude on the order of chord length, $a/c = O(1)$) at low frequencies (Strouhal number based on the chord length, $Sr_c = fc/U_\infty = O(10^{-1})$). However, in our case, we have small amplitude motion ($a/c = O(10^{-1})$) at high frequency (Strouhal number, $Sr_c = fc/U_\infty = O(1)$). Hence, the kinematics is very different from the biological flows.

The second parameter is more relevant to the thrust generation. The history of the subject is given in the review article by Platzer *et al.* [14]. It has been shown that the most important parameter for thrust generation is the Strouhal number based on the amplitude, which is defined as:

$$Sr_A = f A / U_\infty, \tag{2}$$

where A is the peak-to-peak amplitude of the trailing-edge. This parameter can also be considered as normalized plunge velocity. It is also related to the maximum effective angle of attack $\alpha_{eff,\,max}$, through:

$$\alpha_{eff,\max} = \alpha + \tan^{-1} \frac{U_{pl}}{U_\infty} = \alpha + \tan^{-1} \frac{2\pi f a}{U_\infty} = \alpha + \tan^{-1} \pi Sr_A \tag{3}$$

where U_{pl} is the maximum plunge velocity. Interestingly, Strouhal number based on the amplitude, $Sr_A = fA/U_\infty$, which is a measure of the change in the effective angle of attack due to the unsteady motion, is similar in nature and our case.

Even though the flows that we are interested in are very different from biologically inspired flows, we note that the flexibility of the wings in insects and birds has been documented [15,16]. There is a belief among biologists that wing flexibility improves the aerodynamics [17,18]. Therefore, even though the kinematics of the biological flows and flows of our interest are very different, we share the same goal, which is performance improvement by means of flexibility.

The outline of this article is as follows: we first start with rigid airfoils in forced plunging motion. As the frequency of the plunging motion is varied, we identify and discuss various modes of vortex topology and two different mechanisms of high-lift production. Then, finite rigid wings in oscillatory motion are discussed. Next, vortex dynamics and lift production are reviewed for oscillating flexible wings, followed by the self-excited vibrations of flexible wings and membrane wings. Finally, thrust enhancement or drag reduction using chordwise and spanwise flexibility are discussed.

2. Lift enhancement of oscillating rigid airfoils

2.1. Two mechanisms of high-lift

Figure 2 illustrates two high-lift mechanisms for an airfoil oscillating with small amplitude: a) leading-edge vortices for post-stall angles of attack; b) deflected trailing-edge vortices for pre-stall angles of attack. In the first mechanism, the flow is fully separated at the leading-edge for the stationary airfoil, and therefore part of the suction is lost. For the oscillating airfoil, the LEV is produced during the downstroke and once formed it is convected over the upper surface creating a low-pressure wave as it passes. Extremely small amplitude oscillations of a SD7003 airfoil at a post-stall incidence have been shown to increase the time-averaged lift [19]. Furthermore, small amplitude airfoil oscillations for a NACA0012 airfoil [20] and a flat plate airfoil [21] at a post-stall incidence have also been studied. Various experimental methods including particle image velocimetry (PIV) measurements and force measurements were combined with high-fidelity simulations. These findings highlighted the delay of stall and lift enhancement on oscillating airfoils, and also identified an interesting phenomenon due to a strong interaction between the airfoil and vortex. In this new mode of vortex topology, a leading-edge vortex is generated during the downward motion of the airfoil and then impinges on the upward moving airfoil, resulting in rapid loss of its coherency. As a result in this flow regime no coherent vortices are convected

downstream over the suction surface of the airfoil, which has a considerable effect on the aerodynamic forces.

In the second mechanism shown in Figure 2, asymmetric wake flow can be observed at even zero angle of attack if the Strouhal number is sufficiently high. This asymmetric flow generates the time-averaged lift. For the zero mean angle of attack, various studies of plunging airfoils [22-26] and pitching airfoils [27-29] showed that asymmetric wake flows are possible at high Strouhal numbers. Emblemsvag et al. [27] was the first to suggest that, at high frequencies, the vortices tend to shed in pairs (vortex dipoles) and this triggers the deflected wakes. Hence, the formation of dipoles is important as the distance between the vortices decrease and strength of the vortices increase with increasing frequency. A symmetry breaking criterion, based on a simple model of a dipole and its self-induced velocity, was suggested by Godoy-Diana et al. [29]. The model was developed based on the measured strength of the vortices and the phase velocity of the vortex street for zero mean angle of attack. Cleaver et al. [30] showed that deflected flows are possible up to the stall angle, resulting in very high time-averaged lift coefficients. The details of these two high-lift mechanisms are discussed below.

2.2. Leading-edge vortices

Figure 3 shows the variation of the time-averaged lift coefficient as a function of Strouhal number based on the chord length for a NACA 0012 airfoil at a post-stall angle of attack of 15 degrees at a Reynolds number of 10,000 for different amplitudes [20]. It is seen that significant lift enhancement is possible, which increases with increasing amplitude until a critical high frequency is reached. The sudden drop in the lift for larger amplitudes will be discussed below. Up to $Sr_c \approx 0.5$, the increase in the time-averaged lift is monotonic, and, in fact, it has been shown that the lift increase is approximately proportional to the Strouhal number based on the amplitude [20]. At around $Sr_c \approx 0.5$, there is a local maximum, which is visible for almost all amplitudes. For the largest amplitude $a/c = 0.20$, the lift coefficient is also given for $Re = 20,000$ for the same airfoil in Figure 3. The same peak has been found, revealing no effect of Reynolds number. In Figure 3, the second peak around $Sr_c \approx 1.0$ and the third peak around $Sr_c \approx 2.0$ are also visible. We note that a peak was observed at a Strouhal number of $Sr_c \approx 0.4$ in the direct numerical simulations of Andro and Jacquin [31] for a plunging NACA 0012 airfoil at $Re = 1,000$. In their case, the peak was attributed to an

optimal interaction of the leading-edge vortices with the airfoil. We shall return to the physical mechanisms behind these peaks later on.

Figure 4(a) presents the streamlines and the magnitude of the total velocity vector for the stationary NACA 0012 airfoil at a post-stall angle of attack of 15 degrees for Re = 10,000. The large region of separation becomes much smaller when the airfoil is plunged periodically with small amplitude as shown in Figure 4(b). With increasing Strouhal number, the flow becomes more attached, leading to increased lift as well as reduced drag in agreement with the direct force measurements shown in Figure 3. In fact, at high Strouhal numbers, a time-averaged jet is formed downstream of the trailing-edge, which indicates thrust generation.

Figure 5 shows the vorticity in the phase-averaged flow field at the top and bottom of the plunging motion for different Strouhal numbers. For the Strouhal numbers less than 2.5 shown in the figure, the main feature is the generation of leading-edge vortices during the downward motion and their subsequent convection downstream. Other features such as generation of secondary vortex of opposite sign and vortex interactions and merging in the wake are less important. Consequently we call this type of flow: *mode-1*, where the LEV is basically convected. Figure 5(e) shows a *mode-2* flow field. Here the LEV is formed during the downward motion and loses its coherency entirely during the upward motion due to the impingement with the airfoil. This form of flow field (no convected LEV) does not arise abruptly; Figure 5(d) shows a mixed mode. A time history of a mode-2 vortex flow is presented more clearly in Figure 6 for a larger plunge amplitude (a/c = 0.10). The dramatic vortex-airfoil interaction and loss of vortex coherency are visible during the upward motion of the airfoil.

Figure 7 shows the boundary between the mode-1 and mode-2 in the amplitude-Strouhal number plane. The boundary is illustrated as a shaded region, where the flow field is of mixed mode (there is a discernible convected LEV, but it is very weak). Different vortex topologies in mode-1 and mode-2 flow fields affect the time-averaged forces significantly. It is seen that the boundary region matches zero time-averaged drag as determined by direct force measurements. In mode-1 region there is drag, while mode-2 region generates thrust. Also, there is usually high-lift in mode-1, but low-lift in mode-2. In Figure 7, lines of constant maximum effective angle of attack are shown, which can also be considered as the lines of constant plunge velocity (or Strouhal number based on the amplitude), as discussed

with Equations (2) and (3) earlier. Since the mode-switch band occurs in the approximate range of $\alpha_{\text{eff,max}} = 48°$ to $\alpha_{\text{eff,max}} = 68°$, or alternatively $Sr_A = 0.20$ to $Sr_A = 0.43$, one can conclude that the mode-switch does not bear a strong correlation with either constant effective angle of attack or constant Strouhal number based on amplitude. So in a similar manner to the observations of Young and Lai [32] for drag, neutral and thrust wakes, wake structure regions do not follow lines of constant Strouhal number based on amplitude.

It is interesting to consider the time-averaged lift in the amplitude-Strouhal number plane, and relate this to the mode-1 and mode-2 flows. As the frequency (Strouhal number based on the chord length) or amplitude is increased, the plunge velocity (or "excitation" velocity) is also increased. Therefore, excitation level is not constant when either the frequency or amplitude is varied. In order to take this into account, we define a modified lift coefficient based on the vector sum of the free stream velocity and maximum plunge velocity:

$$\hat{C}_l = \frac{L}{\frac{1}{2}\rho(U_\infty^2 + U_{pl}^2)c} \tag{4}$$

Figure 8 shows a contour plot of the modified lift normalized by the lift coefficient of the stationary airfoil, as a function of amplitude and Strouhal number based on the chord length. The most apparent feature of Figure 8 is the existence of three regions of optimal excitation with their Strouhal number ranges centered around $Sr_c = 0.5$, 1.0, and 2.0. It is interesting that the three regions are located on a constant plunge velocity of $U_{pl}/U_\infty = 0.5$ shown with a dashed line in Figure 8. Hence, the optimum plunge velocity is approximately half the free stream velocity. The band shown with the two solid lines is the same region that separates mode-1 and mode-2 flow fields as discussed earlier. Hence, all three optimal operating conditions have a mode-1 flow field, confirming that convected leading-edge vortices provide the most efficient conditions for maximizing the time-averaged lift. Hence the mode-2 flow field is associated with a loss of lift.

Returning to the frequency range of the optimal excitation conditions shown in Figure 8, there is a close relation to the natural shedding frequency measured in the wake [20]. The measurements suggest that the optimal frequencies are related to the fundamental, subharmonic and the first harmonic of the natural shedding frequency. This is agreement with earlier observations of the vortex lock-in phenomenon in the wakes of the stalled airfoils [8,9]. One expects that when oscillated at the natural shedding frequency, its harmonics or

11

subharmonics, the wake becomes more ordered and synchronized, with an increased spanwise correlation of the flow, in a similar manner to vortex lock-in of oscillating cylinders [33]. This was confirmed for the periodically plunging airfoil at a post-stall incidence [20].

Finally, we return to the sudden drop of the time-averaged lift for larger amplitudes in Figure 3. It is seen in Figure 9 that, at high Strouhal numbers, a lower-surface leading-edge vortex forms. This is best illustrated in Figure 9(d) for the largest Strouhal number. The lower-surface vortex strengthens rapidly with increasing Strouhal number, and becomes nearly equal to the circulation of the upper-surface vortex [20]. As the low pressure region induced by the lower-surface vortex counteracts the lift, we observe a decrease in the lift. It is interesting that the time-averaged lift coefficient returns to the level of a stationary airfoil.

2.3. Bifurcated/asymmetric flows

For zero mean angle of attack at high Strouhal numbers, the symmetry may be broken by deflected jets. Figure 10 shows the transition towards symmetry breaking with increasing Strouhal number. Thus there is the possibility of asymmetric flow fields and non-zero lift even at zero angle of attack. As this phenomenon is related to the formation of vortex dipoles, it is believed that the trailing edge vortices alone are responsible for deflected jets and any criteria should be derived from their properties. This is supported by the results of Jones *et al.* [22], who simulated deflected jets with an inviscid unsteady panel code, where no leading-edge vortex exists because separation is not modelled. We will show later on that there may be an effect of the leading-edge vortex in determining the stability of certain cases. It was found that the direction of the deflection (upwards or downwards) is determined by the sign of the starting vortex when the airfoil starts to move up or down [22]. For non-zero mean angles of attack, it also depends on the angle of attack [30], indicating that starting vortex as well as the bound vortex play a role. Usually a stable deflected flow field is established within a couple of plunge cycles.

Figure 11 shows the time-averaged lift coefficient [30] for various angles of attack in the range 0° to 20° for *a/c* = 0.15. For angles of attack less than or equal to the stall angle (10° in this case), at high Strouhal numbers, significant bifurcations are observed in the time-averaged lift coefficient resulting in two lift coefficient branches. The upper branch is associated with an upwards deflected jet, and the lower branch is associated with a downwards deflected jet. These branches are stable and highly repeatable, and are achieved

by increasing or decreasing the frequency in the experiments. Increasing frequency (solid line) refers to starting from stationary and increasing the frequency very slowly (while waiting for the flow to reach a stable asymptotic state after each change in frequency); decreasing frequency (dashed line) refers to impulsively starting at the maximum frequency and decreasing the frequency very slowly. The upper branch is termed *mode A* and the lower branch is termed *mode B*. It is seen that, when there are two branches, the lift coefficient for mode A can be very high, in fact higher than those due to the leading-edge vortices discussed previously. The lift coefficient is the same for increasing and decreasing frequency for Strouhal numbers less than the bifurcation point. For angles of attack larger than the stall angle, there are no longer distinct branches and the lift for both increasing and decreasing frequency matches.

Shown in Figure 12 is time-averaged velocity for typical pre-bifurcation, mode A and mode B flow fields at zero angle of attack. The pre-bifurcation flow field in Figure 12(a) shows a jet aligned horizontally, whereas Figure 12 (b) and (c) reveal deflected jets. For mode A, the time-averaged jet is deflected upwards and there is a high-velocity region over the upper surface, while for mode B the inverse is true. The time-averaged lift data shown in Figure 11 and the time-averaged velocity in Figure 12 reveal that the lift direction is the same as the direction of the vertical component of the deflected jet, i.e., mode A is associated woth positive lift and mode B with negative lift. This is consistent with the simulations performed at much lower Reynolds numbers [26,27]. This relationship between the direction of the lift and deflected jet is contrary to what one would intuitively expect. In a simple control volume analysis applied to the measurement domain shown in Figure 12(c), Cleaver *et al.* [30] demonstrated that momentum flux terms are small compared to the measured lift, and therefore concluded that the time-averaged lift is dominated by the pressure difference resultant from the velocity difference over the upper and lower surfaces.

Figure 13 reveals the details of the vortex dipole formation. For mode A, a clockwise trailing-edge vortex (TEV) forms during the upward motion and loiters near the airfoil during the downward motion during which the counter-clockwise TEV forms. Due to the relative positions of the vortices, the resulting dipole has a self-induced velocity in the upwards direction, thereby creating an upwards deflected jet. For mode B, similar events occur but mirrored in the *x*-axis and phase-shifted by *T*/2. Due to the asymmetry of the flow near the trailing-edge, asymmetry is also created near the leading-edge. Mode A has a stronger upper-

surface LEV, which also explains the higher time-averaged velocity above the upper surface. For mode B, the inverse is true: stronger lower-surface LEV causes the higher time-averaged velocity over the lower surface.

For non-zero angles of attack, Figure 14 reveals that similar dual flows exist, which is expected based on the upper and lower branches of the time-averaged lift shown in Figure 11. Phase-averaged vorticity contours for mode A (left column) and mode B (right column) are qualitatively similar for $\alpha = 0°$, $5°$, and $10°$. There a slight increase in the distance between the vortices of the dipole with increasing angle of attack for mode A, while this effect appears to be very small for mode B. For other oscillation amplitudes, except for small values $a/c \leq 0.05$, bifurcation of the lift and the main features of the flow fields are similar, although bifurcation occurs at different Strouhal numbers based on the chord length. For small amplitudes ($a/c \leq 0.05$), bifurcation was not observed within the range of Strouhal numbers tested ($Sr_c \leq 3.0$). This is shown in Figure 15 in the amplitude-Strouhal number plane. Theoretically, bifurcation may be possible for very small amplitudes at very high Strouhal numbers, which are not reached in the experiments. The effect of geometric angle of attack on the boundary of the single/dual flow fields appears to be small. It is also seen that this boundary takes place in the thrust producing region.

As the bifurcation occurs at different Strouhal numbers based on the chord length for different amplitudes a/c, Strouhal number based on amplitude and effective angle of attack due to the plunging motion can be considered as alternative criteria. Figure 16 shows the variation of the maximum and minimum effective angles of attack as a function of Strouhal number based on the amplitude. The bifurcation points for different oscillation amplitudes are shown on the diagram. It is seen that there is some correlation: the onset of bifurcation fall within the range $Sr_A = 0.45 \pm 0.07$ and $\alpha_{eff, max} = 60° \pm 9°$. However, these criteria cannot explain why there is no bifurcation at larger angle of attack and also for small oscillation amplitudes. In a similar manner to Godoy-Diana et al. [29] better correlations and insight can be derived from the measurements of the trailing-edge vortices. Cleaver et al. [30] found that, as the difference in the absolute value of the circulation of the clockwise and counter-clockwise vortices increases there is stronger trend towards a downwards deflected flow. This difference in circulation grows with increasing angle of attack. Thus, at a post-stall angle of attack $\alpha = 15°$, stronger counter-clockwise vortex and weaker clockwise vortex cause the

flow to be heavily biased towards a downwards deflected jet, and this is therefore the only mode that exists. Similarity of this single mode of the post-stall incidence to the mode B of the pre-stall incidences is shown in Figure 17. Given the very strong similarity, it is appropriate to classify this single flow field as a mode B. As asymmetry was identified as a key mechanism, a new parameter is suggested based on the angular velocity of a vortex pair [34]:

$$\frac{(\Gamma_{T+} + \Gamma_{T-})}{d^2} \tag{5}$$

where d is the distance between the vortices. This is made dimensionless as:

$$\frac{(\Gamma_{T+} + \Gamma_{T-})c}{U_\infty d^2} \tag{6}$$

This represents a non-dimensional TEV *asymmetry parameter*. The results of Clever *et al.* [30] suggest this parameter determines whether the time-averaged jet is deflected upwards or downwards.

A second parameter, which has been found to be important, is a strength parameter, derived from the average of the circulations of the TEVs. Figure 18 shows the data points in the plane of the asymmetry parameter versus this normalized circulation parameter. The horizontal line separates the single and dual flow modes. A vertical line separates mode A and mode B. If the circulation parameter is less than a critical value (for small amplitudes and frequencies), there is only one flow field. For larger values of circulation parameter, dual flows exist. If the asymmetry parameter is less than a critical value, mode A is generated. For larger values of the asymmetry parameter, only mode B is produced. At large angles of attack, the symmetry parameter is large even in the pre-bifurcation range. Indeed for $\alpha = 15°$, all of the data points are on the mode B side, making a mode B flow field the only possible outcome. Therefore mode B is selected as shown in Figure 18 for $\alpha = 15°$.

In Figure 19, the circulation parameter is defined based on the plunge velocity instead. It is seen that there is a clear boundary between the single and dual modes with minimal scatter of the data. The critical value of circulation normalized by plunge velocity is $\bar{\Gamma}/U_P c = 1.85$. The circulation normalized by the plunge velocity, $\Gamma/U_p c = \Gamma/(2\pi f a c)$, can be also interpreted as the inverse of a modified Strouhal number based on the dipole velocity Γ/a, the frequency and chord length.

2.4. Effect of airfoil shape

It was found that the airfoil shape has some effect on the two high-lift mechanisms (leading-edge vortices and asymmetric flows). For a post-stall angle of attack of 15 degrees, Figure 20 compares the time-averaged lift and drag coefficients for a NACA 0012 airfoil and a thin flat plate as a function of Strouhal number at different oscillation amplitudes [21]. For fixed-wing aircraft, thin airfoils are generally preferable at low Reynolds numbers [35]. It is seen in Figure 20 that there are strong similarities for the time-averaged lift [21]. The peaks in the lift and the Strouhal numbers at which these peaks occur are similar. This is consistent with earlier explanations of the origin of the peaks, namely, resonance with the wake instabilities. The wakes of stationary airfoils at post-stall angles of attack are likely to be similar as the flow separation takes place at the leading-edge. Comparable lift is produced for the flat plate up to a Strouhal number of unity, but after this, the lift decreases. There is an interesting difference for the time-averaged drag. While the thrust generation occurs for the NACA 0012 airfoil with increasing Strouhal number and amplitude, thrust is never produced for the flat plate.

These features can be understood by the comparison of the time-averaged velocity (Figure 21) and phase-averaged vorticity (Figure 22) for different Strouhal numbers. For a small amplitude $a/c = 0.025$, it is seen in Figure 21 that the time-averaged flows look similar for the two airfoils for Strouhal numbers up to $Sr_c = 1.0$. With increasing Strouhal number beyond this value, flow separation region becomes larger for the flat plate while separation almost disappears for the NACA 0012 airfoil. This trend is also visible in the phase-averaged vorticity fields shown in Figure 22. Particularly for $Sr_c \geq 2.0$, the leading-edge vortices are convected almost parallel to the free stream and much further away from the airfoil surface. This causes decreased lift and increased drag, and explains why thrust is never achieved.

For a larger amplitude of $a/c = 0.15$, a new phenomenon is observed as shown in Figure 23. In this figure, the vorticity fields are in a counter-clockwise loop starting at the top of the motion in the top left corner, moving down through the left column to the bottom of the motion in the bottom right, and then up through the right column back to the start. At $t/T = 0$ there is a clear, strong counter-clockwise lower surface LEV. This interacts with the boundary-layer to form clockwise vorticity. During the initial stages of the downward motion

(t/T = 0 to 2/12) this clockwise vorticity forms a vortex that pinches off by the point of maximum effective angle of attack (t/T = 3/12). This clockwise vortex pairs with the counter-clockwise to create a vortex dipole that convects away from the leading-edge in an upstream direction (t/T = 2/12 to 7/12). During this "vortex ejection" both vortices rapidly dissipate. This dissipation in the phase-averaged flow is an indication of the vortices becoming highly three-dimensional. This flow results in low lift and high drag. In contrast, this phenomenon was never observed for the NACA 0012 airfoil, and there is no sign of interaction between the upper- and lower-surface LEVs.

The second high-lift mechanism (asymmetric/bifurcated flows) was also investigated for the flat plate airfoil [21]. For zero angle of attack at high Strouhal numbers, the flat plate experiences deflected jets that are prone to periodic oscillations in direction, resulting in oscillation of the lift coefficient with a period on the order of 100 cycles. This is shown in Figure 24. Crosswise coordinates of the clockwise and counter-clockwise TEVs are shown in Figure 24(a) for the same phase (when the airfoil is at the bottom of motion) in each cycle. These phase-locked measurements show that the location of the vortices varies periodically. The circulation of these vortices also varies for the same phase in each cycle. The period of the oscillations is two orders of magnitude larger than the plunging period. It is interesting that this type of unstable jets was previously observed for rigid and flexible airfoils oscillating in still fluid [24] with a very similar oscillation period of around $100T$. As a result of these periodic switches in the direction of the jet, the lift force fluctuates. Figure 24(d) shows the variation of *period-averaged* lift coefficient, which reveals oscillations that are approximately sinusoidal with an amplitude of $C_l \approx 5$.

For the flat plate, one can observe similar deflected vortex dipoles to those of the NACA 0012 airfoil during the peak deflection angles of the periodic oscillations. This is shown in Figure 25 for mode A, where the TEV dipoles appear very similar, even though this is a stable flow for the NACA 0012 airfoil and unstable for the flat plate. We note that the location and strength of the LEV appear different. Therefore we suggest that this jet switching is caused by the LEV.

3. Lift enhancement of oscillating rigid finite wings
3.1. Coupling with wake instabilities

Calderon *et al.* [36-38] demonstrated that resonance with the wake instabilities also exists for low-aspect-ratio wings. Figure 26 presents a comparison of the time-averaged lift coefficients of the two-dimensional airfoil and the (semi-aspect ratio) $sAR = 2$ rectangular wing with NACA0012 cross-section. Both wings are subject to an oscillating amplitude of $a/c = 0.15$ and a geometric angle of attack of $\alpha = 20°$. Overall the optimal frequencies are quite similar between the two wings with peaks observed at $Sr_c \approx 0.5$, $Sr_c \approx 0.9$ and $Sr_c \approx 1.5$ for the low aspect ratio case. The peaks that we observe for the low aspect ratio wing, illustrate that the phenomenon is not confined to quasi-two-dimensional flows. Force measurements were also carried out at a different Reynolds number of $Re = 20,000$, illustrating similar lift performance. Considering, similar Strouhal numbers require different forcing frequencies, due to the change in freestream velocity, the existence of similarly located peaks reinforce that this as a fluid dynamic phenomenon. As previously mentioned, the lock-in phenomenon with the sub-harmonic and harmonic of the natural vortex shedding frequency, in the case of a two-dimensional NACA0012 airfoil, provides an explanation for the existence of peaks in lift. Similar measurements of the wake vortex shedding frequency have been performed and summarized in Figure 27. It is seen that, for the angle of attack of $\alpha = 20°$ (corresponding to Figure 26), we observe a vortex shedding frequency of $St_c \approx 0.54$, which is significantly closer to the first peak in lift. Even at very low Reynolds numbers ($Re = 300\text{-}500$), vortex shedding from low-aspect-ratio wings has been reported [39]. In fact, it was shown that periodic excitation at a frequency slightly less than the natural frequency of vortex shedding can lead to enhanced lift [40].

Measurements of wake vortex shedding frequency for other angles of attack are also shown in Figure 27. A comparison has also been made with the vortex shedding frequencies reported by Rojratsirikul *et al.* [41], indicated by the shaded region, which includes various aspect ratios ($AR = 1$ - 10, and also 2D airfoils) and Reynolds numbers in the range of 10,000 to 120,000. This is superimposed by a dashed line of constant Strouhal number $Sr_d \approx 0.17$, as proposed by Rojratsirikul *et al.* [41], for which the projected height is used, instead of the chord length, as the characteristic length. The wake measurements for the $sAR = 2$ wing reveal a good fit with the literature. Superimposed within the same graph are the locations of the first and second peaks in the time-averaged lift for various angles of attack. It is seen that the first peak for $\alpha = 20°$, is very close to the natural vortex shedding frequency in the wake. However, for $\alpha = 10°$, the data seem to suggest that the first peak could be the sub-harmonic of the natural vortex shedding frequency. The interpretation is even more difficult for $\alpha =$

15°, for which the first peak of the lift is between the fundamental and the subharmonic of vortex shedding. It is apparent that the peaks in lift are on the same order as the frequencies of the wake instabilities of the stationary wing. However, the first peak remains remarkably unchanged for all three incidences, while the fundamental frequency of the wake instability and the second peak varies. The same is observed in the case of a flat plate wing with the same aspect ratio. This brings the question whether or not any other phenomenon might be contributing to the selection of the optimal frequency. This is discussed below for both the NACA 0012 and flat plate cross-sections.

Velocity magnitude and streamlines in the mid-span plane are shown in Figure 28 for the sAR = 2 wing with the NACA 0012 cross-section. Two phases in the cycle, corresponding to the halfway point and bottom of the downstroke, are shown at different operating Strouhal numbers. The two phases here give a good indication of the progression of the LEVs and TEVs at the early stages of their formation. Here $Sr_c = 0.45$ corresponds to the frequency at which the first peak in lift is observed (see Figure 26). With increasing frequency the leading edge vortex becomes more compact. In relation to the peaks that we observe in the time-averaged lift measurements, $Sr_c \approx 0.6$ corresponds to a local trough and $Sr_c \approx 0.9$ corresponds to the second peak. There is an apparent interaction between leading edge vortex and trailing edge-vortex for $Sr_c = 0.6$. In essence, the Strouhal number determines when the LEV reaches the trailing edge of the wing, yielding frequencies that synchronize the passing of the LEV with the formation of the TEV. Such appears to be the case at $Sr_c = 0.6$ and in the process, the LEV forms a dipole with the TEV. Due to the positioning and orientation of these two vortices, their induced velocity is directed upstream. At $Sr_c = 0.9$ the wing appears to recover somewhat, due to the delay of the leading edge vortex in reaching the trailing edge of the wing, significantly reducing the width of the wake. Consequently, the interaction between the leading edge and trailing edge vortices appears to contribute to the selection of optimal frequencies for lift.

Figure 29 shows iso-surfaces of constant velocity magnitude and vorticity magnitude in volumetric measurements over the $sAR = 2$ flat plate wing. The three frequencies here are very close to peaks and troughs observed in the time-averaged lift measurements. Similarities can be observed with respect to the size and location of the leading and trailing edge vortices, at the midspan of the wing, when comparing the 2D and 3D measurements. At $Sr_c = 0.4$, vortex dipoles are absent along the span, however, at $Sr_c=0.6$ a vortex dipole is observed at a

further location inboard of the midspan, and evidently absent closer to the tip beyond the leading edge vortex. For $Sr_c = 0.8$, there seems to be very little difference in streamline pattern inboard of the midspan location. Iso-surfaces of velocity magnitude illustrate that in the case of Sr_c=0.6, a stronger interaction between the LEV and TEV is nonetheless observed close to the midspan of the wing.

3.2. Main features of the vortical flows

A comparison of the computed and experimental results [42,43] for the $sAR = 1$ rectangular wing plunging at $Sr_c = 0.65$ is shown in Figure 30. The flow is reflected about the wing centerline ($z = 0$) with the assumption of lateral symmetry. (Note that the calibration process near the end plate resulted in a small region with no data). The three-dimensional phased-averaged flow structure is represented using the iso-surface of the Q-criterion ($Qc/U_\infty = 20$). Overall good agreement is observed between experiments and computations in terms of the main flow features. As the wing plunges downward (Figure 30b-e), a leading-edge vortex is formed due to the increasing effective angle of attack. This vortex is fairly coherent in the spanwise direction and is pinned at the front corners of the plate. The formation and strengthening of the tip vortices is also observed during the downstroke motion. The tip vortices join with the trailing-edge vortex (containing vorticity generated on the bottom plate surface) to form a vortex loop extending from one wing front corner to the opposing edge. These features are consistent with the vortical structures observed over finite wings previously [39,44-50].

In Figure 30, spanwise undulations of the leading-edge vortex are observed near the end of the downstroke (Figure 30f,g). The leading-edge vortex evolves into an "arch-type" structure similar to that found by Visbal [51]. The legs of the arch-vortex move downstream and towards the wing centerline. During the upstroke, the tip vortices appear to breakdown and the trailing-edge vortex is shed into the wake. For this relatively moderate-amplitude high-frequency heaving motion, the arch-vortex remains over the wing well into the next plunging cycle. For instance, in Figure 30d, the arch vortex is still located near the mid-chord and does not reach the trailing edge until the initiation of the subsequent upstroke (Figure 30h).

Figure 31 compares the evolution of the leading-edge vortex at $Sr_c = 0.8$ for various wing planforms. The effect on the elliptical wing with $b/c = 2$ is interesting, the leading edge vortex undergoes a remarkable transformation, developing a distinct undulation (see phase c).

This strong undulation encountered on the elliptical wing also occurs for the rectangular wing at some other Strouhal numbers [42,43]. These examples demonstrate that the three-dimensional vortical structures are quite complex. Calderon et al investigated how the spanwise undulations develop during the plunging motion by presenting the vortex core locations, using the Q-criterion as a core identification tool. Figure 32 reveals the progression of the undulation for both the elliptical and rectangular wing at $Sr_c = 0.75$. Twelve phases in the cycle were used to observe the progression of the undulation with time. Apparently, the undulation exists quite early on in the cycle. Initially close to the tip of the wing, but as the cycle progresses, the undulation both amplifies and travels inboard. It is interesting to note that the undulation appears far more prominent for the rectangular wing. Its overall shape is also highly sensitive to Strouhal number.

Figure 33 shows the vortical structures at higher Strouhal numbers of $Sr_c = 1.0$-1.35 for flat-plate wings. The higher Strouhal numbers appear to dampen any strong undulations across the span of the wings. We observe instead that the LEV anchor point remains quite close to the tip, and moves further away from the surface further inboard of the wing. The considerable vertical movement is consistent with a reduction in lift performance at the higher Strouhal numbers. A sudden dissipation of the leading edge vortex is observed near the root with increasing Strouhal number. (This is similar to the flat-plate airfoil case shown in Figure 23 and discussed in more detail). It is apparent that the breakdown of the leading edge vortex is dependent on the spanwise position. Whilst, the leading edge vortex is pinned to the surface of the wing, it remains largely coherent closer to the tip, but loses coherency inboard.

Finally, we point out the formation of unusual vortex rings for flows with high Strouhal number. Both upper surface and lower surface tip vortices are generated at high Strouhal numbers due to the higher effective angles of attack. Figure 34 show that these tip vortices form a vortex ring. Although the iso-surfaces represent a constant Q-criterion value, colour maps have been superimposed to illustrate any variation in the streamwise component of vorticity, ω_x. In this way tip vortices formed during the downstroke and upstroke can be differentiated. In Figure 34, it is evident that the vortex ring consists of an interaction between lower and upper surface tip vortices. The comparison at various Strouhal numbers suggests that the phenomenon is associated with high Strouhal numbers. This vortex ring induces velocity in the spanwise (and outboard) direction. It should be noted that in the

previous work on pitching wings at high Strouhal number, wake vortices have been observed to undergo spanwise compression [47,48], for which tip vortices have an induced velocity directed towards the symmetry plane of the wing. The tip vortices described here seem to differ significantly from these studies.

Another consequence of the tip vortices is that bifurcated/asymmetric wakes discussed in the two-dimensional case (Section 2.3) have not been observed for finite wings for the same conditions (Strouhal number and amplitude) [52]. In fact, there is no evidence that such asymmetric wakes exist for finite wings. This may be due to the fact that tip vortices shed during the upward and downward motion, and form vortex loops. The position of the tip vortices with respect to the wing (either above or below the wing) appears to enforce a boundary condition that prevents vortex loops from moving below or above the wing.

3.3. Effect of leading-edge sweep

For a wing with zero sweep angle, and at a high angle of attack in the post-stall region, there is only partial or intermittent (periodic) reattachment, when the wing oscillates. Complete flow reattachment is not possible due to the lack of spanwise removal of vorticity for zero sweep angle. There is evidence that moderate sweep angles are beneficial in achieving complete and steady reattachment. Potential of lift enhancement due to the flow reattachment by means of small-amplitude wing oscillations has been explored in various studies for nonslender delta wings [53-55]. Nonslender delta wings (sweep angle $\Lambda \leq 55°$) have different flow topology at high angles of attack [56] compared to the slender delta wings ($\Lambda \geq 65°$). The primary attachment line occurs on the wing surface outboard of the symmetry plane, even when vortex breakdown is near the apex, for the nonslender delta wings. Hence there is potential to manipulate the reattachment of the flow by means of wing oscillations [6]. Figure 35 shows the dye flow visualization for a stationary and oscillating (small amplitude rolling motion) delta wing with a sweep angle of $\Lambda = 50°$ at an angle of attack of $\alpha = 25°$. It is seen that completely separated flow for the stationary wing becomes reattached on the wing surface with increasing Strouhal number.

This effect is better illustrated in a cross-flow plane using laser fluorescence flow visualization as shown in Figure 36. The difference between the stationary and oscillating wing appears small for pre-stall incidences, however, flow reattachment is remarkable in the

post-stall angles of attack. The dashed line in the pictures shows the symmetry plane of the wing. The time-averaged velocity field in a cross-flow plane is shown in Figure 37 for an angle of attack of $\alpha = 25°$. It is noted that this substantial effect has been achieved for small amplitude (1°) of rolling motion. Both pitch and roll oscillations are effective in the control and reattachment of the separated flow [55]. Experiments with various simple and cropped delta wings show that the reattachment process is similar for all nonslender wings. However, there appears to be a lower limit of sweep angle ($\Lambda = 20°$), below which the beneficial effect of leading-edge sweep diminishes.

It is also noted in Figure 35 that the leading-edge vortices re-form at high Strouhal numbers, with axial flow and subsequent breakdown. While there is only reattachment at low Strouhal numbers, such as $Sr_c = 0.3$, axial flow develops in the core of the vortices, and then breaks down further downstream at high Strouhal numbers. Wing oscillations therefore produce two separate effects: first is the reattachment at low Strouhal numbers. Second is the vortex re-formation at high Strouhal numbers. Observations of reattachment and vortex re-formation for various nonslender wings suggest that there is an optimal range of frequencies, $Sr_c = 1$ to 2. This range of Strouhal numbers compares well with the dominant frequencies in the spectra of velocity fluctuations of the shear layer instabilities over the wings in the post-stall region.

4. Lift enhancement of oscillating flexible wings

Cleaver *et al.* [57,58] investigated the aerodynamics and fluid-structure interactions of flexible rectangular wings with aspect ratios of $sAR = 1.5$ and 3, which are clamped at the root and subjected to a harmonic plunging motion. As flow control and lift enhancement were the main objectives, post-stall angles of attack and small amplitude excitation at root were considered. For simplicity, wings with flat-plate cross-section were considered. An example is shown in Figure 38 for three wings with different flexibility at an angle of attack of 15°. It is seen that, up to $Sr_c \approx 0.8$, the time-averaged lift coefficients are the same for all wings. However, with increasing Strouhal number, the lift curves start to diverge. For the "highly flexible" wing, there is substantial lift enhancement compared to the rigid wing, which seems to increase with increasing Strouhal number. It appears that there is no optimal Strouhal number. For this wing, the natural frequency of the first bending mode was measured as $Sr_c =$

1.5 in still fluid in the absence of free-stream flow. At the natural frequency, the lift coefficient of this wing is more than the double of that of the rigid wing. Therefore, detailed measurements of the wing deformation and phase-averaged flow were made at this Strouhal number, $Sr_c = 1.5$, which is also in the realistic range for micro air vehicle applications as shown in Figure 1.

The deformation of this wing is mostly in the bending mode with negligible twist. As the spanwise flexibility is dominant, the deformation of the wing tip is important to characterize the fluid-structure interaction. Figure 39 shows the variation of the amplitude ratio and phase angle of the wing tip as a function of Strouhal number. The tip amplitude increases with increasing frequency, revealing a local maximum around $Sr_c \approx 1.3$. The phase angle (with respect to the root) increases with increasing frequency. At the natural frequency ($Sr_c = 1.5$), the tip amplitude is 1.84 times the value at the root, and the phase angle is around 90°. (This phase lag is similar to that found for maximum lift for a flexible plate tilted to horizontal and plunging at zero free-stream velocity [59]. These characteristics of the fluid-structure interaction are similar to those of a system with damping. The wing shape during the plunging cycle is represented in Figure 40. The mid-chord position is plotted as a function of the spanwise direction at different phases in the cycle. The solid lines are for the root moving downwards and dashed lines are for the root moving upwards. When moving down the wing tends to be deformed upwards, and when moving up the wing tends to be deformed downwards. This indicates that the tip motion lags behind the root motion.

Figure 41 and 42 show the volumetric velocity measurements for the rigid and "highly flexible" wing at this Strouhal number. Iso-surfaces of the phase-averaged vorticity magnitude overlaid with spanwise vorticity reveal that the rigid wing experiences a LEV dipole formation (similar to the case of the flat-plate airfoil in Figure 23), whilst the flexible wing experiences a stronger convected LEV and tip vortex. While the LEV dipole for the rigid wing dissipates very quickly and does not contribute much to the lift, the much stronger LEV and tip vortex explain the significantly higher lift. Hence, the flexibility inhibits LEV dipole formation, resulting in a stronger convected LEV and stronger tip vortex, which also contributes to the lift for low aspect ratio wings.

The above mentioned studies are concerned with flow control using aeroelastic effects and are limited to small-amplitude high-frequency motions as discussed in the introduction. However, it is interesting to consider the effect of flexibility on lift in biologically inspired flows for which the kinematics is very different (much larger amplitudes and smaller frequencies). It appears that the effect of flexibility depends on the kinematics as well as the main direction of the flexibility (chordwise versus spanwise flexibility or a combination), and possibly on the density ratio. For an insect hovering motion, Zhao *et al.* [60,61] had essentially chordwise flexibility, and observed a reduction in the lift compared to the rigid wing. This can be easily understood by the negative camber produced by the chordwise flexibility. On the contrary, Nakata and Liu [62] observed an increase in the lift for a hovering hawkmoth, when a realistic structural model was used, which combined chordwise and spanwise flexibility. In this case, three-dimensional LEV was found to be enhanced on the flexible wing. For a very different kinematics similar to a bird flapping, Hu *et al.* [63] observed that the flexibility generally decreased the lift, even though a combination of the chordwise and spanwise flexibility was used, confirming the importance of the wing kinematics as well. A tilted flexible wing plunging at zero free stream at a low Reynolds number (based on the plunge velocity) of $Re = 100$ suggests enhanced lift and the maximum is found near the natural frequency of the wing [59]. This is in contrast with the lack of an optimal Strouhal number that maximizes the lift in the experiments of Cleaver *et al.* [57].

5. Lift enhancement of self-excited flexible wings

5.1. Nonslender delta wings

Previous sections considered active flow control approaches for which external energy is required to oscillate the rigid or flexible wings in order to achieve lift enhancement. In this section, we consider self-excited wing vibrations as a passive flow control approach. One of the examples in this category is flexible nonslender delta wings [64]. Figure 43 show that substantial lift enhancement is possible for thin flexible delta wings compared to the rigid ones. It is seen that this lift enhancement is observed for nonslender wings only. This passive flow control method achieves lift enhancement in the post-stall region and delays the stall. It was shown that time-averaged deformation does not contribute to the lift enhancement. Self-excited vibrations in the anti-symmetric mode are essential for creating lift enhancement. It is therefore only observed for the full wing, and not for a half-model. Figure 44 shows the dominant frequency of the wing vibrations in the anti-symmetric mode as a function of sweep

angle. The inset shows a typical mode shape, which is the second anti-symmetric mode. The Strouhal number of the dominant frequency of structural vibration was on the order of unity, which also corresponds to the frequency of the shear layer instabilities.

Vibration of the wing increases the energy of the vortices shed into the shear layer, which allows the transfer of momentum from the freestream, resulting in reattachment. This is shown in Figure 45 with the help of the near-surface time-averaged streamlines for the rigid and flexible wings. It is seen that flow reattachment downstream of the apex occurs for the flexible wing. There is no axial flow forming within the reattached region, which is similar to a three-dimensional conical separation bubble in the time-averaged sense.

5.2. Membrane wings

Membrane wings are preferred due to their inherent lightweight and ability to change shape for MAV applications [2]. This article is not intended to be an extensive review of the literature associated with membrane wings. In terms of the fluid-structure interactions and the main theme of this paper, we do not focus on the well-known ability of changing shape and camber of membrane wings [65]. Instead, we focus on the unsteady aspects of the fluid-structure interaction and the effect on aerodynamic forces. Flow-induced vibrations of membrane airfoils [66,67] and low-aspect ratio wings [41,68] were investigated in recent studies. Amplitude and mode of the vibrations of the membrane depends on the relative location and the intensity of the unsteadiness created by the separated shear layer, indicating a strong coupling of the unsteady flow with the membrane oscillations. This is demonstrated in Figure 46, where the time-history of the locations of the shear layer and membrane are shown. Coupling of the membrane oscillations and separated shear layer is demonstrated with a high degree of correlation between the membrane displacement and location of the shear layer. However, this coupling may also increase the lift force fluctuations [69].

There is also evidence of coupling of the membrane oscillations with the vortex shedding for post-stall incidences. It is suggested that membrane vibrations occur at the natural frequencies close to the harmonics of the wake instabilities [41]. Figure 47 shows flow visualization and Reynolds stress measurements for post-stall incidences for a rigid (but cambered) airfoil and flexible membrane airfoil. The roll-up of large vortices and smaller wake for the flexible membrane suggest that flexibility might decrease drag. Delay of the stall and lift enhancement for membrane wings are well known. Some of these benefits

originate from the unsteady fluid-structure interactions. Hence this is a potential flexibility-based passive flow control method.

There is evidence that similar benefits exist for low-aspect ratio wings. Figure 48 shows a MAV with a membrane wing [70], which exhibits lift enhancement relative to a rigid one. This lift enhancement is observed in the post-stall region, increasing the maximum lift and delaying the stall. Separated flows over low aspect ratio wings are common and contribute to the lift substantially. Wing flexibility and self-excited membrane vibrations may therefore have a significant effect by influencing the separated flow and tip vortices, similar to leading-edge vortices over nonslender delta wings.

6. Thrust enhancement of flexible wings

6.1. Chordwise flexibility

Numerical models have indicated higher propulsive efficiencies for flexible airfoils [71,72], although the computational complexity of the situation often requires the assumption of either inviscid flow [73,74] or of a pre-defined flexing motion [75,76]. Recent studies have presented coupled viscous fluid-structure computations [77-80]. Experimentally, there are findings of higher thrust at zero freestream velocity [81,82], and of higher efficiency at non-zero Reynolds numbers [83,84]. Thiria and Godoy-Diana [85] tested a self-propelled flapping wing with chordwise flexibility, mounted on a rotating arm. They reported enhanced thrust with flexibility. These studies of chordwise flexibility have been inspired by the structure of insect wings. It is well known that insect wings are not rigid, but have intricate variations in their stiffness [15]. Flexibility appears to be more important in the chordwise direction. Typically, chordwise flexural stiffness is 1-2 orders of magnitude smaller than spanwise flexural stiffness [86]. Also, insect wings have relatively stiff leading-edges, which was modelled with the shape shown in Figure 49 in the experiments of Heathcote and Gursul [81,84]. This shape is made of a rigid small airfoil at the leading-edge and a long flexible flat plate. The rigid leading-edge was subjected to pure periodic heaving motion. The stiffness of the flexible section could be varied by using plates of different thickness.

The most important dimensionless number in characterizing the effect of flexibility is the bending stiffness coefficient:

$$\lambda_x = \frac{(EI)_x}{\frac{1}{2}\rho U_\infty^2 S c^2}$$

(7)

where $(EI)_x$ is the flexural stiffness in the chordwise direction and S is the wing surface area. This dimsnionless number is similar to the "effective stiffness" used by Kang *et al.* [80]. A different definition, $E/\rho_b g c$, has also been used by Zhu [87], where ρ_b is the foil density. However this parameter does not relate the aeroelastic forces to the fluid forces. Hence, comparison of thrust and efficiency as a function of this parameter is not as meaningful in describing the fluid-structure interaction. The values of $(EI)_x$ are given as a function of the chord length for various insects by Combes and Daniel [86]. As a typical value, we estimate the bending stiffness coefficient λ_x for *Bombus* and *Manduca,* by using the values of $(EI)_x$ and typical wing surface and forward flight speed [88] as $\lambda_x \approx 2$ and $\lambda_x \approx 0.9$, respectively. In the experiments of Heathcote and Gursul [84], this parameter was varied between 0.07 and 260.

The primary result of the chordwise flexibility is the generation of a pitch angle denoted as θ in Figure 49. Hence, due to the chordwise flexibility, a single-degree-of-freedom heaving motion generates a two-degrees-of-freedom motion of the combined heaving and pitching. An example of displacement-time plot for $Re = 9,000$, $t/c = 0.56 \times 10^{-3}$ (plate thickness-to-chord ratio), and $Sr_A = 0.34$ is shown in Figure 49. The displacement of the leading and trailing edges, and of the difference between them, $s_{LE}-s_{TE}$, are plotted as functions of time. It is seen that the trailing-edge trails the leading-edge in phase, whereas $s_{LE}-s_{TE}$ is seen to lead the leading-edge. The difference $s_{LE}-s_{TE}$ is related to the pitch angle. Pitch amplitude, pitch phase angle and trailing-edge amplitude are all important parameters that affect the shedding of leading-edge and trailing-edge vortices.

Figure 50 shows the variation of the circulation of the trailing-edge vortices and vortex lateral spacing of the reverse Karman vortex street that forms in the thrust producing wakes. These quantities are shown as a function of plunge amplitude for three airfoils with varying flexibilities. It is seen that the strength of the vortices is the smallest for the very flexible plate. The normalized circulation of the flexible plate is equal to or larger than the circulation of the rigid airfoil. Except for the smallest value of plunge amplitude tested, the lateral spacing differs with flexibility. It is seen that the width of the reverse Karman street is largest

for the flexible plate. The combination of stronger vortices and wider jet implies enhanced thrust for the flexible case [81,84].

Figure 51 shows the vorticity field for a rigid, flexible, and very flexible airfoil for $Re =$ 18,000. The leading-edge of the airfoil is moving upwards through the origin at this instant and the instantaneous shape of the airfoils is also shown for each case. Clockwise vorticity is shown white, counter-clockwise vorticity black. The highest thrust coefficient occurs for the airfoil of intermediate stiffness (middle row). It is seen that the vortices from the intermediate airfoil are stronger, and spaced further apart in the lateral direction than those from the stiffest airfoil. Although a large distance in the lateral direction separates the vortices from the least stiff airfoil, their strength is considerably lower than for either of the other two airfoils. Hence, for an airfoil with chordwise flexibility, amplitude and phase of the trailing-edge play a major role in determining the strength and spacing of the vortices. Measured circulation of the shed vortices and lateral spacing between them (width of the induced jet) strongly depend on the airfoil flexibility. Direct force measurements confirm that there is an optimum airfoil stiffness for a given heaving frequency and amplitude [81]. Hence, this offers a possibility for vortex control with passive flexibility.

The complete data set is represented as contour plots in Figure 52 for thrust coefficient and propulsive efficiency. Contours of thrust coefficient are drawn on a Pitch Phase Angle – Strouhal Number plane. The white curve indicates the optimum pitch phase angle (in terms of thrust) for a given Strouhal number. The optimum pitch phase angle is observed to decrease as the Strouhal number increases. Thrust peaks at pitch phase angles similar to those for rigid airfoils in coupled heave and pitch [84]. The corresponding plot for propulsive efficiency exhibits a peak in efficiency at a Strouhal number of $Sr_A = 0.29$. It is noted that this lies within the range of Strouhal numbers of $0.2 < Sr_A < 0.4$ found in nature [89]. The optimum pitch phase angle is seen to be $100°\pm4°$, consistent with the values found in studies of rigid airfoils in coupled heave and pitch, and those found in nature. It is noted that the angles found to optimize the thrust coefficient, both in the literature and in the present study, are higher than those found to maximize the efficiency. This is consistent with the previous observations that it is not generally possible to achieve maximum thrust and efficiency simultaneously.

6.2. Drag reduction

Thrust generation by oscillating airfoils can be used for drag reduction. In particular, this can be achieved either actively by means of forced motion or passively through wave motion near a free surface. Bioinspired applications [90] as well as applications to low-speed vessels [91] are some of the possibilities. The passive scenario is the more interesting possibility because it requires no work input, and any hydrofoil passing through waves will experience the effect [92]. In essence, as the craft passes through waves, it will be subject to an oscillatory freestream due to both the oscillatory flow within the waves and also the motion of the vessel reacting to the waves.

The passive scenario was modeled as a plunging foil near free surface computationally [93] and experimentally [94]. The drag reduction of a NACA 0012 foil plunging near a free surface was investigated as a function of depth from the surface and oscillation amplitude [94]. Phase-averaged vorticity during the plunging cycle is shown and compared for two depths in Figure 53. Free-surface waves, vorticity generation within the wave, and interaction with the foil vortices (this is visible in the phases (a) and (d)) are some of the main characteristics. It was also shown that there is significant wave formation at critical Strouhal numbers resulting in higher drag, and a substantial effect on leading-edge vortex formation. For depths greater than two chords, the free-surface has a negligible effect.

The possibility of enhancing the drag reduction by means of small flexible plates attached to the trailing-edge was investigated by Cleaver *et al.* [95]. This configuration is shown in the inset of Figure 54. It was shown that the drag reduction depends on the length of the flexible plate, oscillation amplitude and the aeroelastic parameter. Simultaneous measurements of the deformation and the drag reduction revealed a relationship between the drag reduction, the aeroelastic parameter λ, and the amplitude of the flap angle δ, as shown in Figure 54. Here λ is defined as:

$$\lambda = \frac{\dfrac{1}{12}Et^3}{\dfrac{1}{2}\rho U_\infty^2 L_{TED}^3}$$

(8)

where L_{TED} and t are the length and thickness of the flexible plate attached to the main wing.

Parts (a) and (b) show the results for two different lengths $L_{TED} = 0.2c$ and $L_{TED} = 0.3c$, and the data of Heathcote *et al.* [84] ($L_{TED} = 0.66c$) is also shown in part (c) for comparison. As expected, excessively flexible plates (small λ) result in decreasing drag reduction. It is interesting that maximum drag reduction highlights an optimal flap angle amplitude of around 10°-15°, and optimal flexibility on the order of unity, $\lambda_{opt} = O(1)$. The magnitude of the drag reduction increases with increasing plate length.

6.3. Spanwise flexibility

Liu and Bose [96] studied the effect of spanwise flexibility on the flukes of an immature fin whale, using inviscid calculations. The phase of the flexing motion relative to the heave was found to be a key parameter in determining the thrust and efficiency characteristics of the fin. For insect wings the spanwise flexural stiffness is much larger than that the chordwise flexural stiffness, hence spanwise flexibility might not appear to be as important. However, the length scale (wing span) is also larger than the chord length; hence the deformation in the spanwise direction is expected to be significant. Effect of spanwise flexibility on the aerodynamics of heaving wings was recently investigated experimentally [97]. A schematic of the experimental setup is shown in Figure 55. Computational studies of these experiments were carried out by Chimakurthi *et al.* [78], Gordnier *et al.* [98], Shyy *et al.* [79] and Kang *et al.* [80]. A rectangular wing was subjected to pure periodic heaving motion near the root. Three wings (Inflexible, Flexible and Highly Flexible) with various spanwise flexural stiffness were tested.

The proper dimensionless number to characterize the effect of spanwise flexibility is the bending stiffness coefficient:

$$\lambda_y = \frac{(EI)_y}{\frac{1}{2}\rho U_\infty^2 S b^2} \tag{9}$$

where $(EI)_y$ is the flexural stiffness in the spanwise direction and b is the wing span. The values of $(EI)_y$ are given as a function of the wing span for various insects by Combes and Daniel [86]. As a typical value, we estimate the bending stiffness coefficient λ_y for *Bombus* and *Manduca,* by using the values of $(EI)_y$ and typical wing surface and forward flight speed (Shyy et al., 2008) as $\lambda_y \approx 3.0$ and $\lambda_y \approx 3.6$, respectively. It is interesting that the bending stiffness coefficients in the spanwise and chordwise directions are not very different in

magnitude even though the flexural stiffness is 1-2 orders of magnitude different. In the experiments of Heathcote *et al.* [97], this parameter varied between 4.8 and 130 as a function of flexural stiffness and free stream velocity.

The tip displacements of the three wings are plotted over a period of two cycles in Figure 55 for $Re = 30,000$ and $k_G = \pi f c / U_\infty = 1.82$. The wing tip curves lie to the right of the root displacement curve, indicating a phase lag. The plot illustrates the steep increase in tip amplitude moving from the Inflexible to the Flexible wing, with only a small increase in tip phase lag. Hence, a degree of spanwise flexibility increases the effective amplitude of the heaving motion in each spanwise section. This was found to be beneficial as long as the phase delay is not large. Figure 56 shows the variation of the thrust coefficient as a function of dimensionless frequency, which indicates substantial enhancement for the flexible wing at high frequencies. In this case, a moderately stronger trailing-edge vortex system was observed due to the increase in the effective heave amplitude [97]. These results offer the possibility of flow control with structural tuning for micro air vehicles.

Introducing a far greater degree of spanwise flexibility, however, was found to be detrimental. As it is also seen from Figure 55, there is a large tip phase lag for the Highly Flexible wing. This large phase delay between the tip and root causes them to move in opposite directions for a significant portion of the cycle. This resulted in vorticity of opposite sign being shed simultaneously from the root and tip. Figure 57 shows the vorticity patterns when the root is moving downwards through the origin. Figure 57(a) illustrates that while the tips of the Inflexible and Flexible wings move in the same direction as the root at this point in time, the tip of the Highly Flexible wing moves in the opposite direction. The effect on the flow field is shown in Figure 57(b). Vorticity fields at six planes along the span are shown for each of the three wings. To minimize the degree of overlap of the vorticity fields, the *z* axis is scaled differently to the *x* and *y* axes. For the Highly Flexible wing (shown at the bottom) it is seen that the sense of vorticity shed at the root is opposite to that shed near the tip.

Kang *et al.* [80] generalized the effects of spanwise and chordwise flexibility. It was suggested that a relationship between the thrust and maximum relative wing-tip deformation exists. It is also suggested that the maximum thrust is observed when flapping near the

resonance and the maximum efficiency is reached when flapping at about half of the natural frequency (this ratio is in the range of 0.33 to 0.6 in various studies according to [80]). On the other hand, Thiria and Godoy-Diana [85] suggest that a simple resonance cannot explain the observed behavior.

7. Conclusions

This review article details recent progress in the field of fluid-structure interactions as a means of low Reynolds number flow control. It describes a wide range of possible flow control methodologies, several of which show promise.

For rigid airfoils plunging with small-amplitude, two mechanisms of lift enhancement have been identified: deflected jets and convected LEVs. Stable deflected jets form at high Strouhal numbers for pre-stall angles of attack. Deflected jets are caused by pairing of the clockwise and counter-clockwise TEVs to form dipoles. These dipoles are asymmetric in position and strength, and therefore self-advect at an angle to the freestream creating asymmetry in the flow field. This asymmetry can create very large lift coefficients, up to $C_l \approx 6$, even for zero degrees angle of attack. Deflected jets do not form at low Strouhal numbers due to insufficient vortex strength, nor at larger incidences due to overwhelming bias for a particular direction. Convected LEVs have been shown to be an effective means of lift enhancement for post-stall angles of attack. At low Strouhal numbers upper-surface LEVs form during the downward motion of the airfoil and then convect over the upper surface creating a low pressure region. As these LEVs are created by the plunging motion, the increase in lift coefficient is approximately proportional to the plunge velocity. This form of flow control is particularly effective when the plunge frequency equals the natural shedding frequency, its harmonics or subharmonics, and continues until high Strouhal numbers when a new mode of LEV behaviour is observed. In this new mode the LEV still forms during the downward motion, but remains over the leading-edge and is therefore destroyed through impingement with the upward moving airfoil. Even though this new mode is associated with low lift it does correlate very well with the switch from drag to thrust. Both of these mechanisms are strongly influenced by the choice of airfoil shape. For a flat plate airfoil, instead of stable deflected jets, the deflected jets periodically switch direction resulting in periodic changes in the direction of lift with a large period. Instead of convected LEVs, LEV dipoles form for Strouhal numbers greater than unity. These LEV dipoles propagate upstream and away from the airfoil surface resulting in very low lift.

For finite wings oscillating at post-stall incidence, similar lift-enhancing convected LEVs are observed, however the flow field is more complicated. The LEV anchors towards the tip on the wing's upper surface. The tip vortex acts to drive this anchor point inboard towards the root creating an undulation in the LEV. This effect is most pronounced for the elliptical planform. The degree of lift-enhancement is diminished by decreasing aspect ratio. For certain cases interaction between the upper-surface and lower-surface tip vortex can result in tip vortex rings which expand in the spanwise direction. In addition, the tip vortex also prevents the formation of high-lift deflected jets previously observed for airfoils at pre-stall incidences. For nonslender delta wings small-amplitude roll and pitch oscillations can improve performance significantly. At low Strouhal numbers flow reattachment is observed; at higher Strouhal numbers vortex reformation is observed. The optimum is observed in the Strouhal number range: $Sr_c \approx 1 - 2$, which compares well with the dominant frequencies of the shear layer instability.

For oscillating flexible wings appropriate spanwise flexibility can significantly enhance lift performance. For a Strouhal number of $Sr_c = 1.5$, a semi-aspect ratio three flexible wing has a lift coefficient more than twice its rigid counterpart. This improvement is associated with significant spanwise deformation of the wing such that the tip lags the root by 90^0 but with an amplitude 1.84 times larger. In terms of the flow field, the rigid wing exhibits weka vortical structures near the leading-edge, which are essentially the three-dimensional version of the LEV dipole observed for flat plate airfoils. Conversely the flexible wing exhibits a strong convected LEV and high lift.

In these previous cases the root was actively plunged in forced oscillations and therefore requires power input. It is also possible to use fluid-structure interactions to passively enhance lift. For nonslender delta wings, self-excited anti-symmetric wing vibrations can significantly enhance lift in the post-stall region. The vibrations increase the energy of the vortices shed into the shear layer, which allows the transfer of momentum from the freestream, resulting in reattachment. Similarly membrane wings exhibit self-excited oscillations which can enhance lift in the post-stall region. Coupling between vortex shedding and the shear layer with membrane oscillations have been clearly demonstrated. It is believed that these may affect the separated flow and tip vortices in a similar manner to leading-edge vortices over nonslender delta wings.

Fluid-structure interaction can also be exploited for drag reduction / thrust enhancement. For plunging airfoils, appropriate chordwise flexibility can increase both thrust and efficiency. The most effective flexibilities are for elastic parameters on the order of unity. It is suggested that appropriate flexibility increases the spacing and circulation of the vortices in the reverse-Karman vortex street, whereas excessive flexibility induces separation which diminishes TEV circulation. The maximum increase in the time-averaged thrust through flexibility can be well in excess of 100%. Similarly spanwise flexibility can improve thrust performance although the effect is not as pronounced. The spanwise deformation amplifies the root motion but with a slight phase lag. Due to this larger amplitude the trailing-edge vortices, and therefore the reverse-Karman vortex street, are moderately stronger, leading to increased thrust. A typical improvement is approximately 50% more than the rigid case.

REFERENCES

[1] Mueller, T.J. and DeLaurier, J.D., "Aerodynamics of small vehicles", *Annual Review of Fluid Mechanics"*, vol. 35, 2003, pp. 89-111.

[2] Shyy, W., Berg, M. and Ljungqvist, D., "Flapping and flexible wings for biological and micro air vehicles", *Progress in Aerospace Sciences,* vol. 35, 1999, pp. 455.

[3] Ho, S., Nassef, H., Pornsinsirirak, N., Tai, Y.C., and Ho, C.M., "Unsteady aerodynamics and flow control for flapping wing flyers", *Progress in Aerospace Sciences*, vol. 39, 2003, pp. 635-681.

[4] Gursul, I., "Vortex flows on UAVs: issues and challenges", *The Aeronautical Journal,* vol. 108, 2004, pp. 597-610.

[5] Seifert, A., Greenblatt, D. and Wygnanski, I.J., "Active Separation Control; an Overview of Reynolds and Mach Number Effects," *Aerospace Science and Technology,* Vol. 8, 2004, pp. 569-582.

[6] Gursul, I., Wang, Z., and Vardaki, E., "Review of Flow Control Mechanisms of Leading-Edge Vortices", *Progress in Aerospace Sciences*, vol. 43, 2007, pp. 246-270.

[7] Raju, R., Mittal, R., Cattafesta, L.N., "Dynamics of Airfoil Separation Control Using Zero-Net Mass-Flux Forcing," *AIAA Journal,* Vol. 46, No. 12, December 2008, pp. 3103-3115.

[8] Wu, J.Z., Lu, X.Y., Denny, A.G., Fan, M. and Wu, J.M., "Post-stall flow control on an airfoil by local unsteady forcing," *Journal of Fluid Mechanics*, Vol. 371, 1998, pp. 21-58.

[9] Miranda, S., Vlachos, P.P., Telionis, D.P. and Zeiger, M.D., "Flow control of a sharp-edged airfoil," *AIAA Journal*, Vol. 43, No. 4, 2005, pp. 716-726.

[10] Glezer, A., Amitay, M., and Honohan, A.M., "Aspects of Low- and High-Frequency Actuation for Aerodynamic Flow Control," *AIAA Journal,* Vol. 43, No. 7, July 2005, pp. 1501-1511.

[11] Maxworthy, T. "The fluid dynamics of insect flight", *Annual review of Fluid Mechanics,* vol. 13, 1981, pp. 329-350.

[12] Triantafyllou, M.S., Triantafyllou, G.S. and Yue, D.K.P., "Hydrodynamics of fishlike swimming", *Annual Review of Fluid Mechanics,* vol. 32, 2000, pp. 33-53.

[13] Azuma, A., *The Biokinetics of Flying and Swimming*, 2nd edition, AIAA.

[14] Platzer, M.F., Jones, K.D., Young, J. and Lai, J.C.S, "Flapping-wing aerodynamics: progress and challenges", *AIAA Journal,* vol. 46, no. 9, pp. 2136-2149.

[15] Wootton, R.J., "Support and deformability in insect wings" *Journal of Zoology: Proceedings of the Zoological Society of London,* vol. 193, 1981, pp. 447-468.

[16] Steppan, S.J., "Flexural stiffness patterns of butterly wings (Papilionoidea)", *Journal of Research on the Lepidoptera,* vol. 35, 2000, pp. 61-77.

[17] Sunada, S., Zeng, L. and Kawachi, K., "The relationship between dragonfly wing structure and torsional deformation", *Journal of Theoretical Biology*, vol. 193, pp. 39-45.

[18] Vanella, M., Fitzgerald, T., Preidikman, S., Balaras, E. and Balachandran, B., "Influence of flexibility on the aerodynamic performance of a hovering wing", *Journal of Experimental Biology*, vol. 212, 2009, pp. 95-105.

[19] Visbal, M.R., "High-Fidelity Simulation of Transitional Flows past a Plunging Airfoil", *AIAA Journal*, Vol. 47, No. 11, 2009, pp. 2685-2697.

[20] Cleaver, D.J., Wang, Z., Gursul, I. and Visbal, M.R., "Lift Enhancement by means of Small Amplitude Airfoil Oscillations at Low Reynolds Numbers", *AIAA Journal*, vol. 49, No. 9, September 2011, pp. 2018-2033.

[21] Cleaver, D., Wang, Z. and Gursul, I., "Investigation of Mechanisms of High Lift for a Flat-Plate Airfoil undergoing Small-Amplitude Plunging Oscillations", *AIAA Journal*, vol. 51, pp. 968-980, 2013.

[22] Jones, K.D., Dohring, C.M. and Platzer, M.F., 1998, "Experimental and computational investigation of the Knoller-betz effect", *AIAA Journal*, vol. 36, no. 7, pp. 1240-1246.

[23] Lewin, G.C. and Haj-Hariri, H., 2003, "Modelling thrust generation of a two-dimensional heaving airfoil in a viscous flow", *Journal of Fluid Mechanics*, vol. 492, pp. 339-362.

[24] Heathcote, S. and Gursul, I., 2007, "Jet switching phenomenon for a periodically plunging airfoil", *Physics of Fluids*, vol. 19, pp. 2-

[25] Von Ellenrieder, K.D. and Pothos, S., 2008, "PIV measurements of the asymmetric wake of a two dimensional heaving hydrofoil", *Experiments in Fluids*, vol. 44, no. 5, pp. 733-745.

[26] Liang, C.L., Ou, K., Premasuthan, S., Jameson, A. and Wang, Z.J., 2011, "High-order accurate simulations of unsteady flow past plunging and pitching airfoils", *Computers and Fluids*, vol. 40, no. 1, pp. 236-248.

[27] Emblemsvag, J.E., Suzuki, R. and Candler, G., 2002, "Numerical simulation of flapping micro air vehicles", AIAA Paper 2002-3197.

[28] Godoy-Diana, R., Aider, J.L. and Wesfreid, J.E., 2008, "Transitions in the wake of a flapping foil", *Phys. Rev. E*, vol. 77, pp. 1-

[29] Godoy-Diana, R., Marais, C., Aider, J.L. and Wesfreid, J.E., 2009, "A model for the symmetry breaking of the reverse Benard-von Karman vortex street produced by a flapping foil", *Journal Fluid Mechanics*, vol. 622, pp. 23-32.

[30] Cleaver, D., Wang, Z. and Gursul, I., "Bifurcating flows of plunging airfoils at high Strouhal numbers", *Journal of Fluid Mechanics*, vol. 708, 2012, pp. 349-376.

[31] Andro, J.Y. and Jacquin, L., "Frequency effects on the aerodynamic mechanisms of a heaving airfoil in a forward flight configuration", *Aerospace Science and Technology*, vol. 13, no. 1, 2009, pp. 71-80.

[32] Young, J. and Lai, J.C.S., "Oscillation frequency and amplitude effects on the wake of a plunging airfoil," *AIAA Journal*, Vol. 42, No. 10, 2004, pp. 2042-2052.

[33] Bearman, P.W., "Vortex Shedding from Oscillating Bluff-Bodies," *Annual Review of Fluid Mechanics*, Vol. 16, 1984, pp. 195-222.

[34] Milne-Thomson, L.M., 1968, *Theoretical Hydrodynamics*, The Macmillan Press Ltd.

[35] Mueller, T. J., and DeLaurier, J. D., "An Overview of Micro Air Vehicles Aerodynamics," *Fixed and Flapping Wing Aerodynamics for Micro Air Vehicle Applications*, edited by T. J. Mueller, Vol. 195, Progress in Astronautics and Aeronautics, AIAA, Virginia, 2001, pp. 1-9.

[36] Calderon, D.E., Wang, Z., and Gursul, I., "Lift Enhancement of a Rectangular Wing Undergoing a Small Amplitude Plunging Motion", AIAA-2010-386, 48th AIAA Aerospace Sciences Meeting Including the New Horizons Forum and Aerospace Exposition, Orlando, Florida, Jan. 4-7, 2010.

[37] Calderon, D.E., Wang, Z., and Gursul, I., "Effect of Wing Geometry on the Lift of a Plunging Finite Wing", AIAA-2010-4459, 40th Fluid Dynamics Conference and Exhibit, 28 June – 1 July 2010, Chicago, Illinois.

[38] Calderon, D.E., Wang, Z., and Gursul, I., "Lift Enhancing Vortex Flows Generated by Plunging Rectangular Wings with Small Amplitude", *AIAA Journal,* in print.

[39] Taira, K. and Colonius, T., "Three-Dimensional Flow around Low-Aspect-Ratio Flat-Plate Wings at Low Reynolds Numbers", *Journal of Fluid Mechanics,* Vol. 623, 2009, pp. 187-207.

[40] Taira, K., Rowley, C.W., Colonius, T. and Williams, D.R., "Lift Enhancement for Low-Aspect-Ratio Wings with Periodic Excitation", *AIAA Journal,* Vol. 48, 2010, pp. 1785-1790.

[41] Rojratsirikul, P., Genc, M.S., Wang, Z., and Gursul, I., "Flow-Induced Vibrations of Low Aspect Ratio Rectangular Membrane Wings", *Journal of Fluids and Structures*, Vol. 27, 2011, pp. 1296–1309.

[42] Calderon, D.E., Wang, Z., Gursul, I. and Visbal, M.R., "Volumetric Measurements and Simulations of the Vortex Structures Generated by Low Aspect Ratio Plunging Wings", AIAA-2012-0914, AIAA Conference, Nashville, Tennessee, January 2012.

[43] Calderon, D.E., Wang, Z., Gursul, I. and Visbal, M.R., "Volumetric Measurements and Simulations of the Vortex Structures Generated by Low Aspect Ratio Plunging Wings", *Physics of Fluids,* vol. 25, 067102 (2013); doi: 10.1063/1.4808440

[44] Freymuth, P. "Visualizing the Connectivity of Vortex Systems for Pitching Wings," *J. Fluids Eng.* Vol. 111, 1989, pp. 217-220.

[45] von Ellenrieder, K.D., Parker, K. and Soria, J. "Flow Structures Behind a Heaving and Pitching Finite-Span Wing", *Journal of Fluid Mechanics*, Vol. 490, 2003, pp. 129-138.

[46] Blondeaux, P., Fornarelli, F., Guglielmini, L., Triantafyllou, M.S. and Verzicco, R. "Numerical Experiments on Flapping Foils Mimicking Fish-Like Locomotion", *Physics of Fluids*, Vol. 17, No. 11, 2005.

[47] Dong, H., Mittal, R. and Najjar, F.M. "Wake Topology and Hydrodynamic Performance of Low-Aspect-Ratio Flapping Foils", *Journal of Fluid Mechanics*, Vol. 566, 2006, pp. 309-343.

[48] Buchholz, J.H.J. and Smits, A.J. "On the Evolution of the Wake Structure Produced by a Low-Aspect-Ratio Pitching Panel", *Journal of Fluid Mechanics*, Vol. 546, 2006, pp. 433-443.

[49] Yilmaz, T.O. and Rockwell, D. "Three-Dimensional Flow Structure on a Maneuvering Wing", *Experiments in Fluids*, Vol. 48, No. 3, 2010, pp. 539-544.

[50] Yilmaz, T.O. and Rockwell, D., "Flow Structure on Finite-Span Wings due to Pitch-Up Motion", *Journal of Fluid Mechanics,* Vol. 691, 2012, pp. 518-545.

[51] Visbal, M.R., "Three-Dimensional Flow Structure on a Heaving Low-Aspect-Ratio Wing", 49th AIAA Aerospace Sciences Meeting, AIAA Paper 2011-219, Orlando, FL, 2011.

[52] Calderon, D., Cleaver, D.J., Wang, Z. and Gursul, I., "Wake structure of plunging finite wings", AIAA paper 2013-XXXX.

[53] Yaniktepe, B. and Rockwell, D., "Flow Structure on a Delta Wing of Low Sweep Angle", *AIAA Journal,* vol. 42, no. 3, March 2004, pp. 513-523.

[54] Yavuz, M.M., Elkhoury, M., and Rockwell, D., "Near-Surface Topology and Flow Structure on a Delta Wings", *AIAA Journal,* vol. 42, no. 2, February 2004, pp. 332-340.

[55] Vardaki, E., Wang, Z., Gursul, I., "Flow Reattachment and Vortex Re-formation on Oscillating Low-Aspect-Ratio Wings", *AIAA Journal,* vol. 46, no. 6, 2008, pp. 1453-1462.

[56] Gursul, I., Gordnier, R. and Visbal, M., "Unsteady Aerodynamics of Nonslender Delta Wings", *Progress in Aerospace Sciences,* vol. 41, 2005, pp. 515-557.

[57] Cleaver, D.J., Wang, Z. and Gursul, I., "Oscillating Flexible Wings at Low Reynolds Numbers", AIAA-2013-0674, AIAA Conference, Grapevine, Texas, January 2013.

[58] Cleaver, D.J., Calderon, D., Wang, Z. and Gursul, I., "Low Aspect Ratio Oscillating Flexible Wings at Low Reynolds Numbers", AIAA-2013-XXXX, AIAA Conference, San Diego, California, June 2013.

[59] Masoud, H. and Alexeev, A., "Resonance of flexible flapping wings at low Reynolds number", *Physical Review E,* 81, 056304 (2010).

[60] Zhao, L., Huang, Q., Deng, X. and Sane, S.P., "Aerodynamic effects of flexibility in flapping wings", *Journal of the Royal Society Interface,* vol. 7, 2010, pp. 485-497.

[61] Zhao, L, Deng, X. and Sane, S.P., "Modulation of leading edge vorticity and aerodynamic forces in flexible flapping wings", *Bioinspiration & Biomimetics,* vol. 6, 2011, pp. 1-7.

[62] Nakata, T. and Liu, H., "A fluid-structure interaction model of insect flight with flexible wings", *Journal of Computational Physics,* vol. 231, 2012, pp. 1822-1847.

[63] Hu, H., Kumar, A.G., Abate, G. and Albertani, R., "An experimental study of flexible membrane wings in flapping flight", AIAA-2009-876, 47th AIAA Aerospace Sciences meeting, 5-8 January 2009, Orlando, Florida.

[64] Taylor, G., Wang, Z., Vardaki, E. and Gursul, I., "Lift enhancement over flexible nonslender delta wings", *AIAA Journal,* vol. 45, 2007, pp. 2979-2993.

[65] Newman, B.G., "Aerodynamic theory for membranes and sails", *Progress in Aerospace Sciences,* vol. 24, 1987, pp. 1-27.

[66] Rojratsirikul, P., Wang, Z. and Gursul, I., "Unsteady fluid-structure interactions of membrane airfoils at low Reynolds numbers", *Experiments in Fluids,* vol. 46, 2009, pp. 859-872.

[67] Gordnier, R.E., "High fidelity computational simulation of a membrane wing airfoil", *Journal of Fluids and Structures,* vol. 25, 2009, pp. 897-917.

[68] Song, A., Tian, X., Israeli, E., Galvao, R., Bishop, K., Swartz, K. and Breuer, K., "Aeromechanics of membrane wings with implications for animal flight", *AIAA Journal,* vol. 46, 2008, pp. 2096-2106.

[69] Waldman, R.M. and Breuer, K.S., "Shape, lift, and vibrations of highly compliant membrane wings", AIAA Paper 2013-XXX, June 2013, San Diego.

[70] Lian, Y., Shyy, W., Viieru, D., Zhang, B., "Membrane wing aerodynamics for micro air vehicles", *Progress in Aerospace Sciences,* vol. 39, 2003, 425-465.

[71] Katz J., Weihs D., "Hydrodynamic Propulsion by Large Amplitude Oscillation of an Airfoil with Chordwise Flexibility," *J. Fluid Mech.*, Vol. 88, No. 3, 1978, pp. 485-497.

[72] Murray M. M., Howle L. E., "Spring stiffness influence on an oscillating propulsor," *Journal of Fluids and Structures*, Vol. 17, No. 7, 2003, pp. 915–926.

[73] Toomey, J. and Eldredge, J.D., 2008, "Numerical and experimental study of the fluid dynamics of a flapping wing with low-order flexibility", *Physics of Fluids,* 20, 073603 (2008).

[74] Michelin, S. and Smith, S.G.L., "Resonance and propulsion performance of a heaving flexible wing", *Physics of Fluids,* 21, 071902 (2009).

[75] Miao J.-M., Ho M.-H., "Effect of Flexure on Aerodynamic Propulsive Efficiency of Flapping Flexible Airfoil," *Journal of Fluids and Structures*, Volume 22, Issue 3, April 2006, Pages 401-419.

[76] Durrani, N. and Qin, N., "Numerical Simulation of Flexible Flapping Airfoil Propulsion using Dynamic Mesh at Low Reynolds Numbers", AIAA-2008-654, 46th AIAA Aerospace Sciences Meeting and Exhibit, 7-10 January 2008, Reno, Nevada.

[77] Tang, J., Viieru, D., and Shyy, W., "A Study of Aerodynamics of Low Reynolds Number Flexible Airfoils", AIAA-2007-4212, 37th AIAA Fluid Dynamics Conference and Exhibit, 25-28 June 2007, Miami, FL.

[78] Chimakurthi, S.K., Tang, J., Palacios, R., Cesnik, C.E.S., and Shyy, W., "Computational Aerolasticity Framework for Analyzing Flapping Wing Micro Air Vehicles", *AIAA Journal*, 47, 1865-1878 (2009).

[79] Shyy, W., Aono, H., Chimakurthi, S,K., Trizila, P., Kang, C.K., Cesnik, C.E.S., Liu, H., (2010), "Recent progress in flapping wing aerodynamic and aeroelasticity", *Progress in Aerospace Sciences*, 46, pp. 284-327.

[80] Kang, C.K., Aono, H., Cesnik, C.E.S. and Shyy, W., "Effects of flexibility on the aerodynamic performance of flapping wings", *Journal of Fluid Mechanics,* vol. 689, 2011, pp. 32-74.

[81] Heathcote, S., Martin, D., and Gursul, I., "Flexible Flapping Airfoil Propulsion at Zero Freestream Velocity", *AIAA Journal*, vol. 42, no. 11, 2004, pp. 2196-2204.

[82] Jones K. D., Platzer M. F., "Experimental investigation of the aerodynamic characteristics of flapping-wing micro air vehicles," AIAA Paper 2003-0418, *41st Aerospace Sciences Meeting & Exhibit*, 2003.

[83] Prempraneerach P., Hover F. S., Triantafyllou M. S., "The effect of chordwise flexibility on the thrust and efficiency of a flapping foil," *Proceedings of the Thirteenth International Symposium on Unmanned Untethered Submersible Technology*, 2003.

[84] Heathcote, S. and Gursul, I., "Flexible Flapping Airfoil Propulsion at Low Reynolds Numbers", *AIAA Journal*, vol. 45, no. 5, 2007, pp. 1066-1079.

[85] Thiria, B. and Godoy-Diana, R., "How ing compliance drives the efficiency of self-propelled flapping flyers, *Physical Review E,* 82, 015303(R) (2010).

[86] Combes, S.A. and Daniel, T.L., "Flexural stiffness in insect wings I. Scaling and the influence of wing venation", *The Journal of Experimental Biology,* 206, 2003, pp. 2979-2987.

[87] Zhu, Q., "Numerical Simulation of a Flapping Foil with Chordwise or Spanwise Flexibility", *AIAA Journal,* vol. 45, no. 10., October 2007, pp. 2448-2457.

[88] Shyy, W., Lian, Y., Tang, J., Viieru, D., and Liu, H., "Aerodynamics of Low Reynolds Number Flyers", Cambridge University Press, 2008.

[89] Taylor G. K., Nudds R. L., Thomas A. L. R., "Flying and swimming animals cruise at a Strouhal number tuned for high power efficiency," *Nature*, Vol. 425, 2003, pp. 707-711.

[90] Barrett, D.S., Triantafyllou, M.S., Yue, D.K.P., Grosenbaugh, M.A. and Wolfgang, M.J., "Drag reduction in fish-like locomotion", *Journal of Fluid Mechanics,* vo. 392, 1999, pp. 183-212.

[91] Naito, S. and Isshiki, H., "Effect of bow wings on ship propulsion and motions", *App. Mech. Rev.,* 2005, vol. 58, pp. 253-268.

[92] Grue J., Mo A., Palm E., "Propulsion of a foil moving in water waves", *Journal of Fluid Mechanics,* vol. 186, 1988, pp. 393-417.

[93] Zhu, O., Liu, Y., Yue, D., "Dynamics of a three-dimensional oscillating foil near the free surface", *AIAA Journal,* vol. 44, 2006, pp. 2997-3009.

[94] Cleaver, D.J., Calderon, D.E., Wang, Z. and Gursul, I., "Periodically plunging foil near a free surface", *Experiments in Fluids,* vol. 54, 2013, pp. 1491-.

[95] Cleaver, D.J., Calderon, D.E., Wang, Z. and Gursul, I., "Rigid and flexible foils oscillating near a free surface", AIAA-2012-1195, 50th AIAA Aerospace Sciences Meeting, 9-12 January, Nashville, TN.

[96] Liu, P., Bose, N., 1997. Propulsive performance from oscillating propulsors with spanwise flexibility. Proceedings of the Royal Society London 453, 1763-1770.

[97] Heathcote, S., Wang, Z., and Gursul, I., "Effect of Spanwise Flexibility on Flapping Wing Propulsion", *Journal of Fluids and Structures*, vol. 24, 2008, pp. 183-199.

[98] Gordnier, R.E., Attar, P.J., Chimakurthi, S.K. and Cesnik, C.E.S., 2010, "Implicit LES simulations of a flexible flapping wing", AIAA Paper 2010-2960.
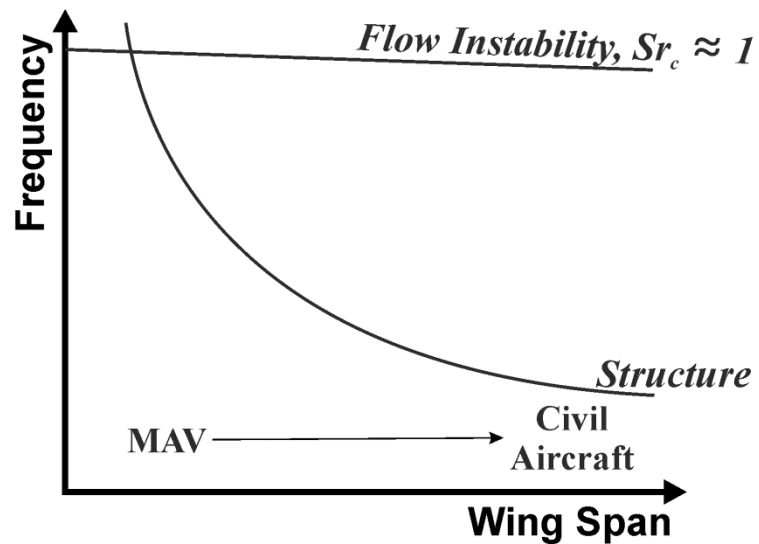
Figure 1: Schematic variation of natural frequency of flow instabilities and wing structure as a function of wing span. Optimal Strouhal number of the flow instabilities is on the order of unity. The Strouhal number is defined based on the chord length and free stream velocity. Schematic variation of the frequency of flow instabilities is shown after the variations of wing chord and flight speed with wing span are taken into account.
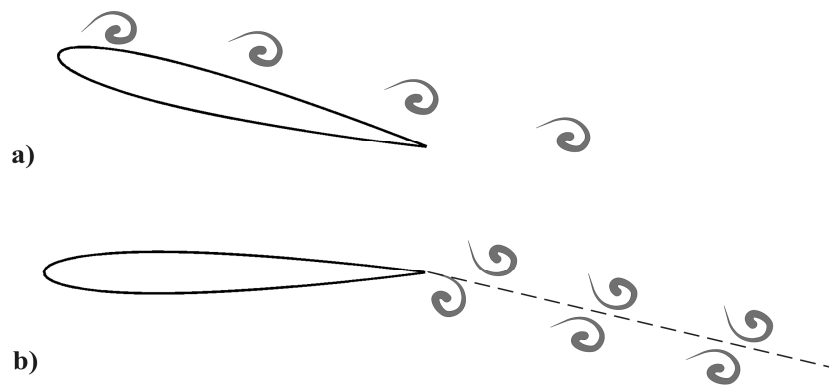
Figure 2: High-lift mechanisms for an airfoil oscillating with small-amplitude: a) LEV for post-stall angles of attack, and b) deflected jets for pre-stall angles of attack.
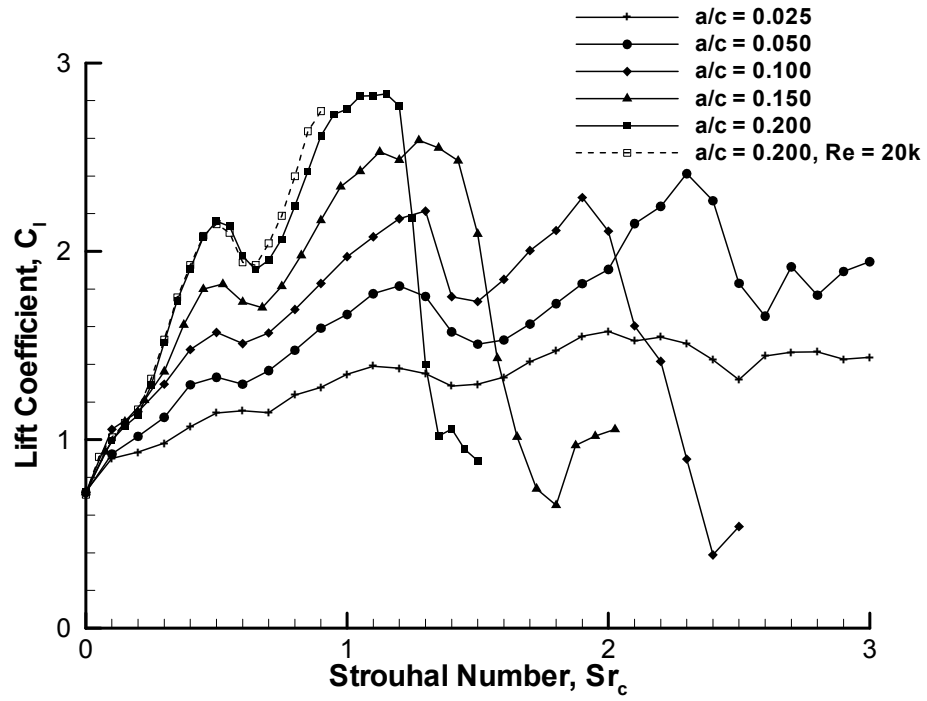
Figure 3: Time-averaged lift coefficient for a NACA 0012 airfoil for α = 15°, *Re* = 10,000 and different amplitudes.
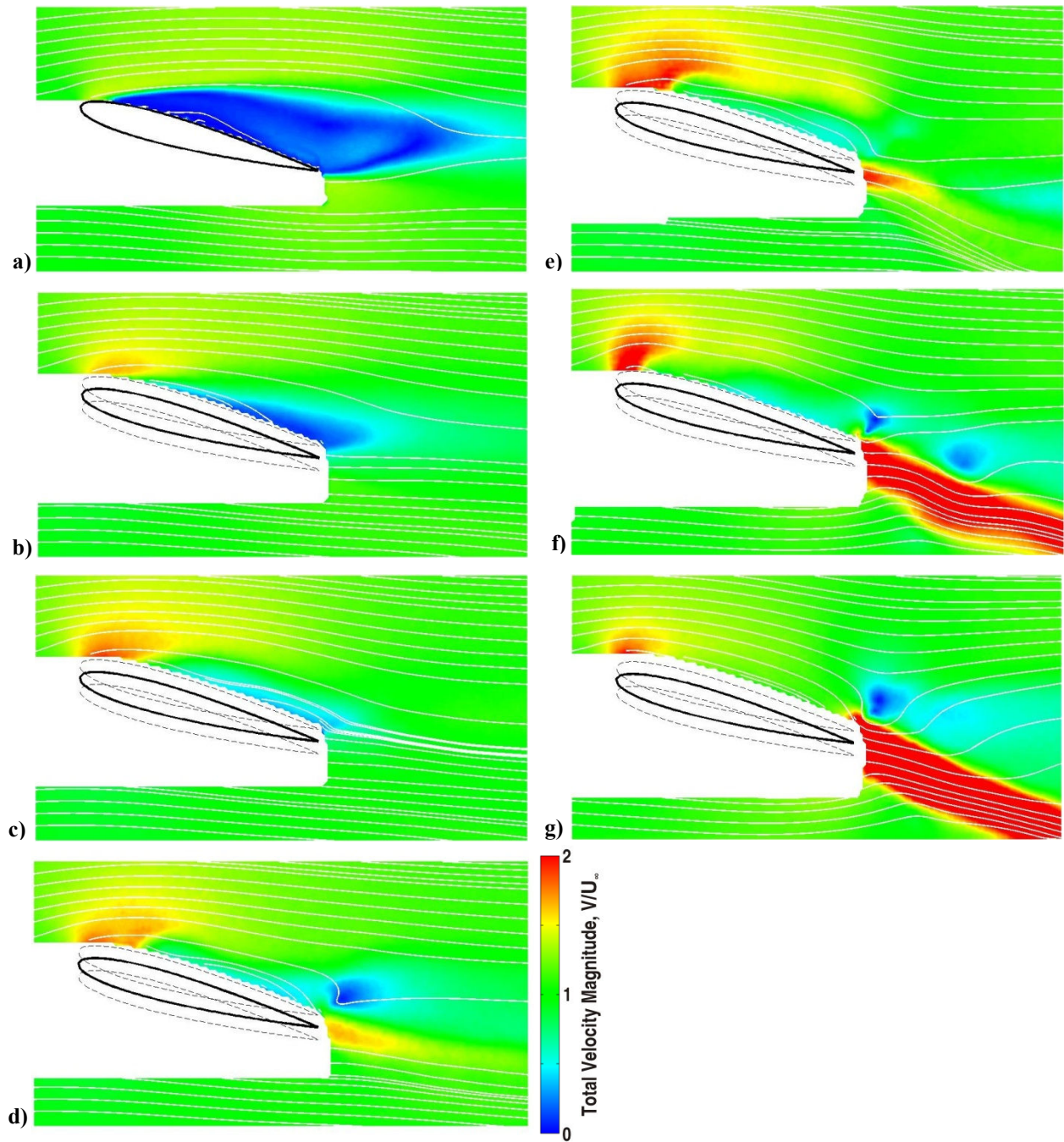
Figure 4: Magnitude of time-averaged velocity for *a/c* = 0.050: a) stationary; b) *Sr_c* = 0.5; c) *Sr_c* = 1.0; d) *Sr_c* = 1.5; e) *Sr_c* = 2.0; f) *Sr_c* = 2.5 and g) *Sr_c* = 3.0. NACA 0012 airfoil for α = 15°, *Re* = 10,000.
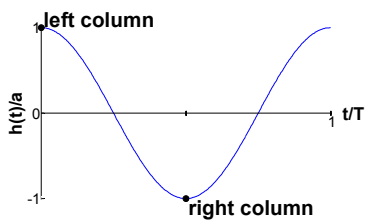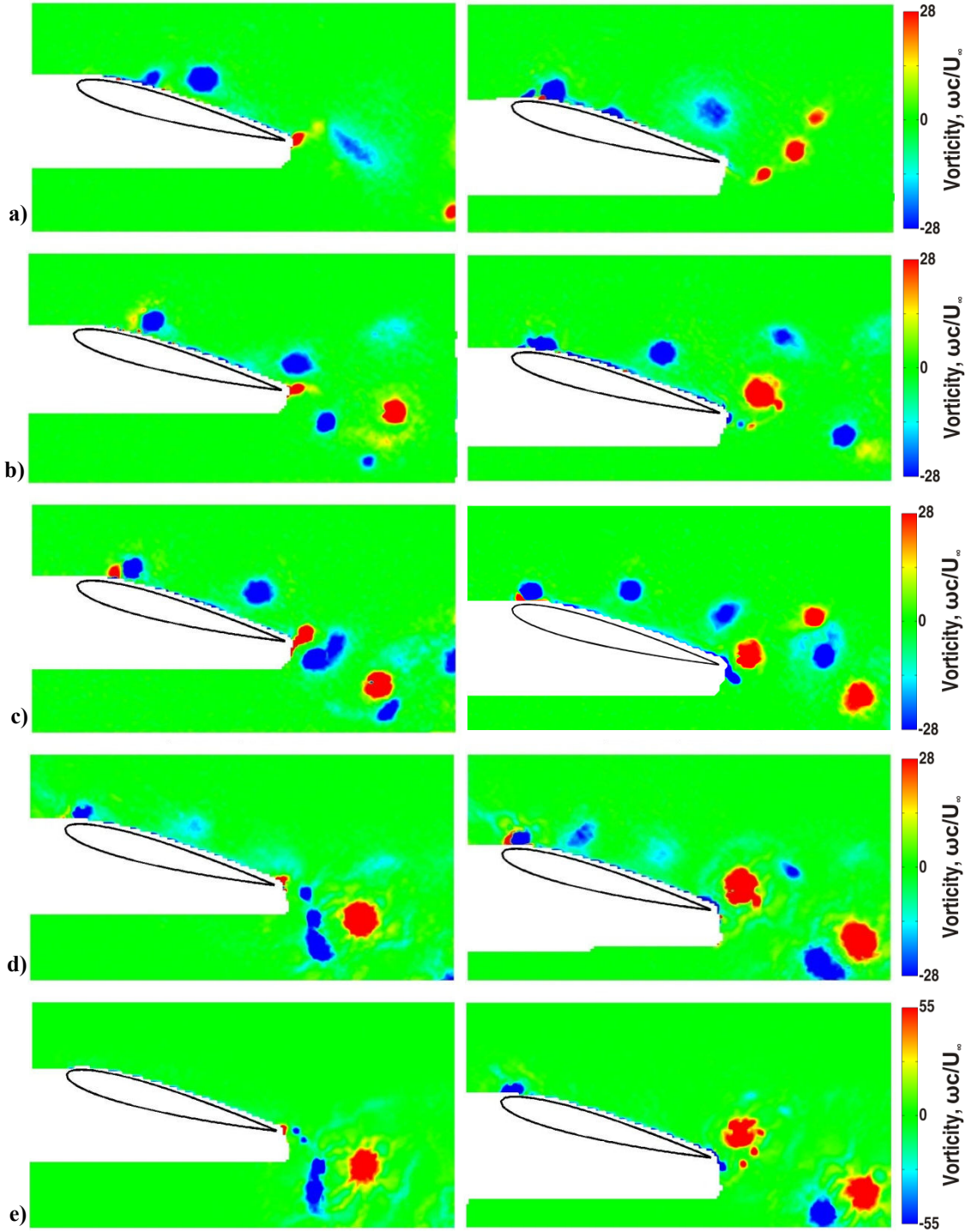
Figure 5: Phase-averaged vorticity at top (left) and bottom (right) of airfoil displacement for $a/c = 0.050$: a) $Sr_c = 1.0$; b) $Sr_c = 1.5$; c) $Sr_c = 2.0$; d) $Sr_c = 2.5$; e) $Sr_c = 3.0$. a) through c) demonstrate mode-1, e) demonstrates mode-2, and d) demonstrates a mixed mode. Note the different scale for e). NACA 0012 airfoil for $\alpha = 15°$, $Re = 10,000$.
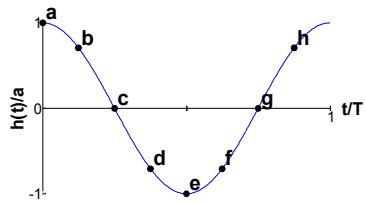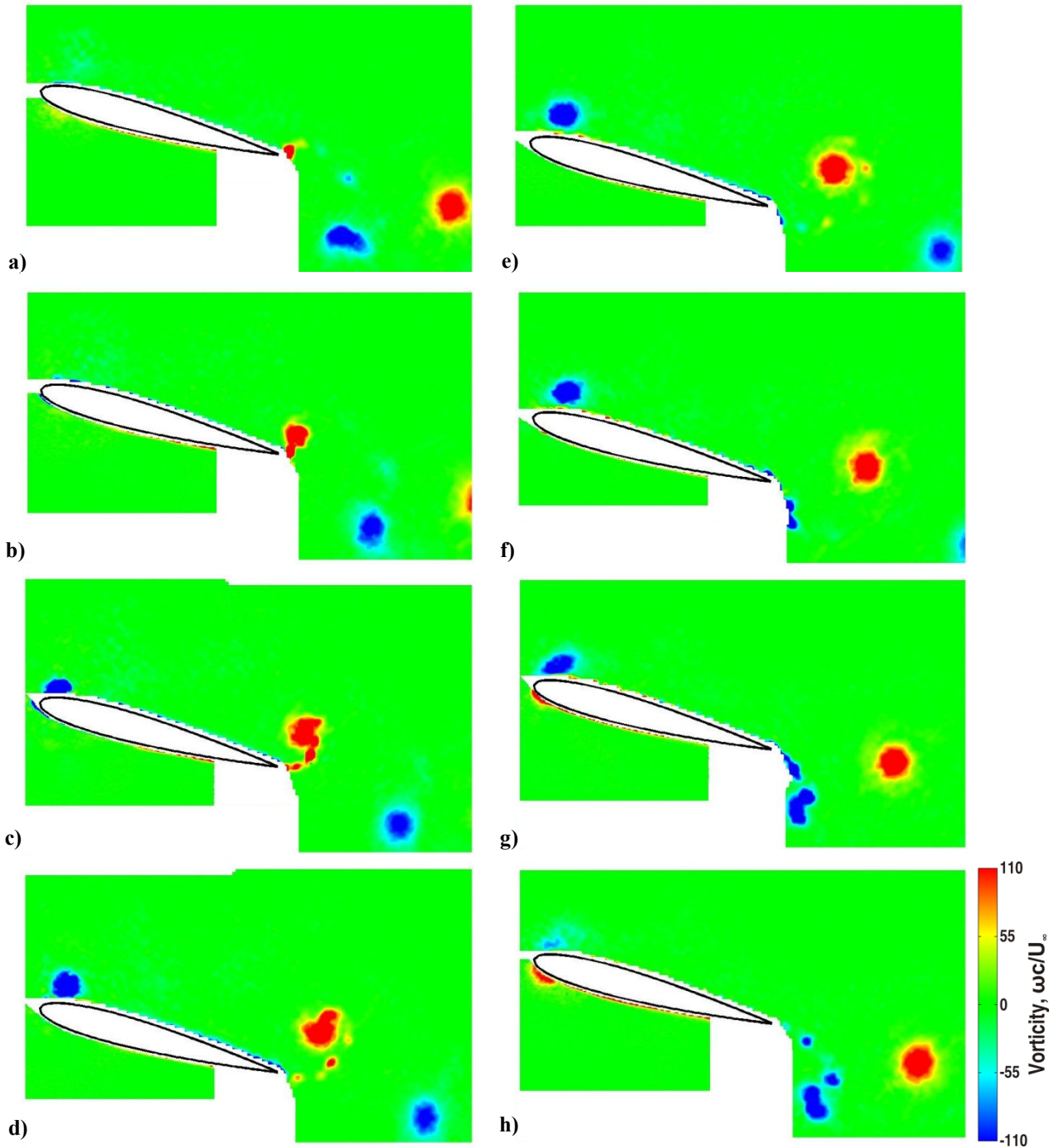
Figure 6: Phase-averaged vorticity, $\omega c/U_\infty$, for both the upper and lower surface of a mode-2 flow field: $a/c = 0.10$ and $Sr_c = 1.75$. Position in the cycle denoted by the diagram. NACA 0012 airfoil for $\alpha = 15°$, $Re = 10,000$.
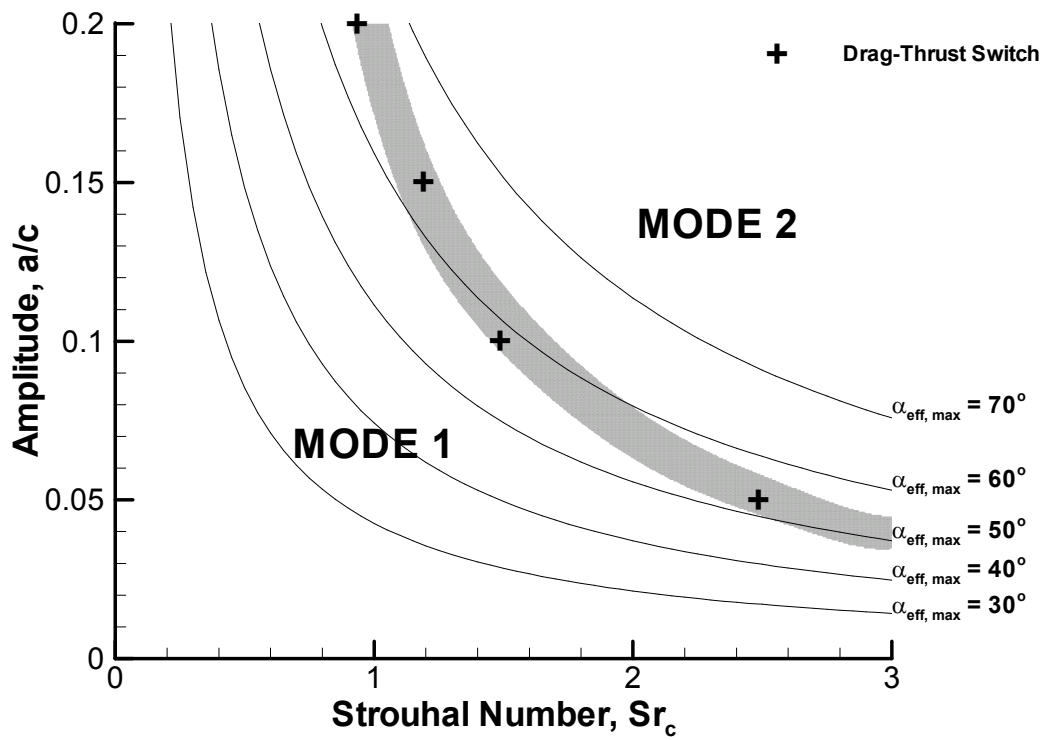
Figure 7: Mode diagram derived from phase-averaged flow fields measured by PIV. The mode-switch boundary is represented by the shaded area. NACA 0012 airfoil for $\alpha = 15°$, $Re = 10,000$.
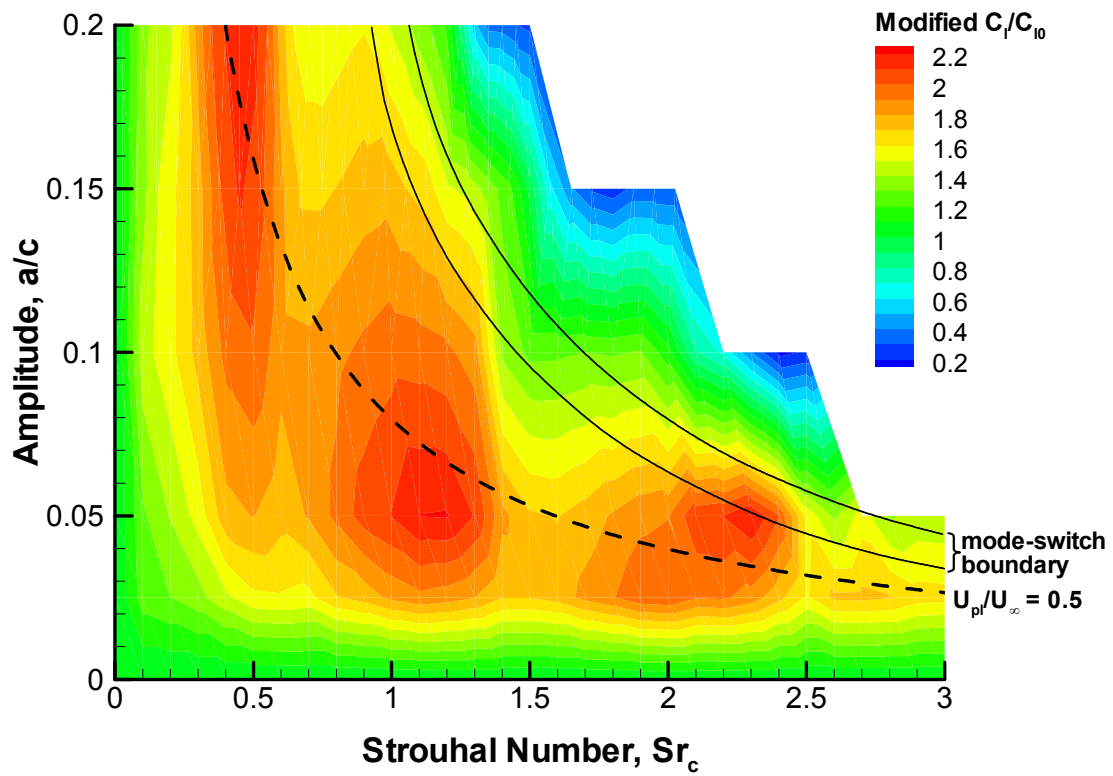
Figure 8: Contour plot of modified lift coefficient normalized by the value for a stationary airfoil. Solid lines represent the mode-switch boundary from Figure 7. Dashed line represents a constant normalized plunge velocity. NACA 0012 airfoil for $\alpha = 15°$, $Re = 10,000$.
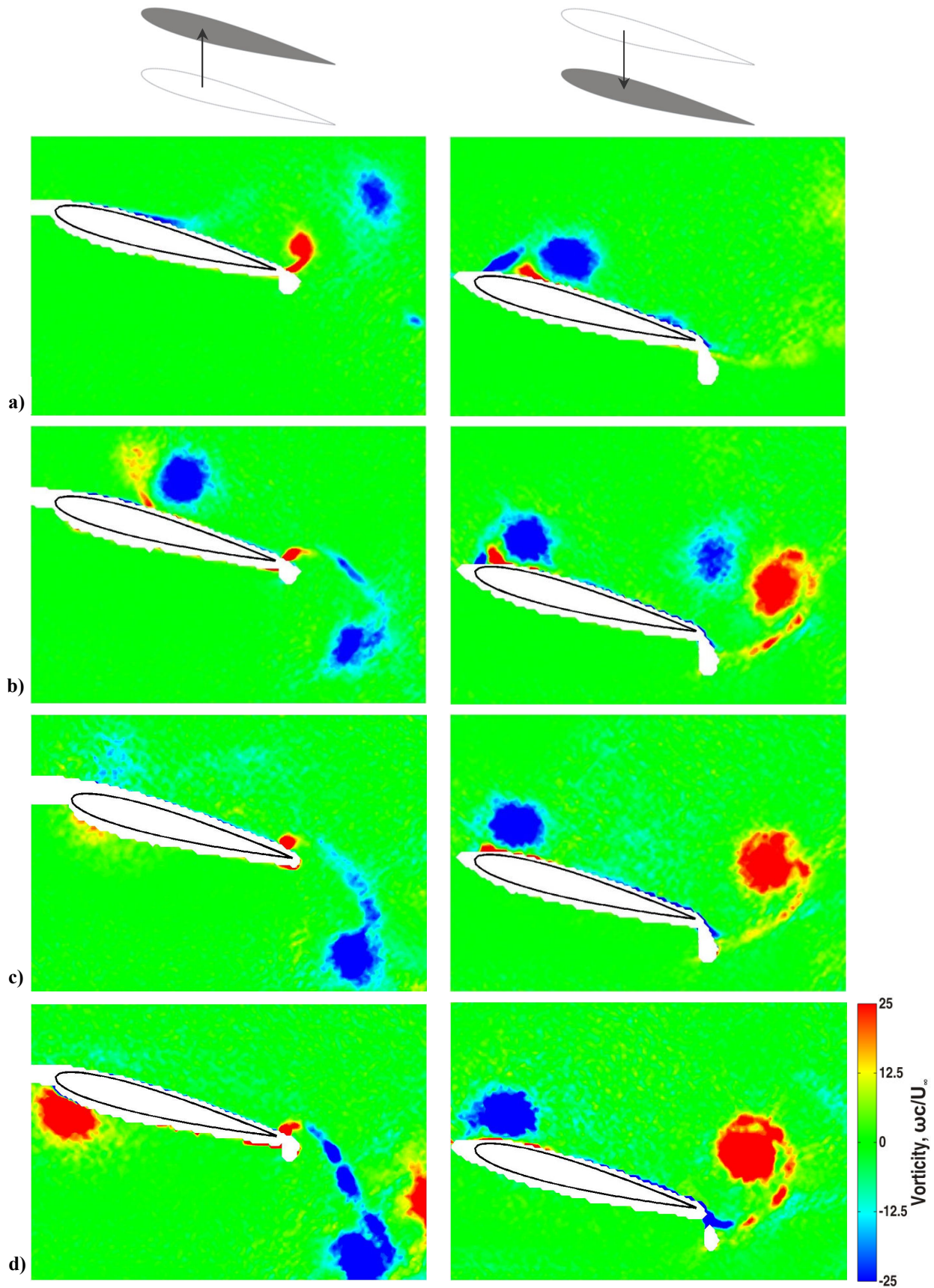
Figure 9: Normalized vorticity at top (left) and bottom (right) of motion with *a/c* = 0.15, for: a) Sr_A = 0.15 (Sr_c = 0.50), b) Sr_A = 0.30 (Sr_c = 1.00), c) Sr_A = 0.375 (Sr_c = 1.25), d) Sr_A = 0.525 (Sr_c = 1.75). NACA 0012 airfoil for α = 15°, *Re* = 10,000.

51
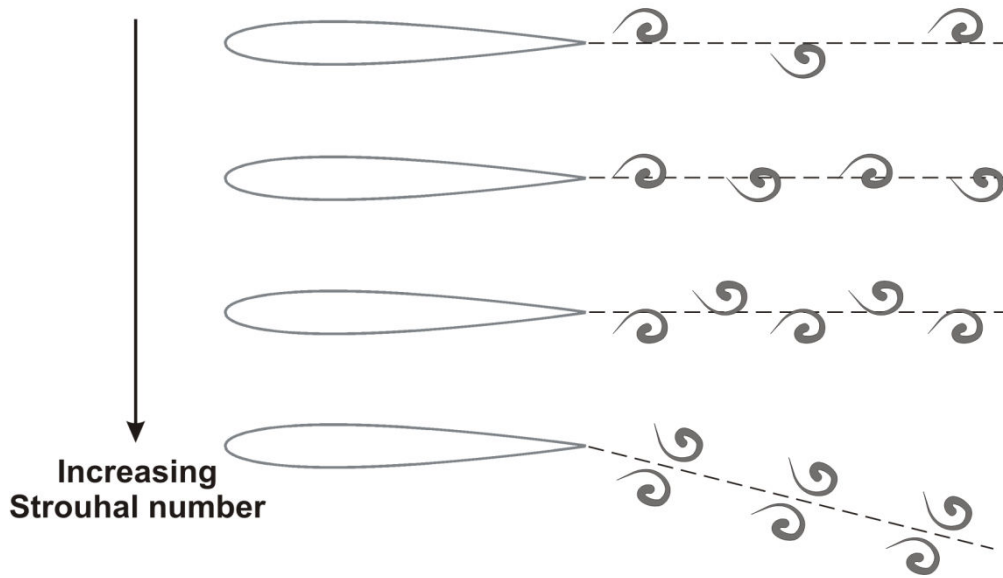
Figure 10: Wake patterns with increasing Strouhal number.
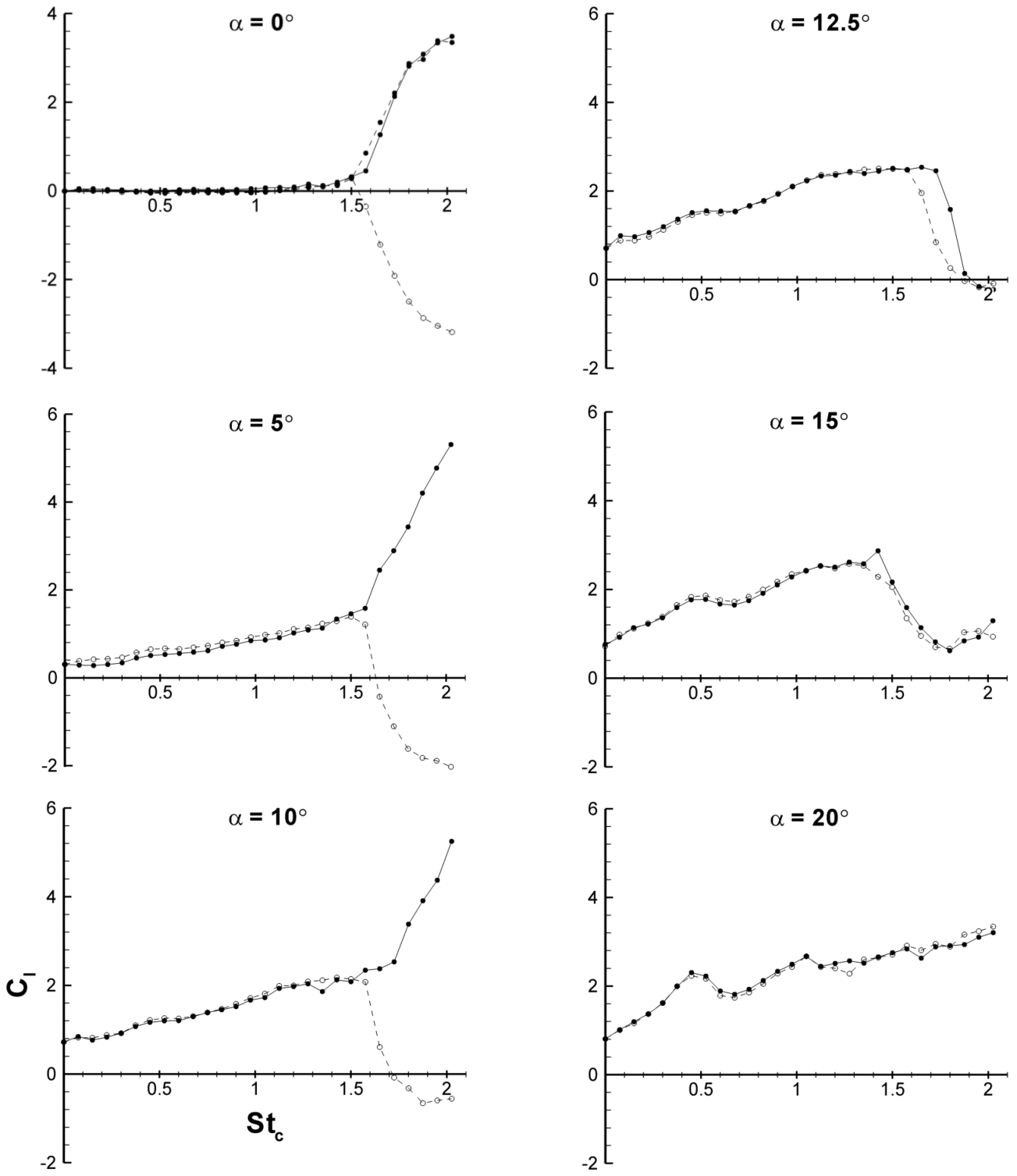
Figure 11: Time-averaged lift coefficient for *a/c* = 0.15 and all angles of attack considered. Solid line represents increasing frequency, dashed line represents decreasing frequency with a starting position for α = 0° of h_i = ±*a*, and for α > 0° h_i = 0 (airfoil moving upwards). NACA 0012 airfoil, *Re* = 10,000.
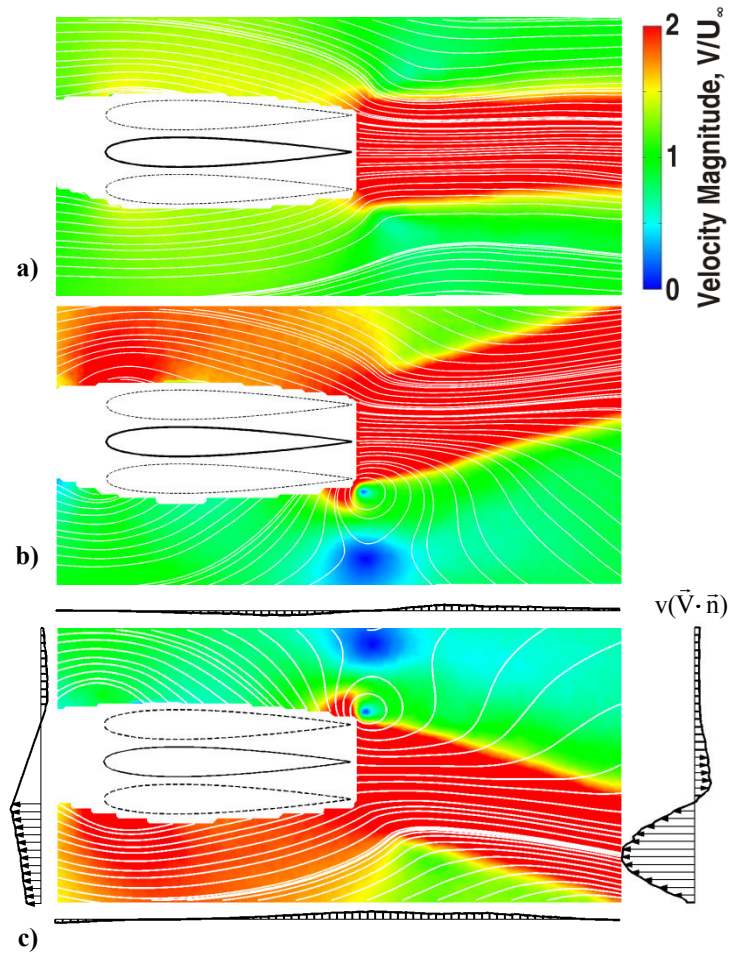
Figure 12: Time-averaged velocity magnitude for $a/c = 0.15$, $\alpha = 0°$, and: a) $St_c = 1.500$ - pre-bifurcation, b) $St_c = 2.025$ – mode A, and c) $St_c = 2.025$ – mode B. For c) arrows show momentum flux component in the vertical direction for the boundaries of the control volume. NACA 0012 airfoil, $Re = 10,000$.
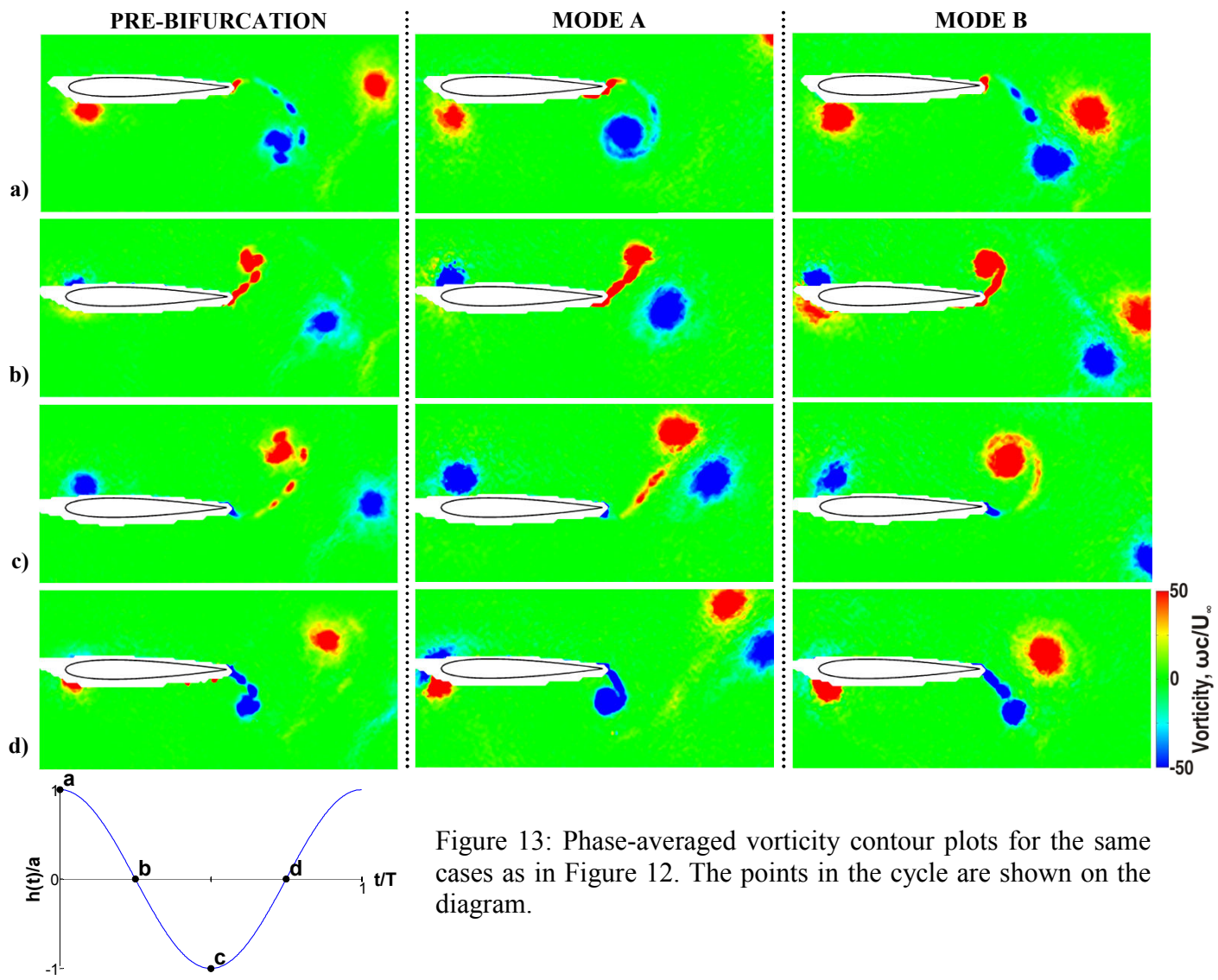
Figure 13: Phase-averaged vorticity contour plots for the same cases as in Figure 12. The points in the cycle are shown on the diagram.
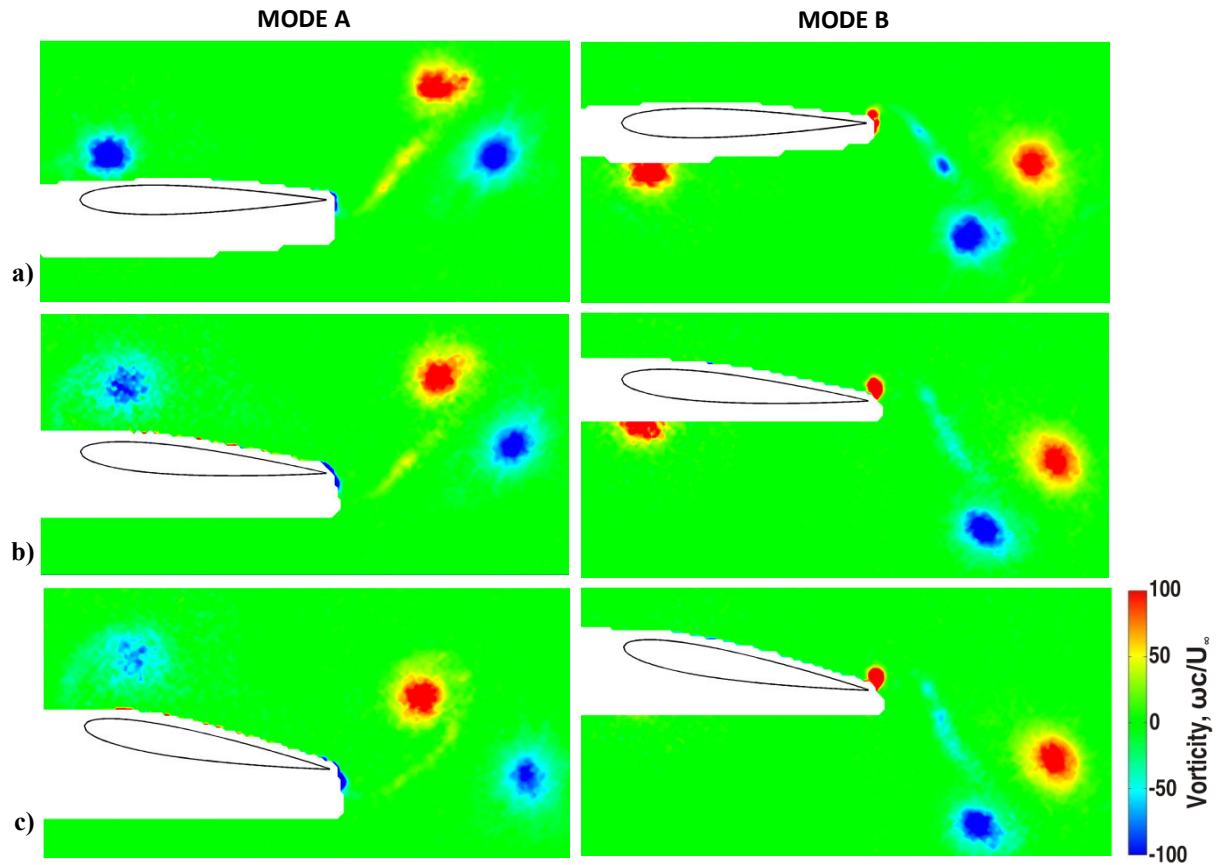
Figure 14: Phase-averaged vorticity contour plots comparing the mode A flow field (left) at the bottom of the motion, and mode B flow field (right) at the top of the motion for $a/c = 0.15$, $St_c = 2.025$ and: a) $\alpha = 0°$, b) $\alpha = 5°$, and c) $\alpha = 10°$. NACA 0012 airfoil, $Re = 10,000$.
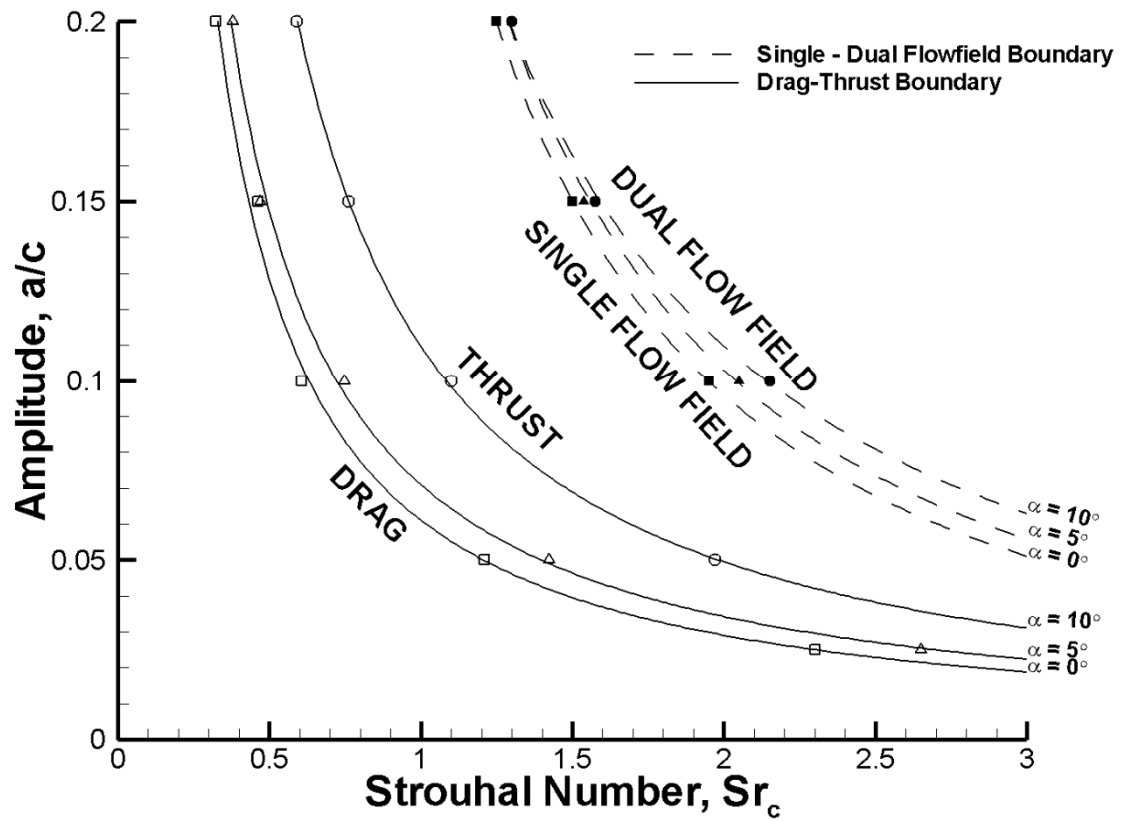
Figure 15: Boundary between drag / thrust producing and single / dual flow field for: α = 0° (square), α = 5° (triangle), and α = 10° (circle). Lines are power law curve fits. NACA 0012 airfoil, *Re* = 10,000.
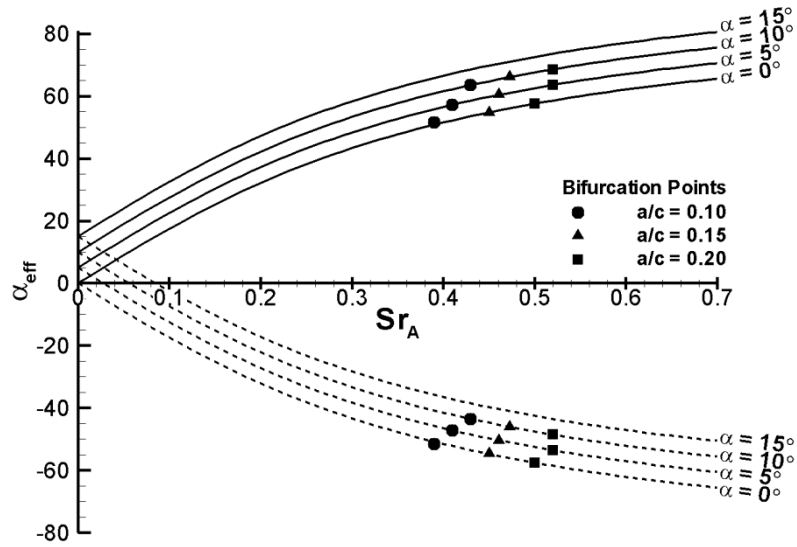
Figure 16: Effective angle of attack as a function of Strouhal number based on amplitude. Solid line: $\alpha_{eff,max}$, dashed line: $\alpha_{eff,min}$. Symbols denote the point of bifurcation as determined from the force measurements. NACA 0012 airfoil, $Re = 10,000$.
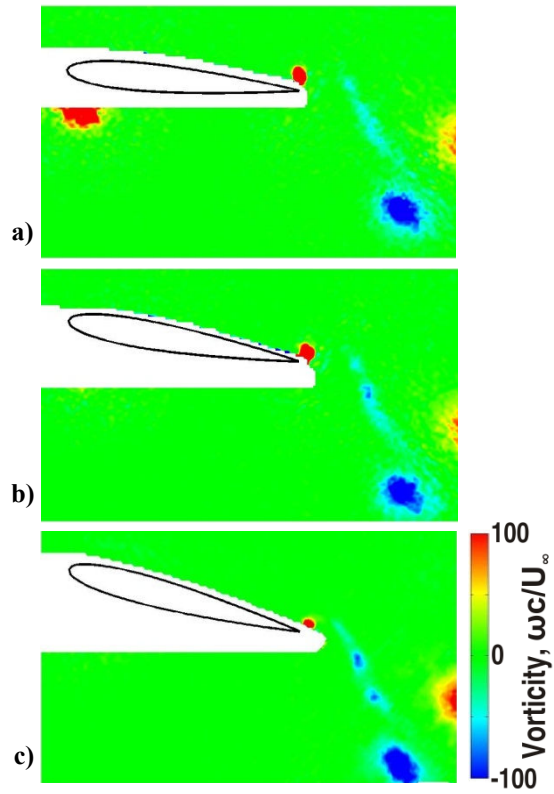
Figure 17: Vorticity contours showing the similarity of flow fields across different angles of attack for a/c = 0.150, St_c = 2.025 and: a) α = 5° - mode B, b) α = 10° - mode B, and c) α = 15°. NACA 0012 airfoil, Re = 10,000.
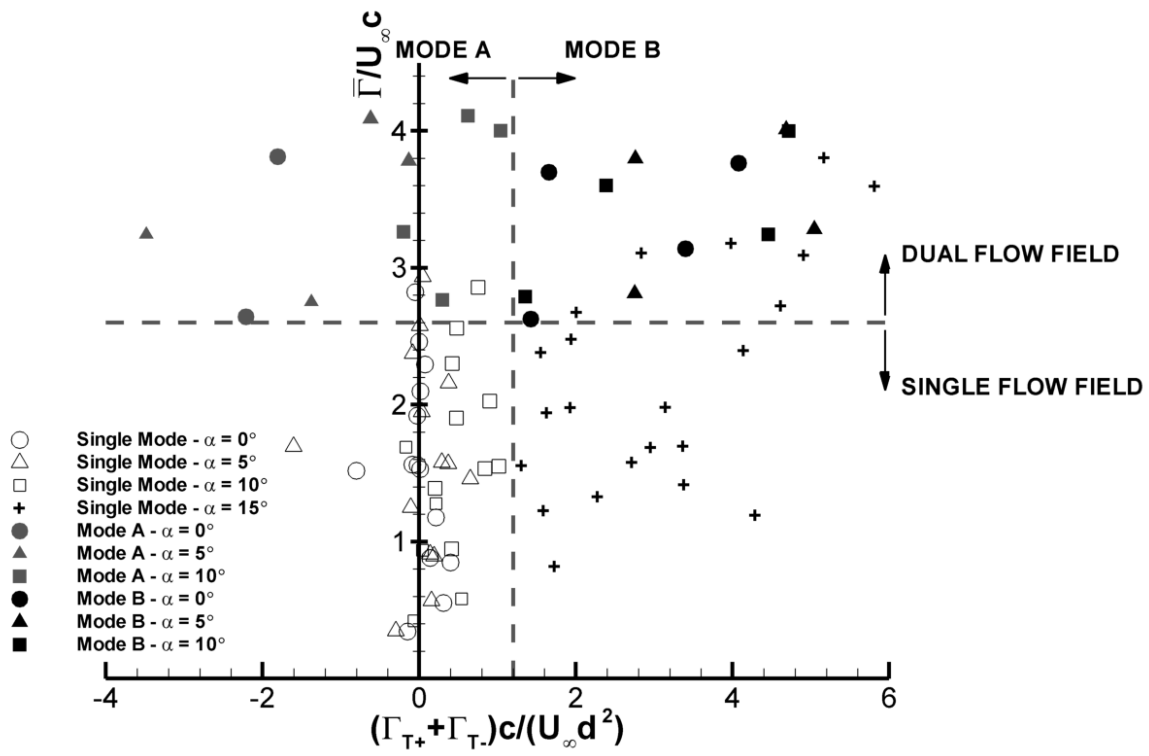
Figure 18: Normalized circulation as a function of asymmetry parameter. NACA 0012 airfoil, *Re* = 10,000.
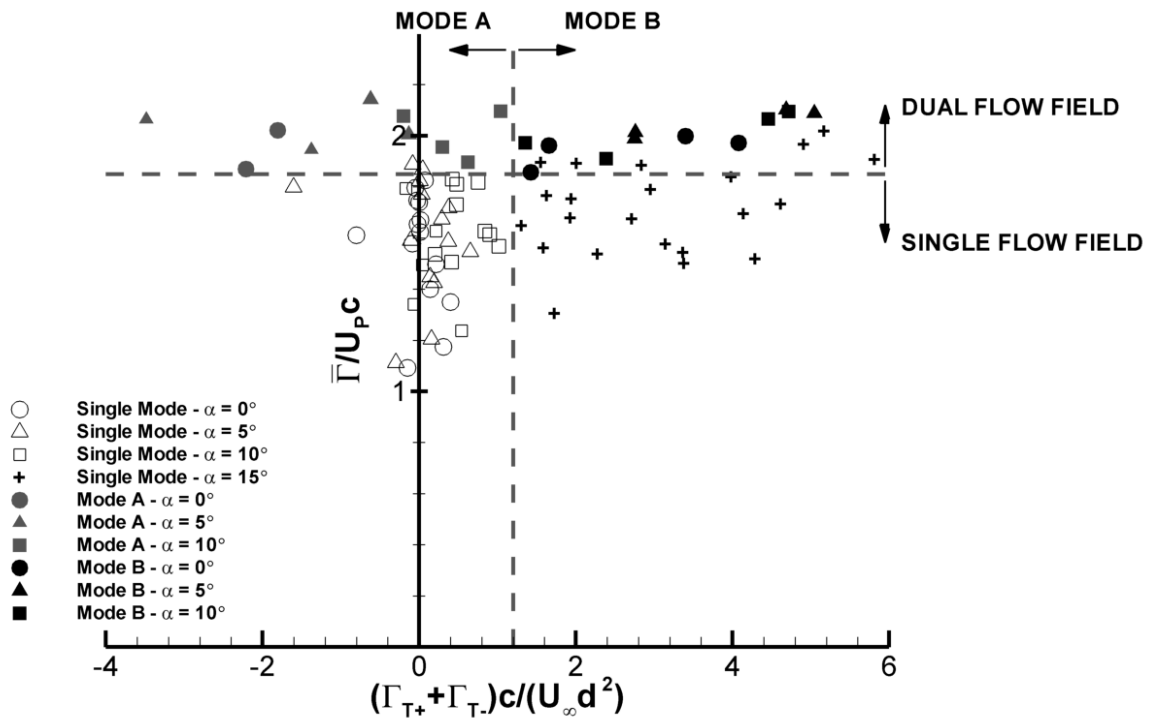
Figure 19: Circulation normalized by plunge velocity as a function of asymmetry parameter. NACA 0012 airfoil, *Re* = 10,000.
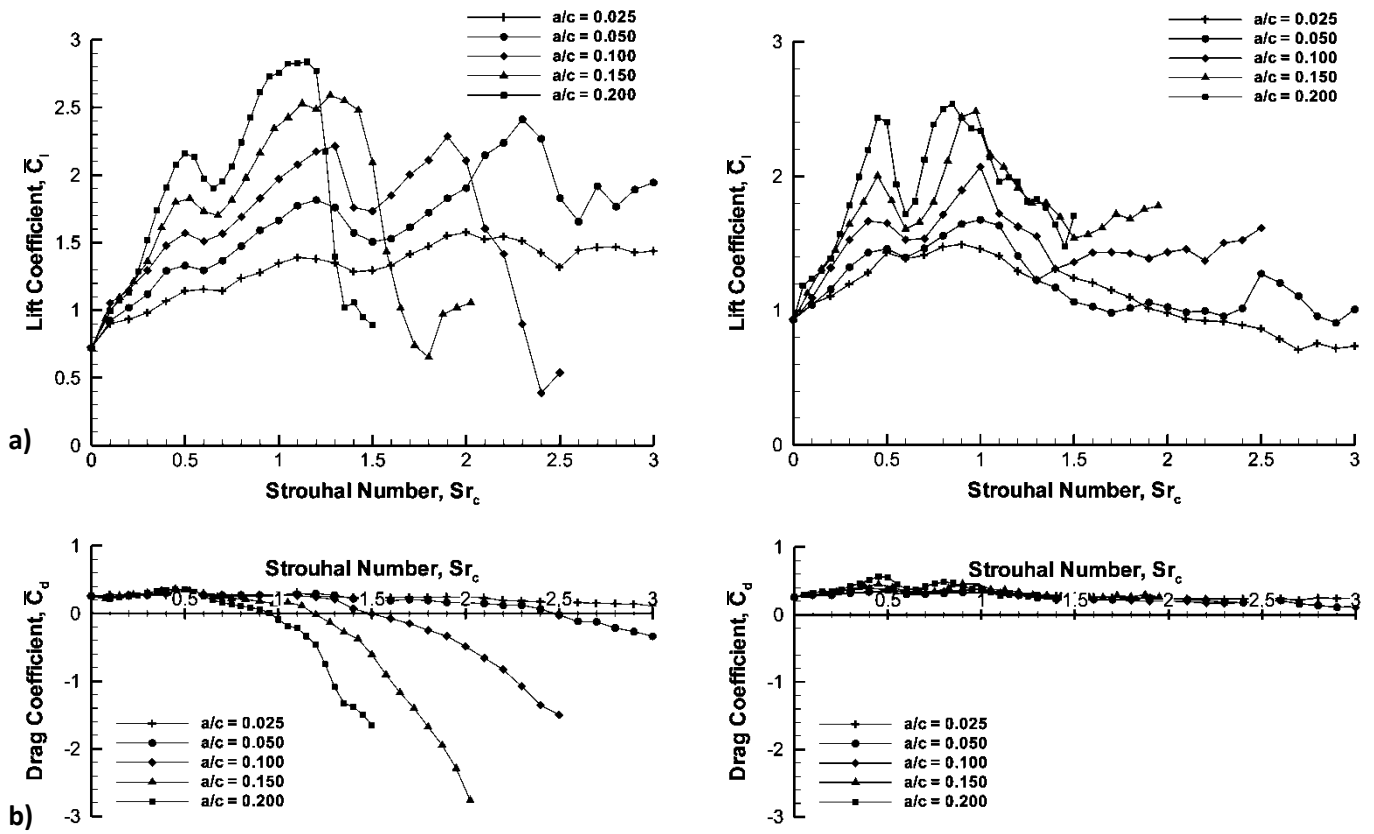
Figure 20: a) Time-averaged lift coefficient, and b) drag coefficient plotted against Strouhal number based on chord for the NACA 0012 airfoil (left column) and the flat plate (right column) at $\alpha = 15°$. $Re = 10,000$.
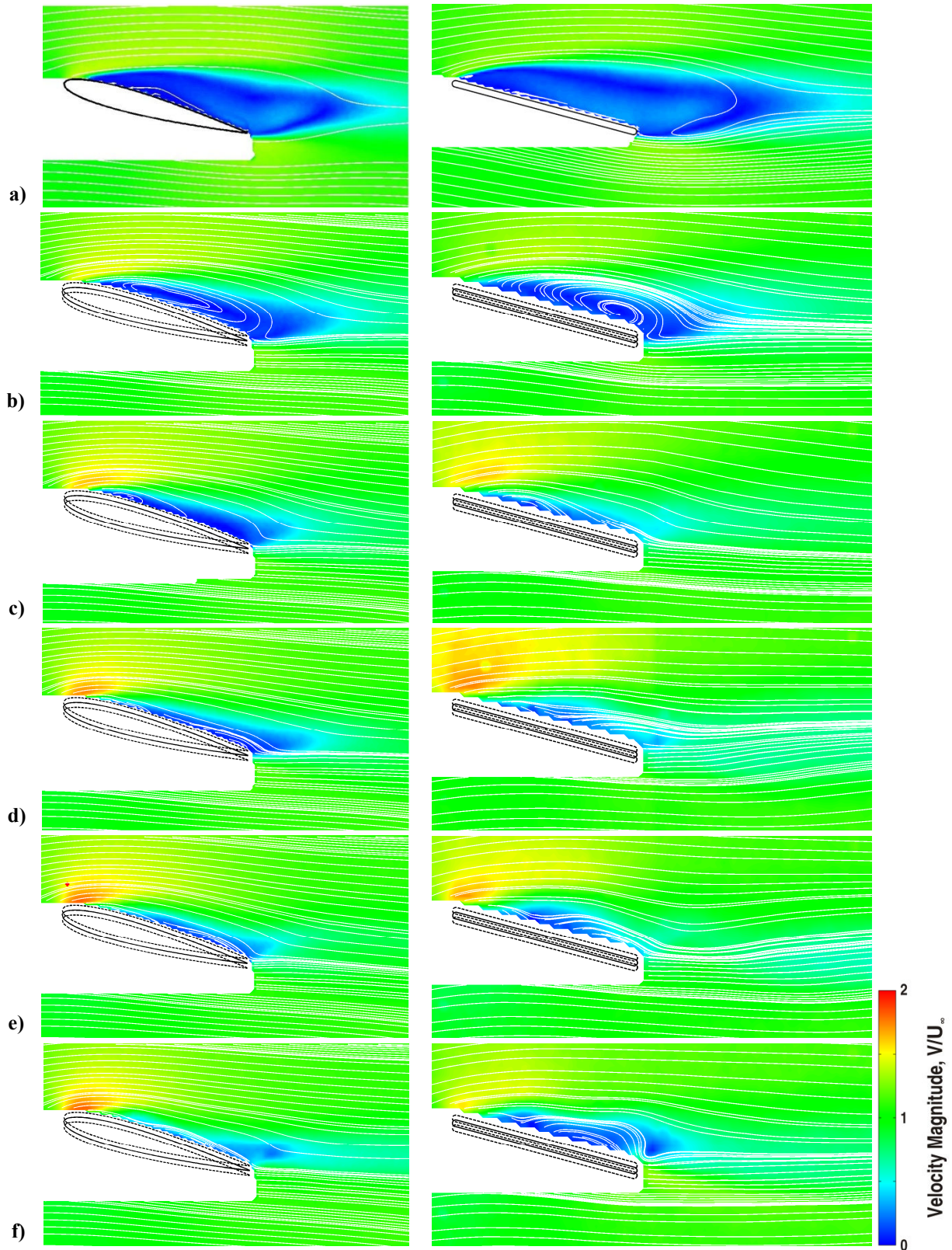
Figure 21: Time-averaged velocity magnitude for the NACA 0012 airfoil (left column) and flat plate (right column) for $a/c = 0.025$ and $\alpha = 15°$ at Strouhal numbers of: a) $Sr_c = 0$, b) $Sr_c = 0.25$, c) $Sr_c = 0.50$, d) $Sr_c = 0.75$, e) $Sr_c = 1.00$, f) $Sr_c = 1.25$, g) $Sr_c = 1.50$, h) $Sr_c = 1.75$, i) $Sr_c = 2.00$, j) $Sr_c = 2.25$, k) $Sr_c = 2.50$, l) $Sr_c = 2.75$, and m) $Sr_c = 3.00$. $Re = 10,000$. Continued on next page.

g)

h)

i)

j)

k)

l)

m)
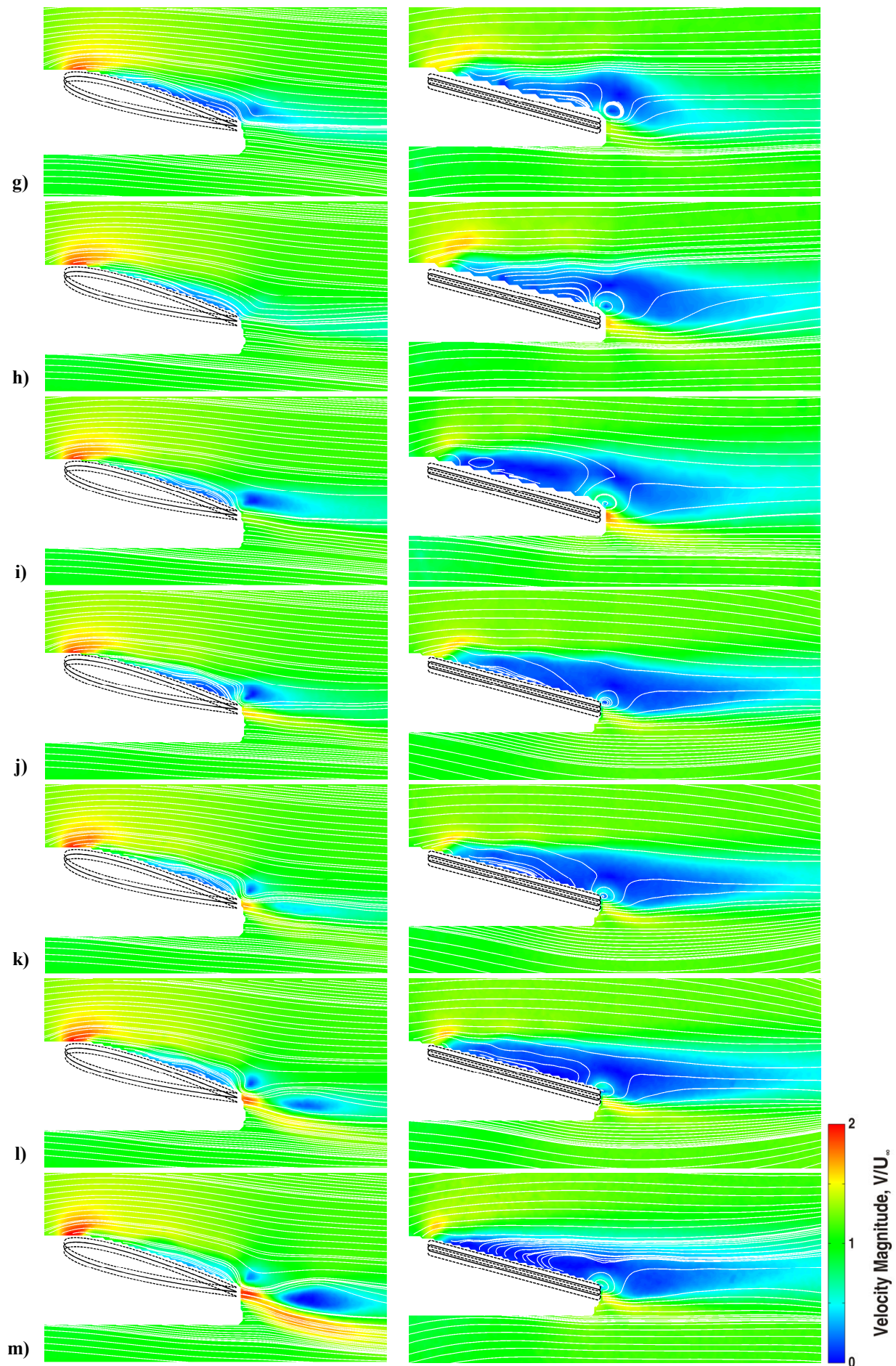
Figure 21 Continued

64
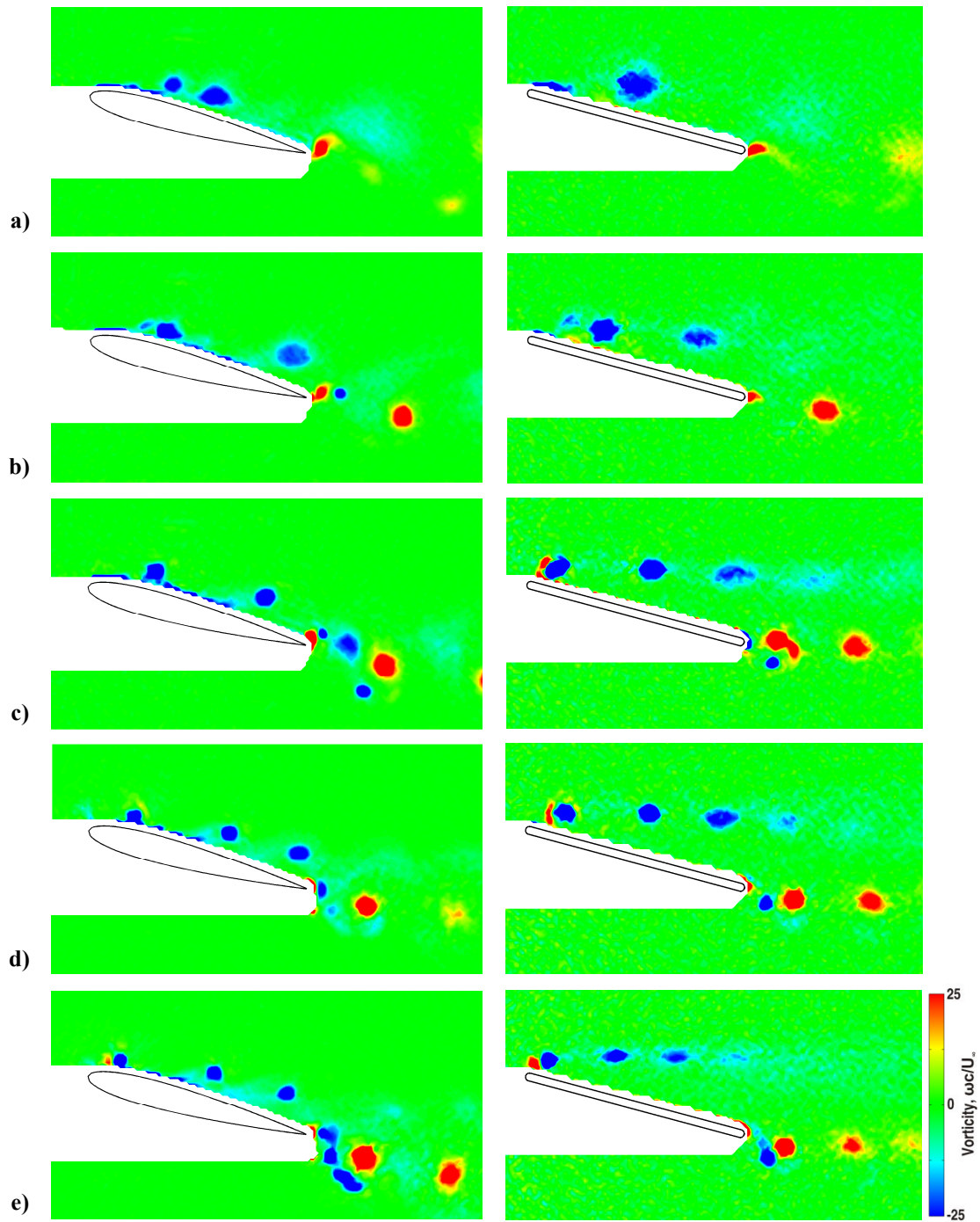
Figure 22: Phase-averaged vorticity contour plots at the top of the motion for the NACA 0012 airfoil (left column) and flat plate (right column) for $a/c = 0.025$ and $\alpha = 15°$ at Strouhal numbers of: a) $Sr_c = 1.00$, b) $Sr_c = 1.50$, c) $Sr_c = 2.00$, d) $Sr_c = 2.50$, and e) $Sr_c = 3.00$. $Re = 10,000$.
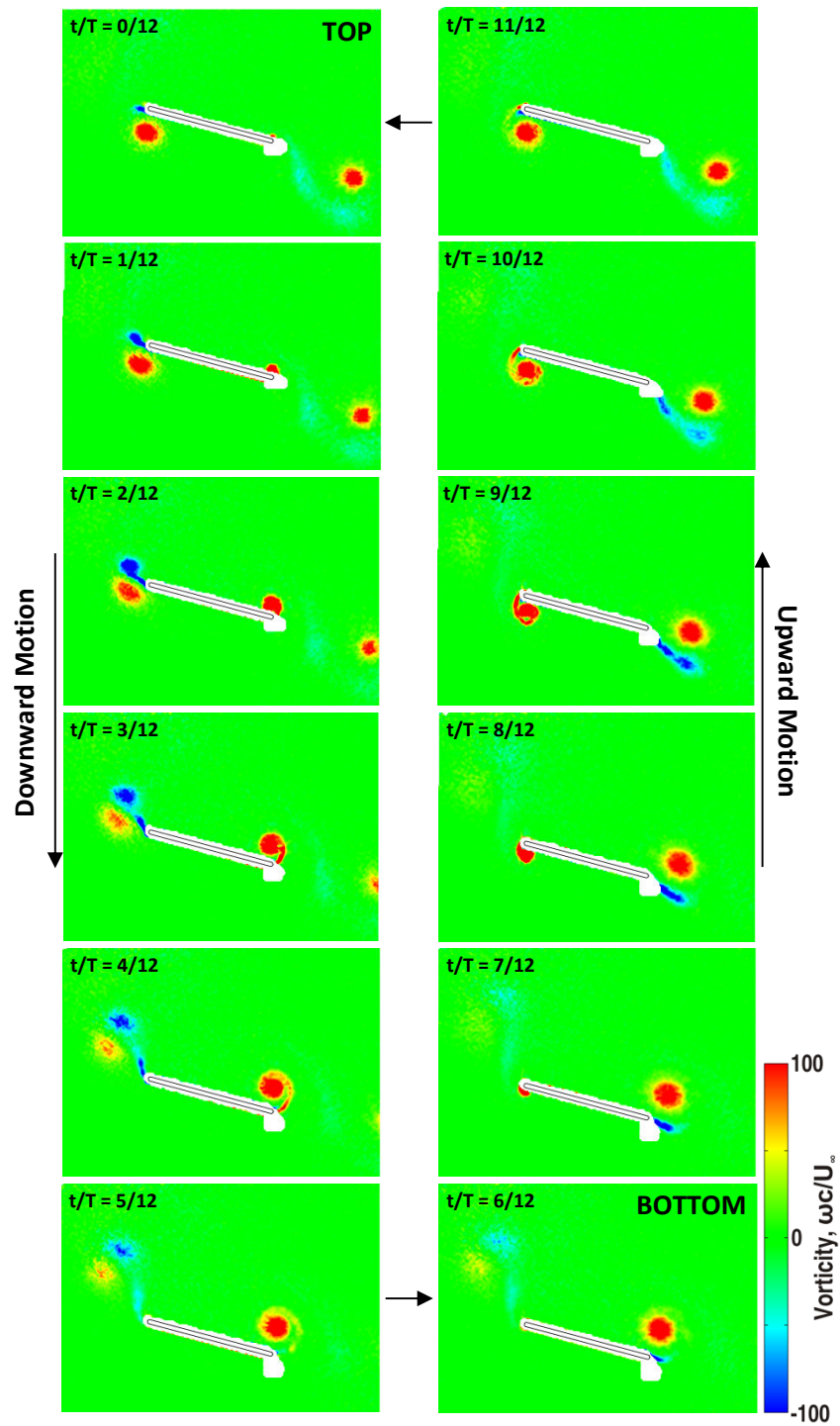
Figure 23: Phase-averaged vorticity contour plots for the 2D flat plate at twelve phases in the cycle for $\alpha = 15°$, $a/c = 0.15$ and $Sr_c = 2.00$. $Re = 10,000$.
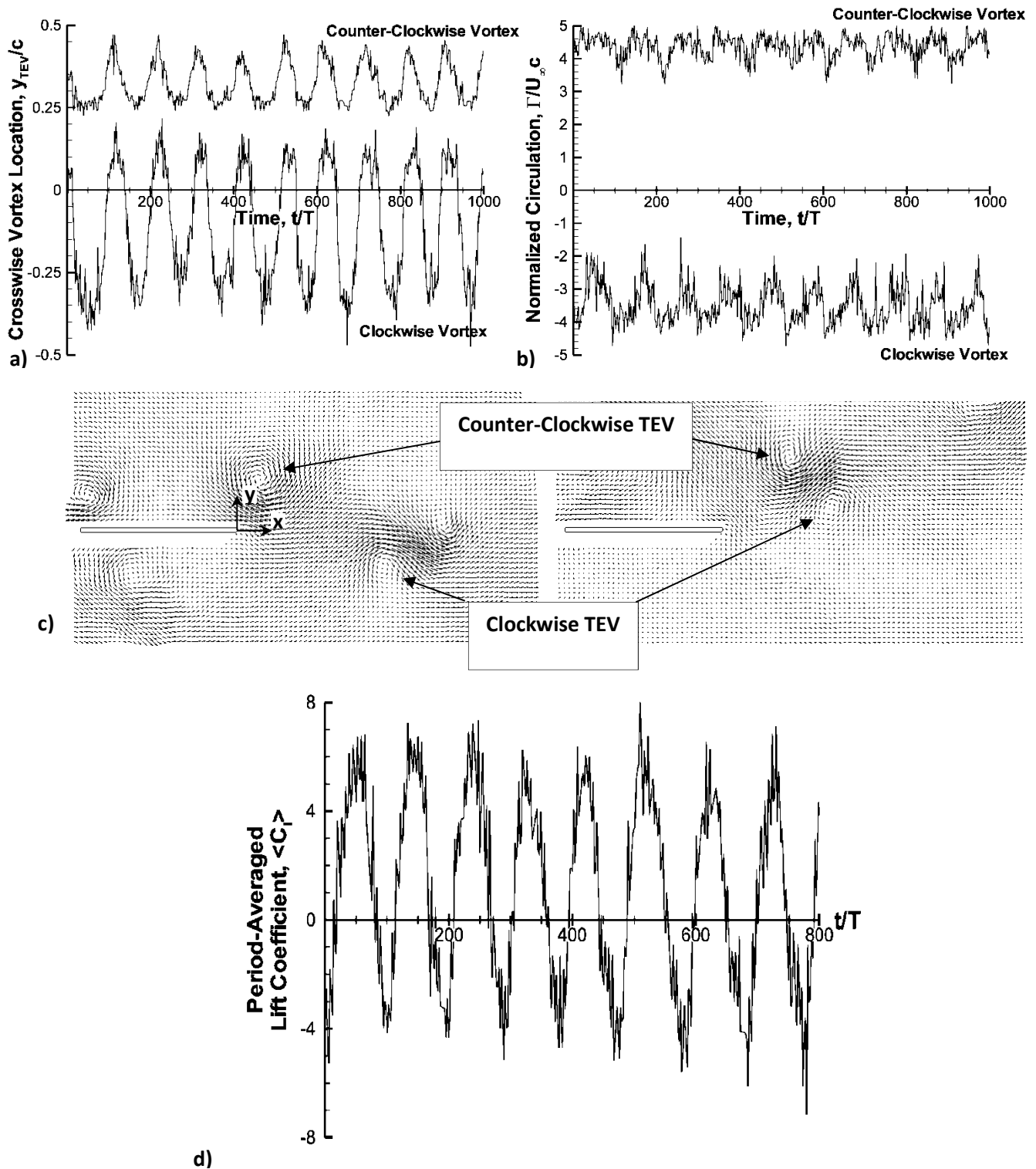
Figure 24: a) Instantaneous cross-stream position of trailing-edge vortex as measured in phase-locked measurements at $h = -a$, b) Instantaneous normalized circulation as measured in phase-locked measurements at $h = -a$, c) Inset identifying clockwise and counter-clockwise vortex for two extreme cases, d) Period-averaged lift coefficient. Flat plate airfoil, $a/c = 0.15$, $Sr_c = 2.025$, $\alpha = 0°$, $Re = 10,000$.
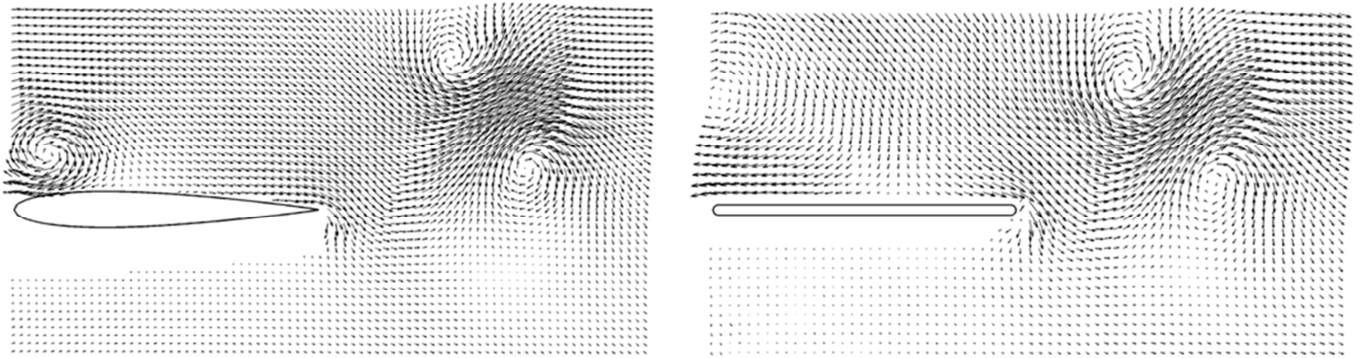
Figure 25: Comparison of phase-averaged mode A flow fields for the NACA 0012 airfoil and flat plate airfoil. $a/c = 0.15$, $Sr_c = 2.025$, $\alpha = 0°$, $Re = 10,000$.
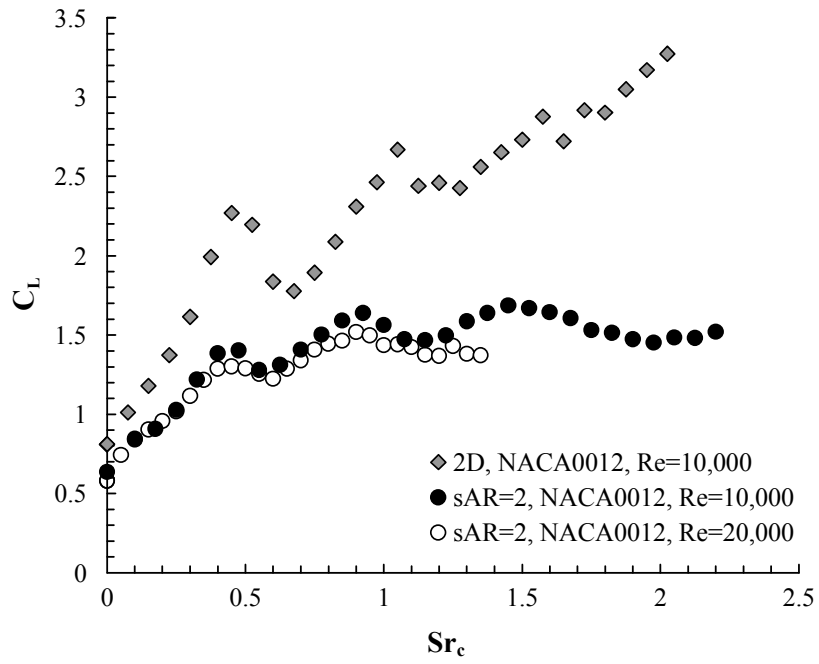
Figure 26: Time-averaged lift measurements of a plunging NACA0012 profile airfoil and *sAR*=2 rectangular wing. *a/c* = 0.15, α = 20º.
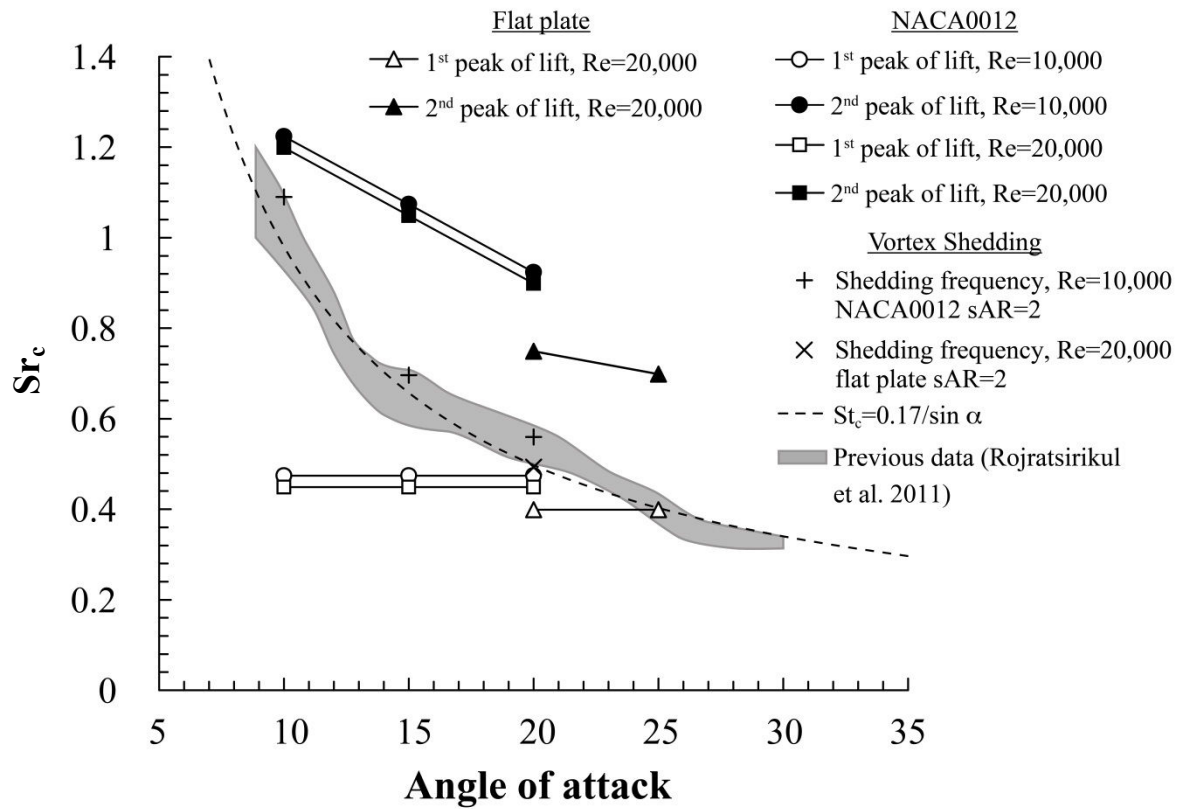
Figure 27: Comparison between the frequency at which lift peaks occur for the oscillating wing and the natural shedding frequency of the stationary wing. *sAR* = 2, *a/c* = 0.15.
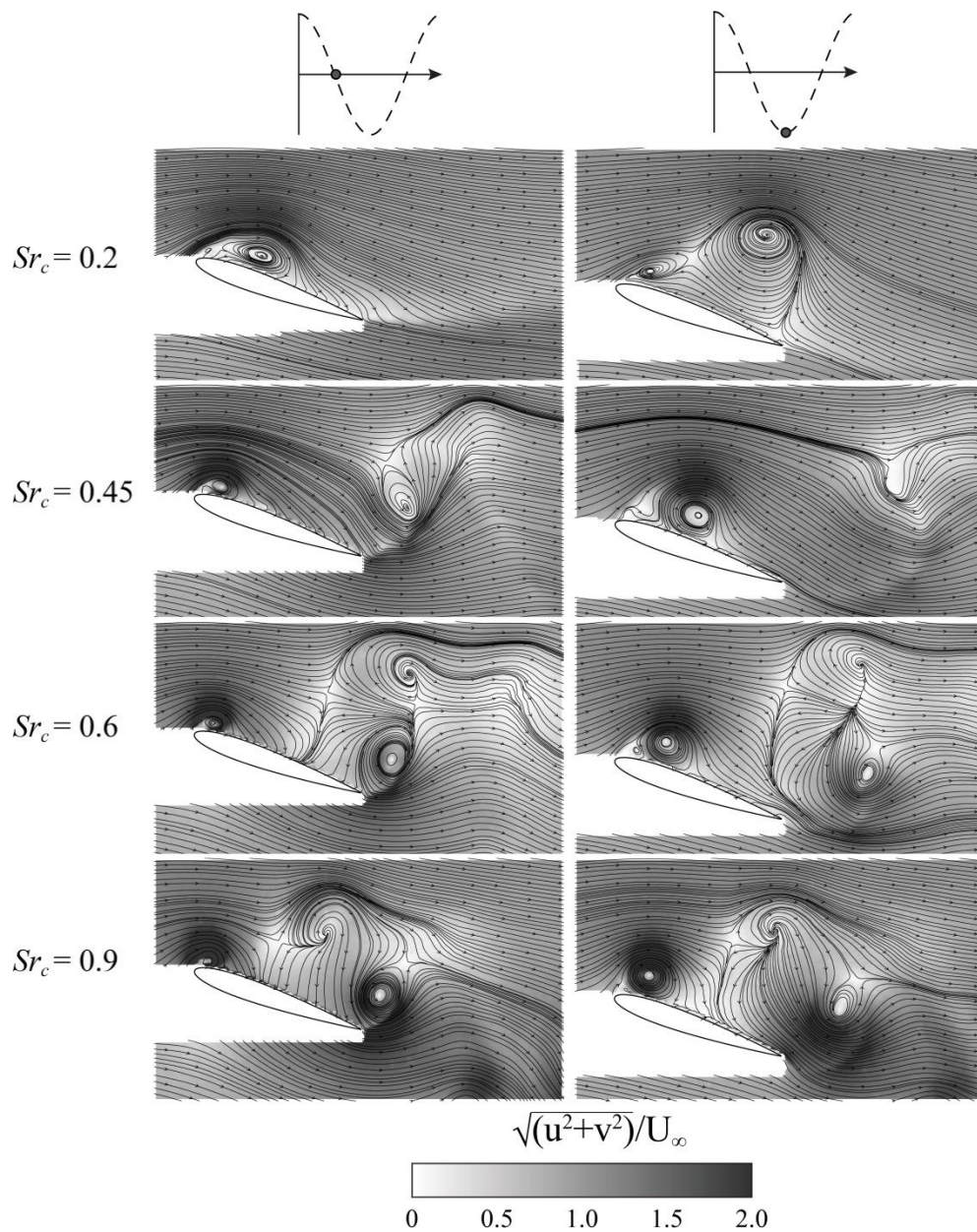
Figure 28: Velocity magnitude and streamlines at the mid-span plane for the NACA0012 *sAR*=2 wing taken at two phases for various Strouhal numbers, *Re* = 20,000, α = 20º, *a/c* = 0.15.
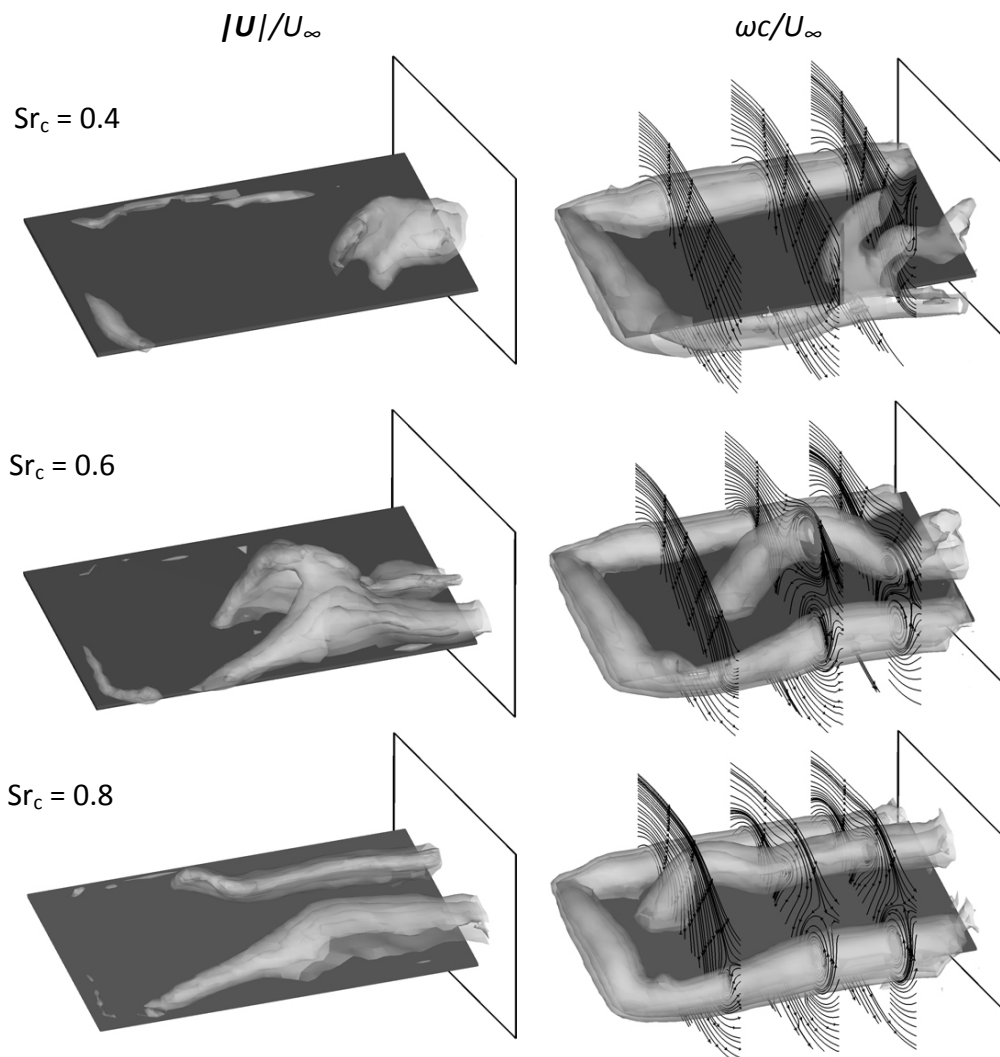
Figure 29: Isometric views of iso-surfaces defined by constant velocity magnitude ($|U|/U\infty = 0.15$, 0.3 and 0.45) and vorticity magnitude ($|\omega*| = 7$, 15 and 25), superimposed by streamlines at three separate spanwise locations. Measurements are presented for the phase when the wing is at the botton of the motion. sAR=2 wing with flat plate cross-section, $Re = 20{,}000$, $\alpha = 20°$, $a/c = 0.15$.
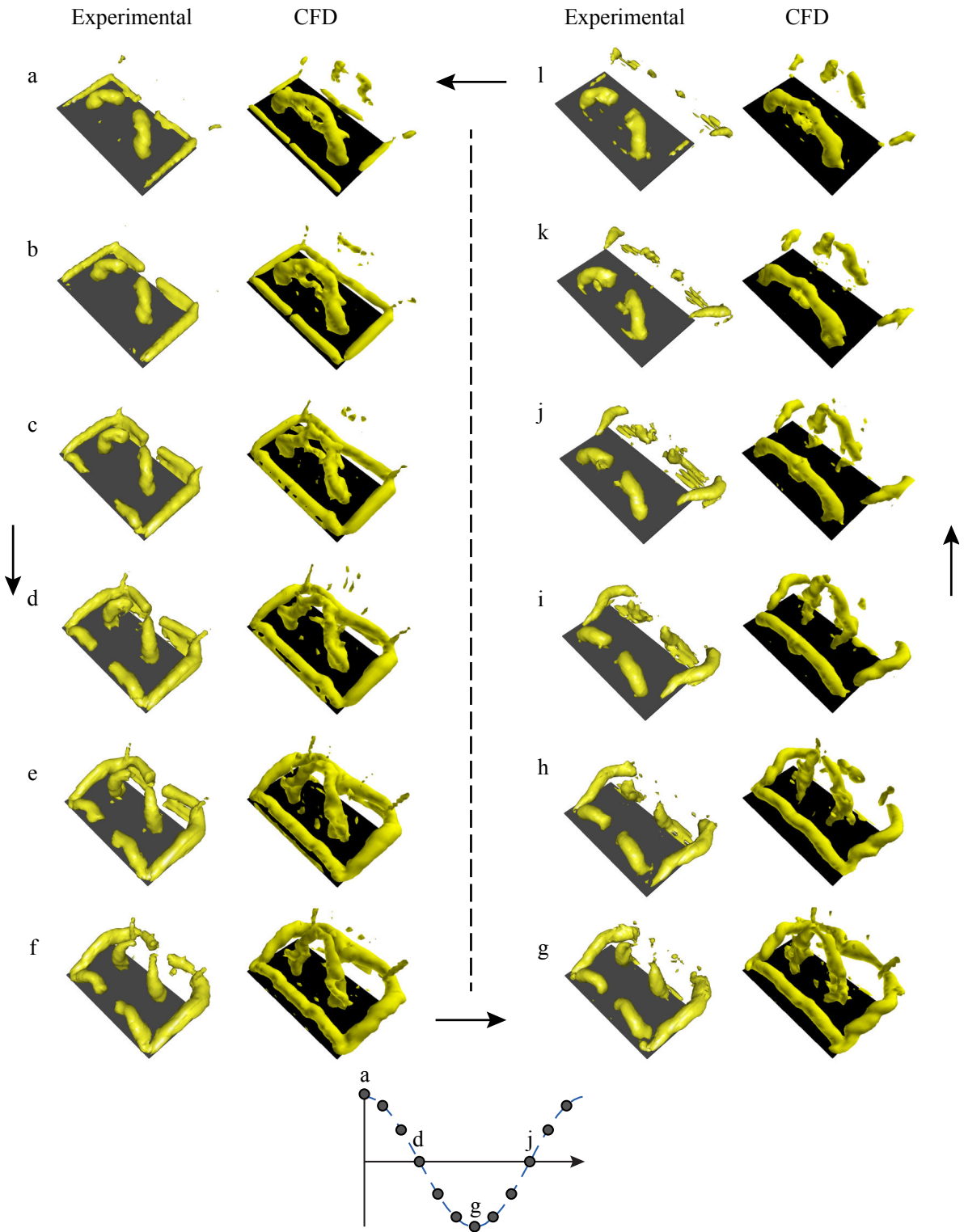
Figure 30: A twelve-phase comparison between CFD and experimental results, for the $sAR = 1$ rectangular wing (with flat-plate cross-section) at $Sr_c = 0.65$, showing $Qc/U_\infty = 20$. $Re = 20{,}000$, $\alpha = 20º$, $a/c = 0.15$.
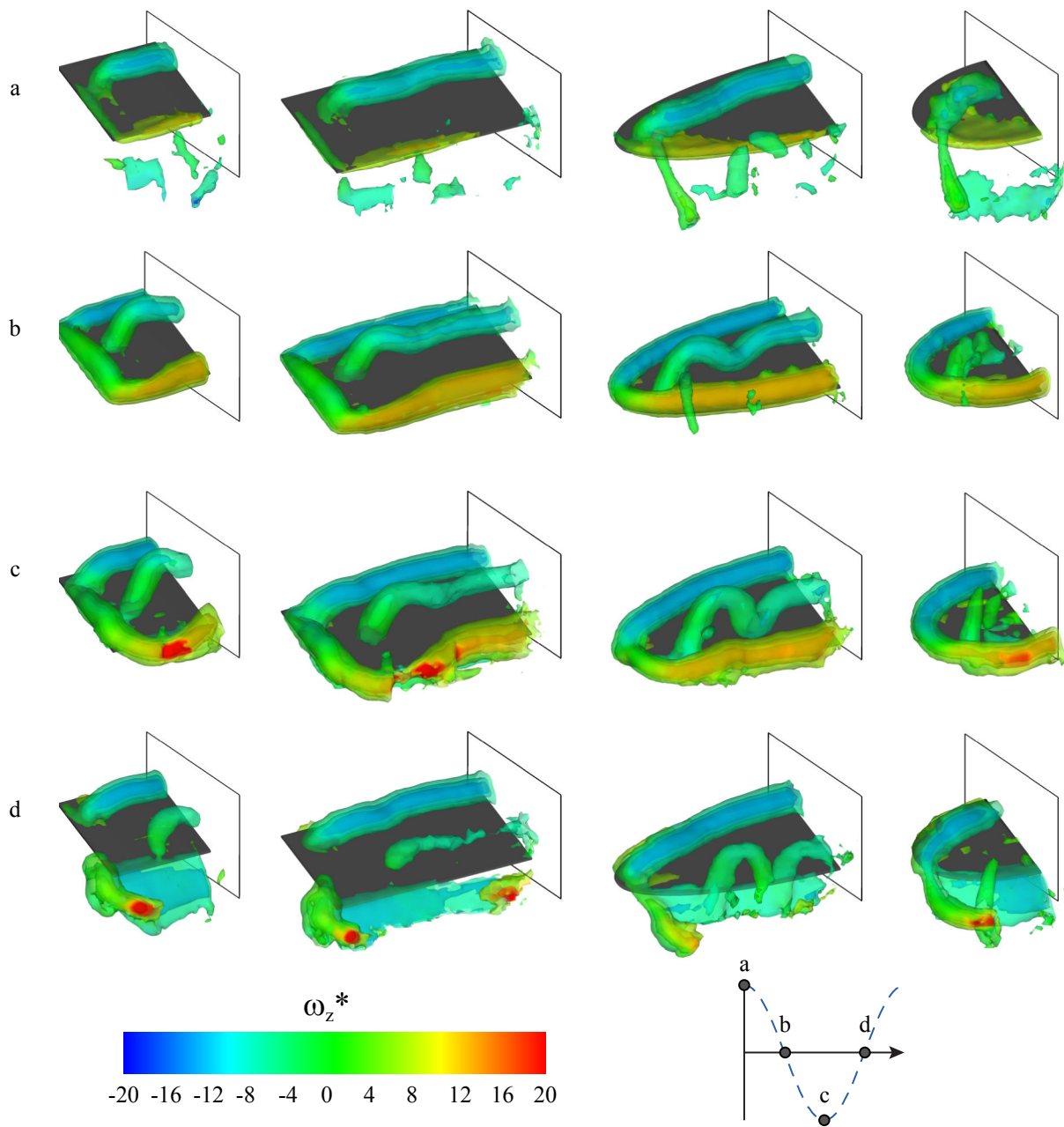
Figure 31: A comparison between different wing planforms at Sr_c = 0.8. Iso-surfaces represent constant vorticity magnitude, $|\omega*|$ =7, 15 and 25 and colour maps represent spanwise vorticity. Re = 20,000, α = 20°, a/c = 0.15.

Figure 32: Vortex core tracking for a) rectangular and b) elliptical wings, at $Sr_c = 0.75$, viewed from different angles. The wing corresponds to its location at the bottom of the cycle. $Re = 20,000$, $\alpha = 20°$, $a/c = 0.15$.
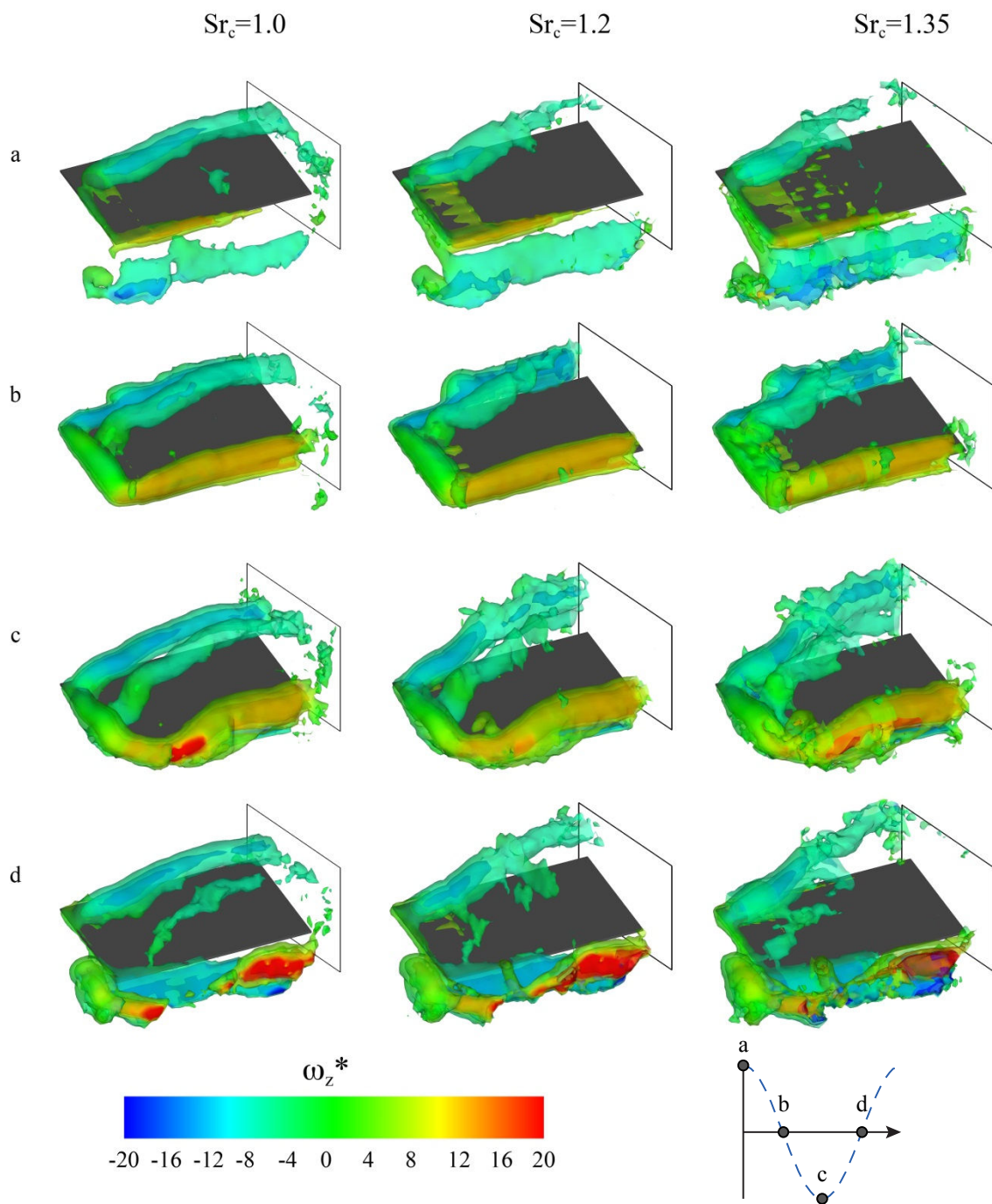
Figure 33: Isometric views of the vortices that surround the *sAR* = 2 flat-plate rectangular wing at four phases in the cycle for various frequencies, operating at *Re* = 20,000. Iso-surfaces represent constant vorticity magnitude, $|\omega^*|$ = 7, 15 and 25. $\alpha = 20º$, *a/c* = 0.15.
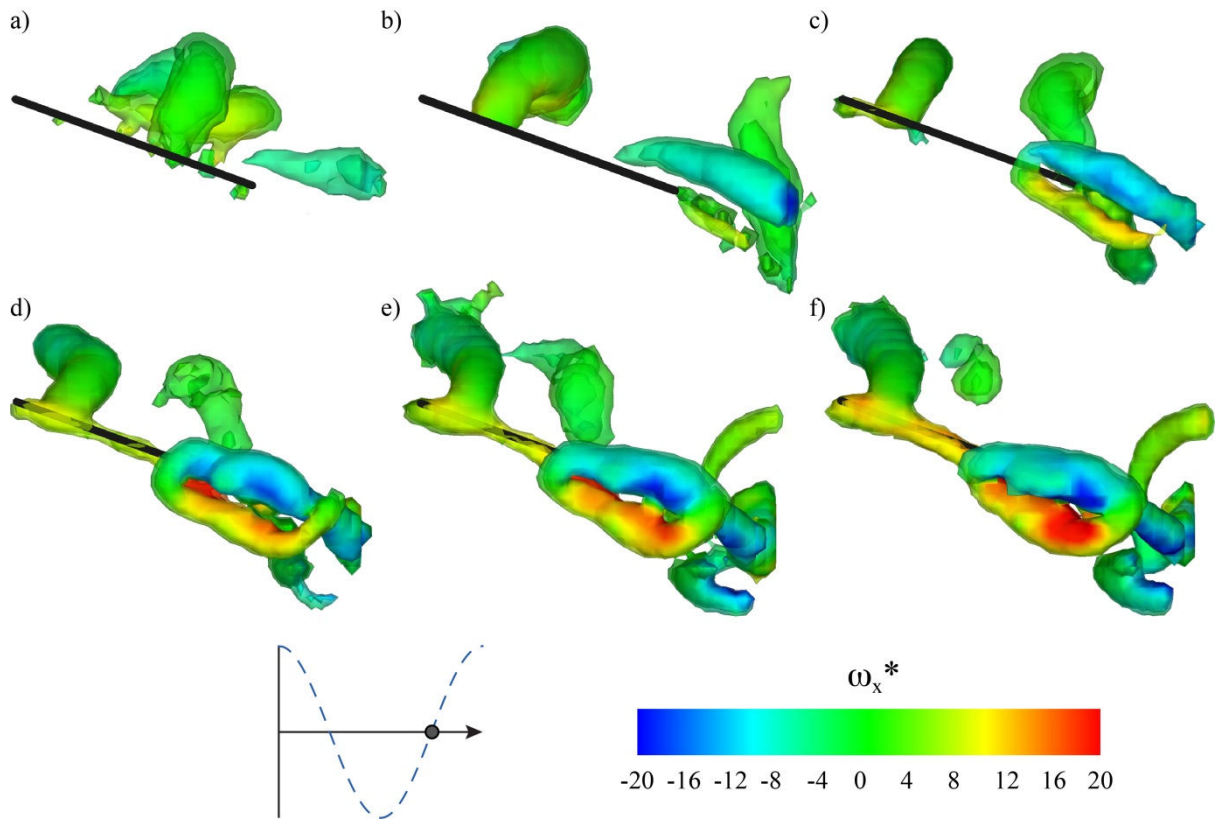
Figure 34: A side view of the Q-criterion iso-surfaces surrounding the $sAR = 1$ rectangular wing at $t^* = 0.75$ for various frequencies: a) $Sr_c = 0.4$, b) $Sr_c = 0.6$, c) $Sr_c = 0.8$, d) $Sr_c = 1.0$, e) $Sr_c = 1.2$ and f) $Sr_c = 1.35$. Iso-surfaces represent constant Q-Criterion, $Qc/U_\infty = 15$, 30 and 45 and colour maps represent streamwise vorticity. $Re = 20,000$, $\alpha = 20^\circ$, $a/c = 0.15$.
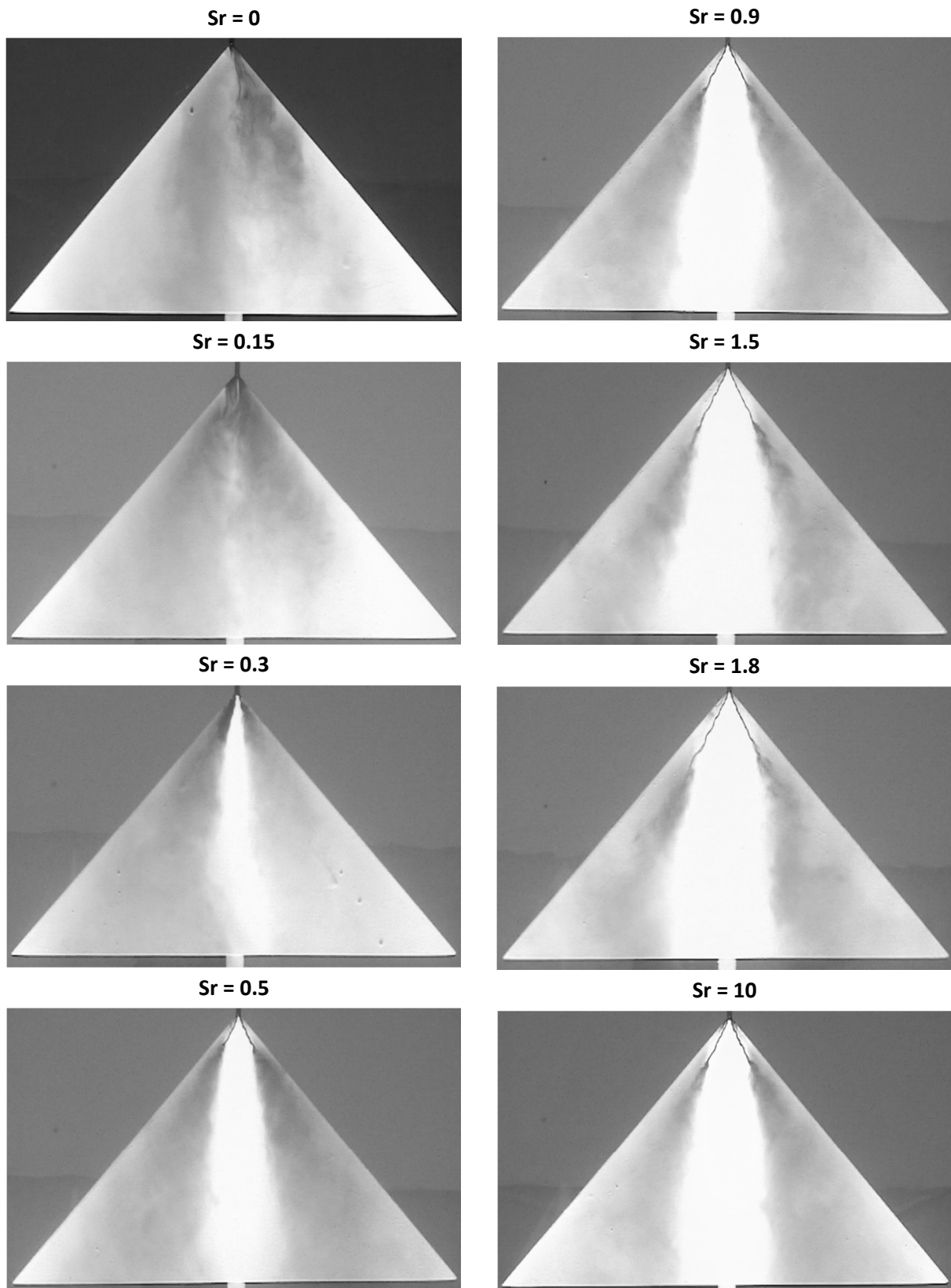
Figure 35: Flow visualization for a stationary and small-amplitude ($\Delta\phi = 5°$) rolling wing. $\alpha = 25°$, $\Lambda = 50°$.

Stationary wing   **Oscillating wing**

α = 15°

α = 20°

α = 25°
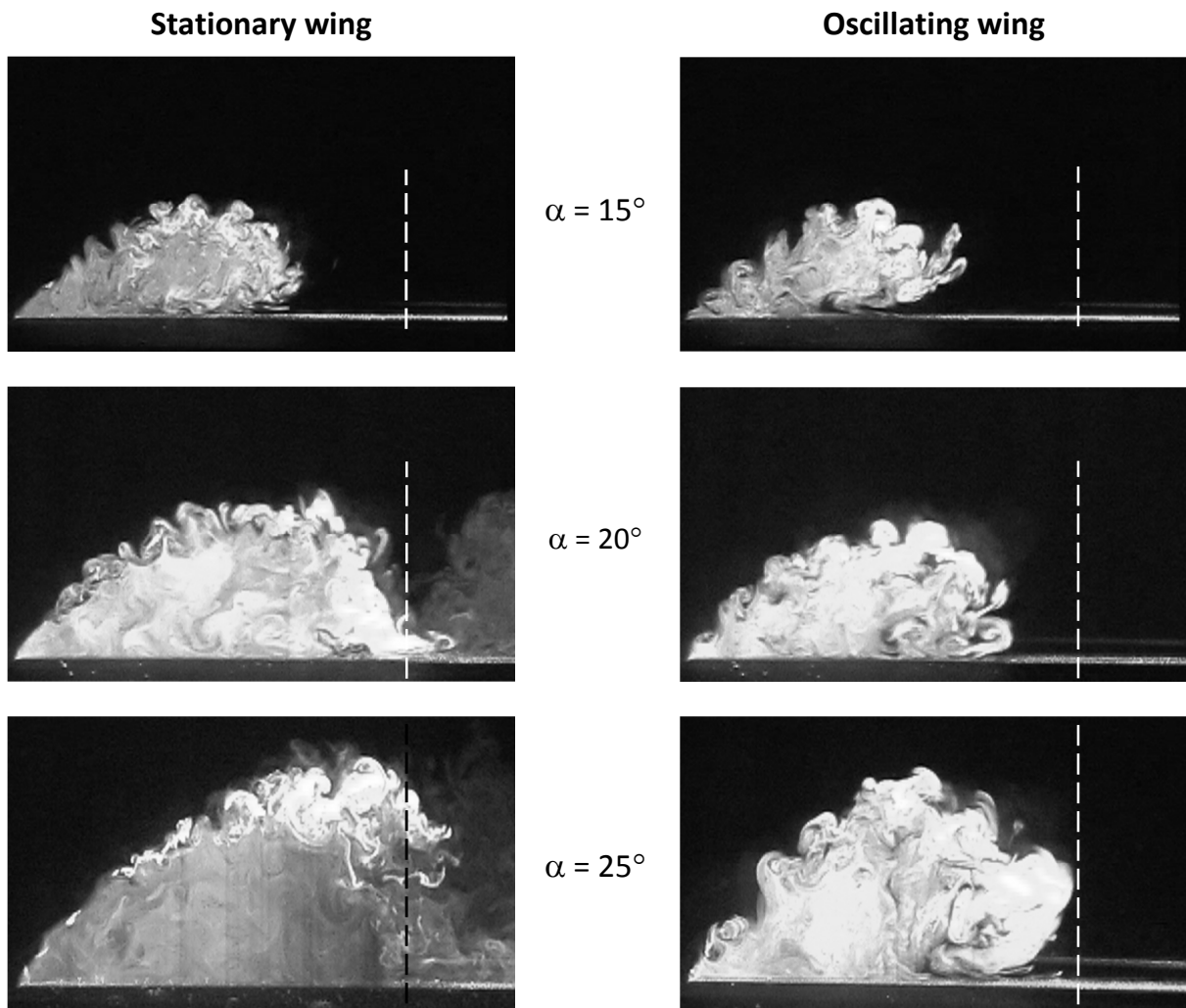
Figure 36: Laser fluorescence flow visualization for stationary ($Sr = 0$) and oscillating wings ($Sr = 1.0$, $\Delta\phi = 1°$), $\Lambda = 50°$.
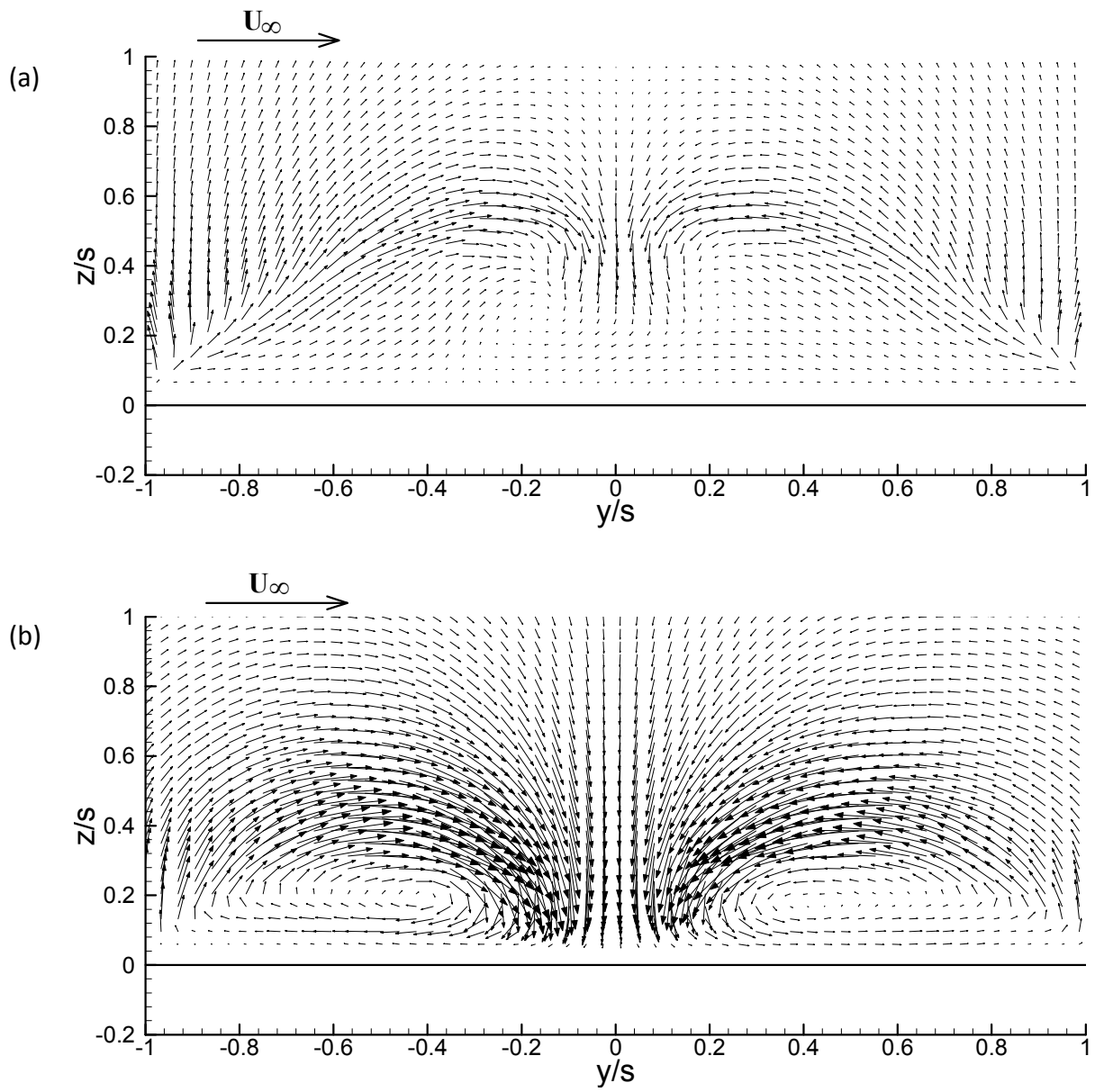
Figure 37: Time-averaged velocity field in a cross-flow plane at x/c = 0.5 for (a) stationary ($Sr = 0$) and (b) oscillating wing ($Sr = 1.5$, $\Delta\phi = 1°$). $\Lambda = 50°$, $\alpha = 25°$.
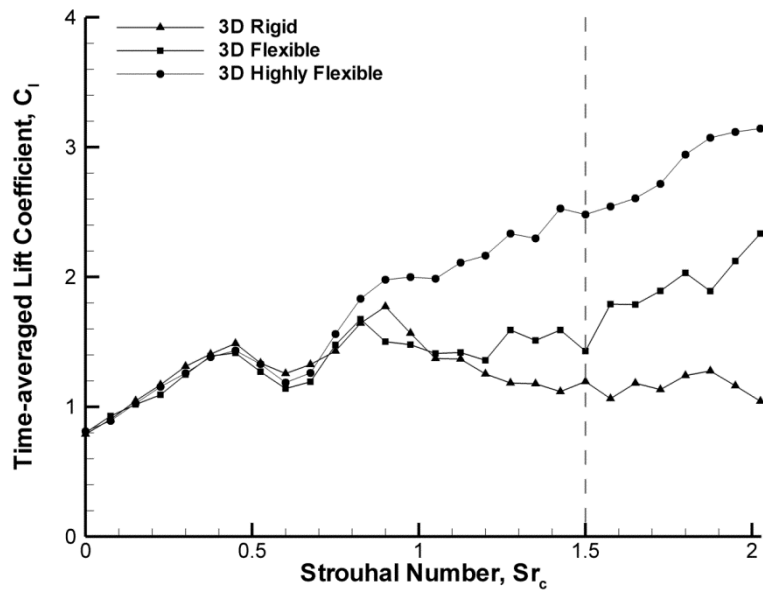
Figure 38: Time-averaged lift coefficient as a function of Strouhal number. The wing natural frequency was measured as $Sr_c \approx 2.2$ for the flexible wing and $Sr_c \approx 1.5$ for the highly flexible wing. $sAR = 3$, $Re = 10{,}000$, $\alpha = 15º$, $a/c = 0.15$.
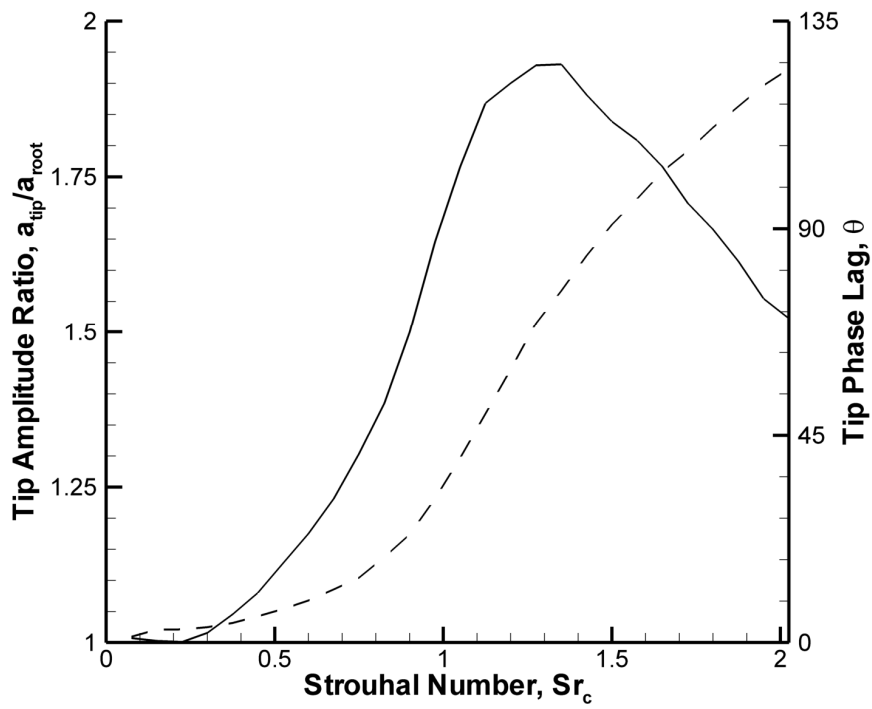
Figure 39: Tip amplitude ratio (solid line) and tip phase lag (dashed line) against Strouhal number. The wing natural frequency was measured as $Sr_c \approx 1.5$. $sAR = 3$, $Re = 10,000$, $\alpha = 15º$, $a/c = 0.15$.
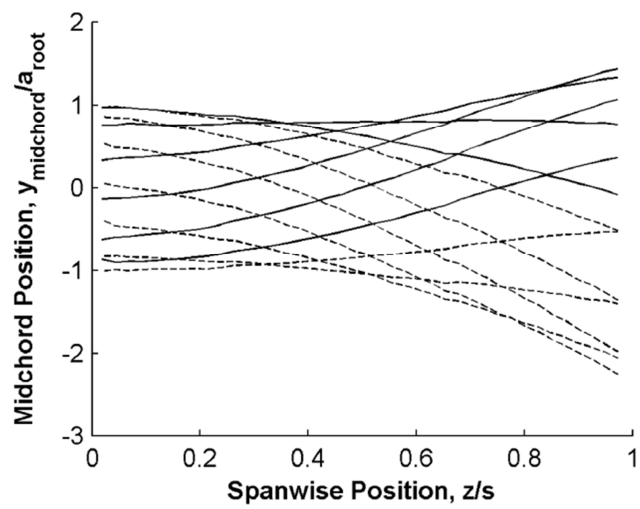
Figure 40: Midchord position of the highly flexible wing normalized by the root amplitude for ten selected instants oscillating at $Sr_c = 1.50$. Solid line is for the root moving downwards; dashed line is for the root moving upwards. $sAR = 3$, $Re = 10,000$, $\alpha = 15°$, $a/c = 0.15$.
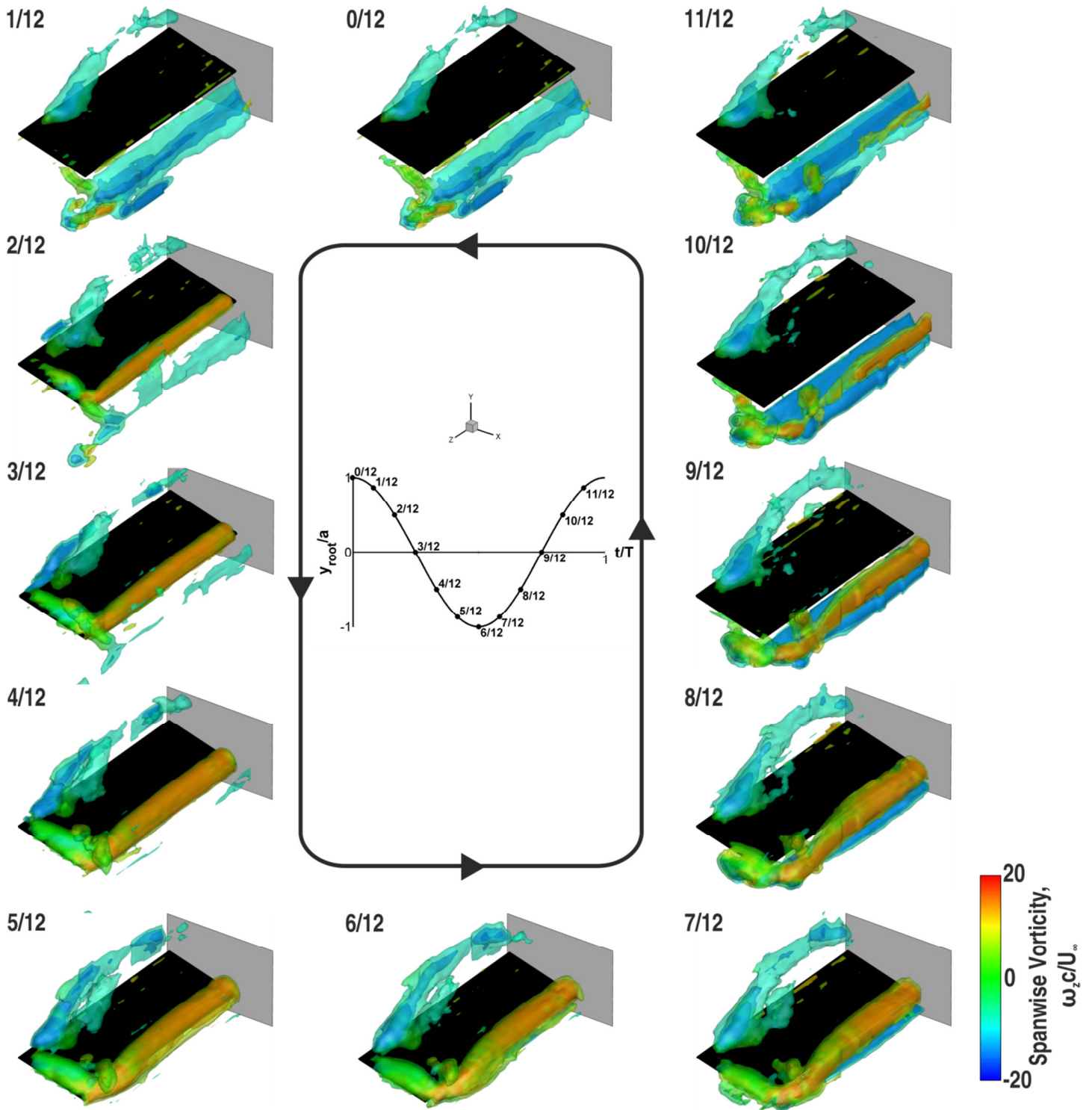
Figure 41: Isosurfaces of phase-averaged vorticity magnitude ($\omega c/U_\infty$ = 8, 16, and 24) overlaid with spanwise vorticity for the rigid wing oscillating with Sr_c = 1.50. sAR = 3, Re = 10,000, α = 15º, a/c = 0.15.
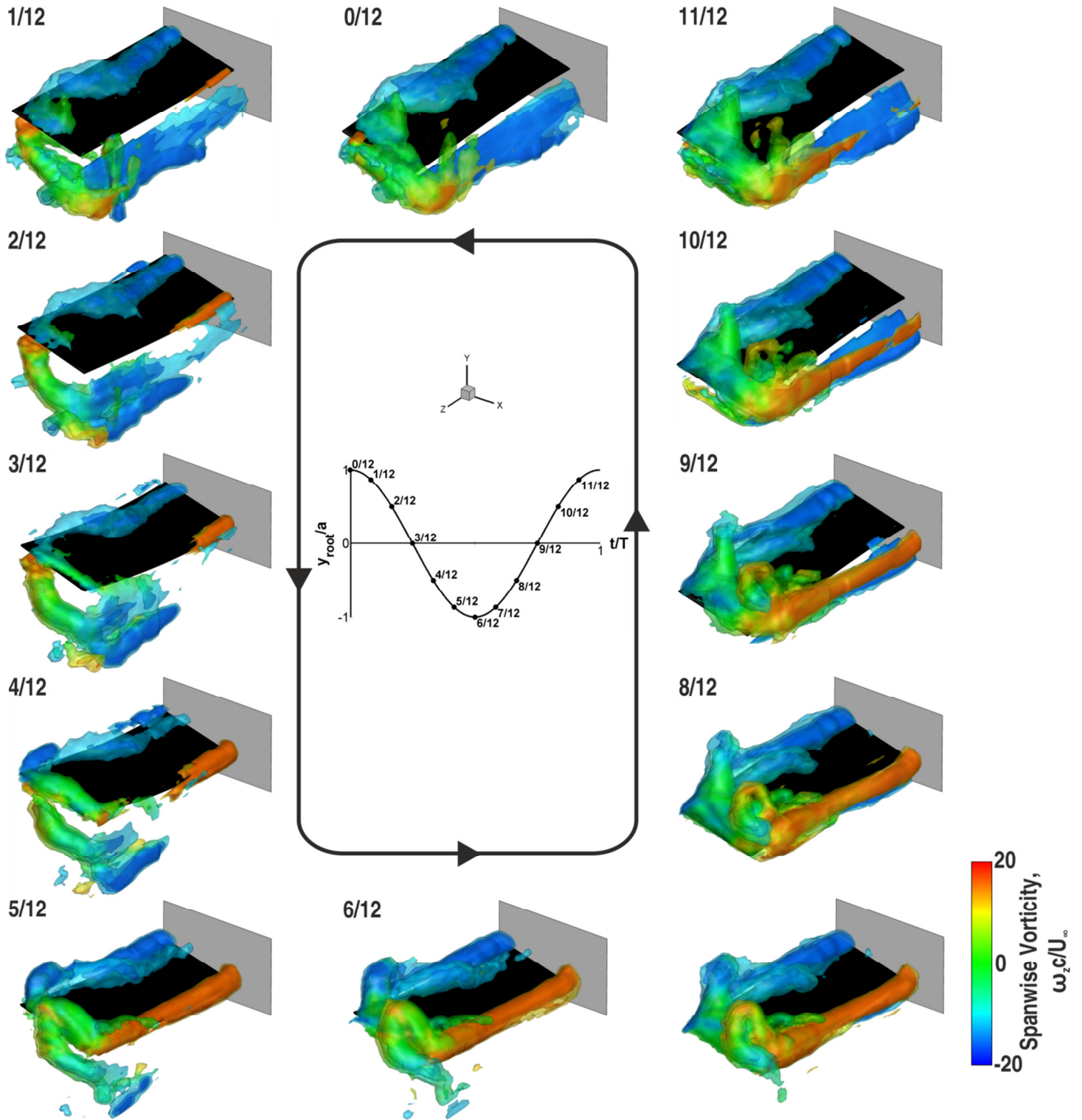
Figure 42: Isosurfaces of phase-averaged vorticity magnitude ($\omega c/U_\infty$ = 12, 18, and 24) overlaid with spanwise vorticity for the highly flexible wing oscillating with Sr_c = 1.50. sAR = 3, Re = 10,000, α = 15°, a/c = 0.15.
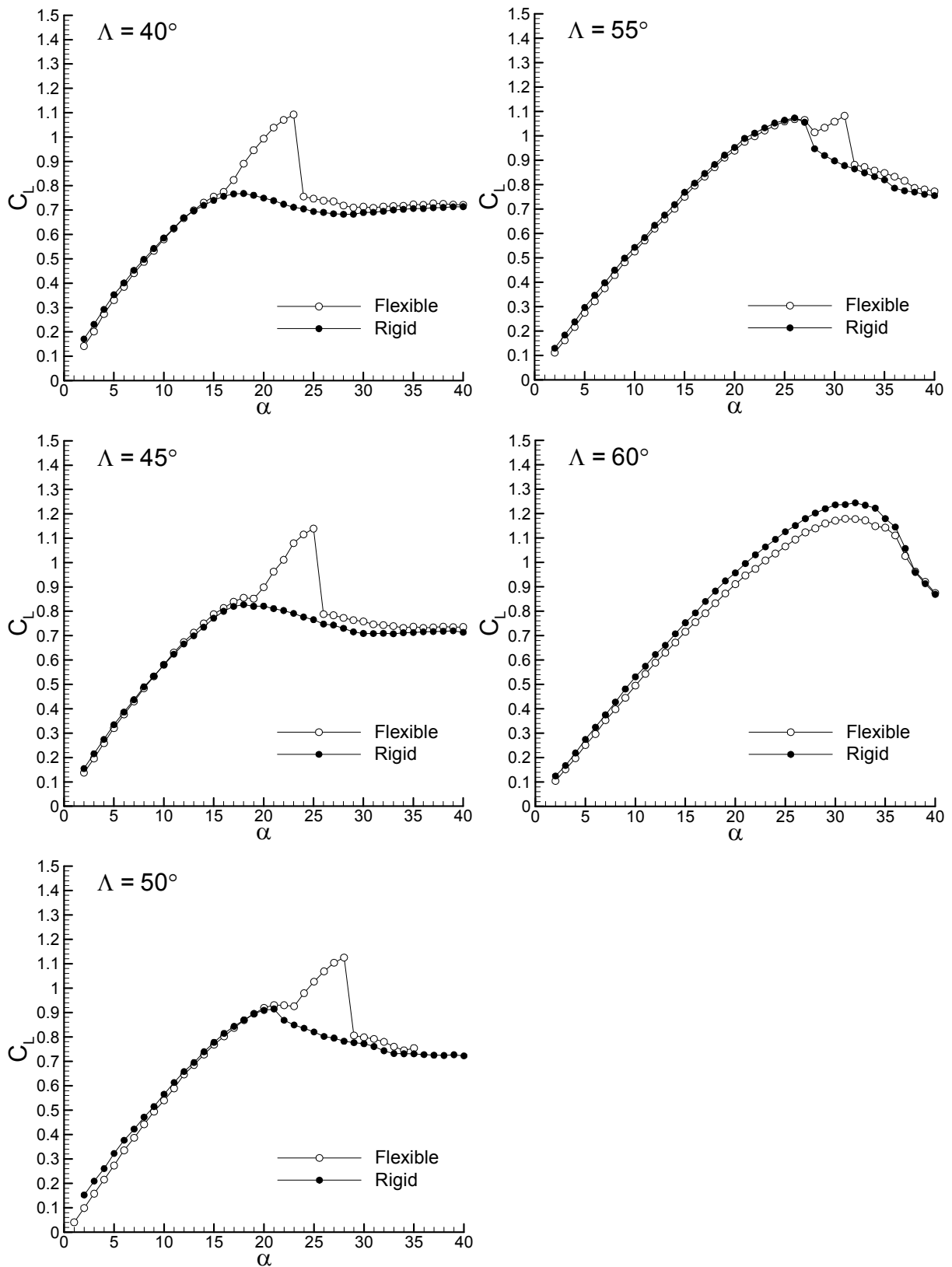
Figure 43: Variation of time-averaged lift coefficient with incidence for flexible delta wings with varying sweep angle.
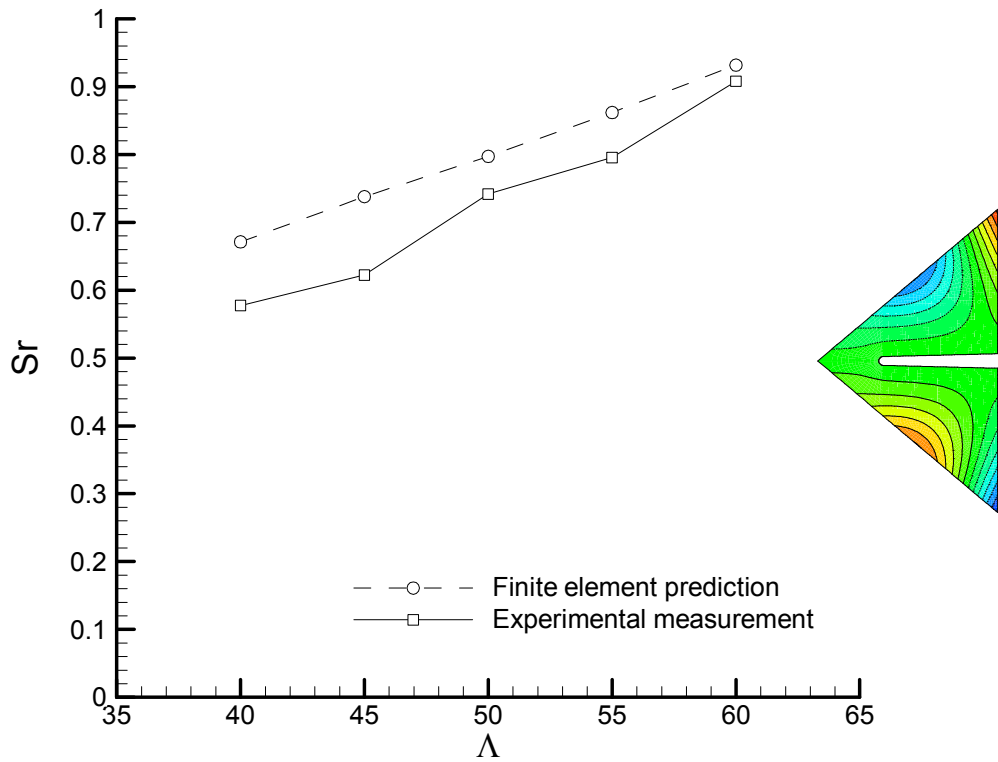
Figure 44: Comparison of Strouhal number of second anti-symmetric mode predicted by the finite element model with measured dominant frequency of wing vibrations. Inset to the right shows an example of the mode shape for a sweep angle of 50 degrees.
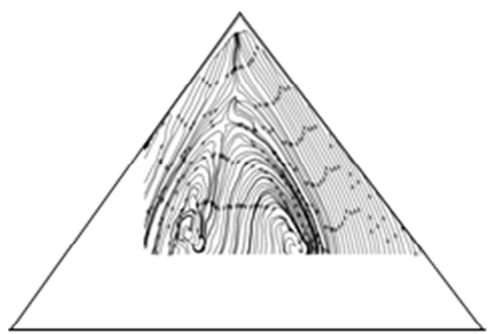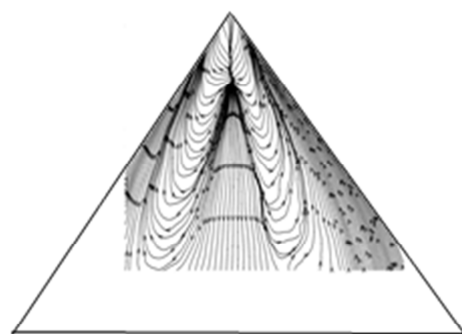
Figure 45: Near-surface time-averaged streamlines at $\alpha = 27°$ for rigid wing and flexible wing, $\Lambda = 50°$.
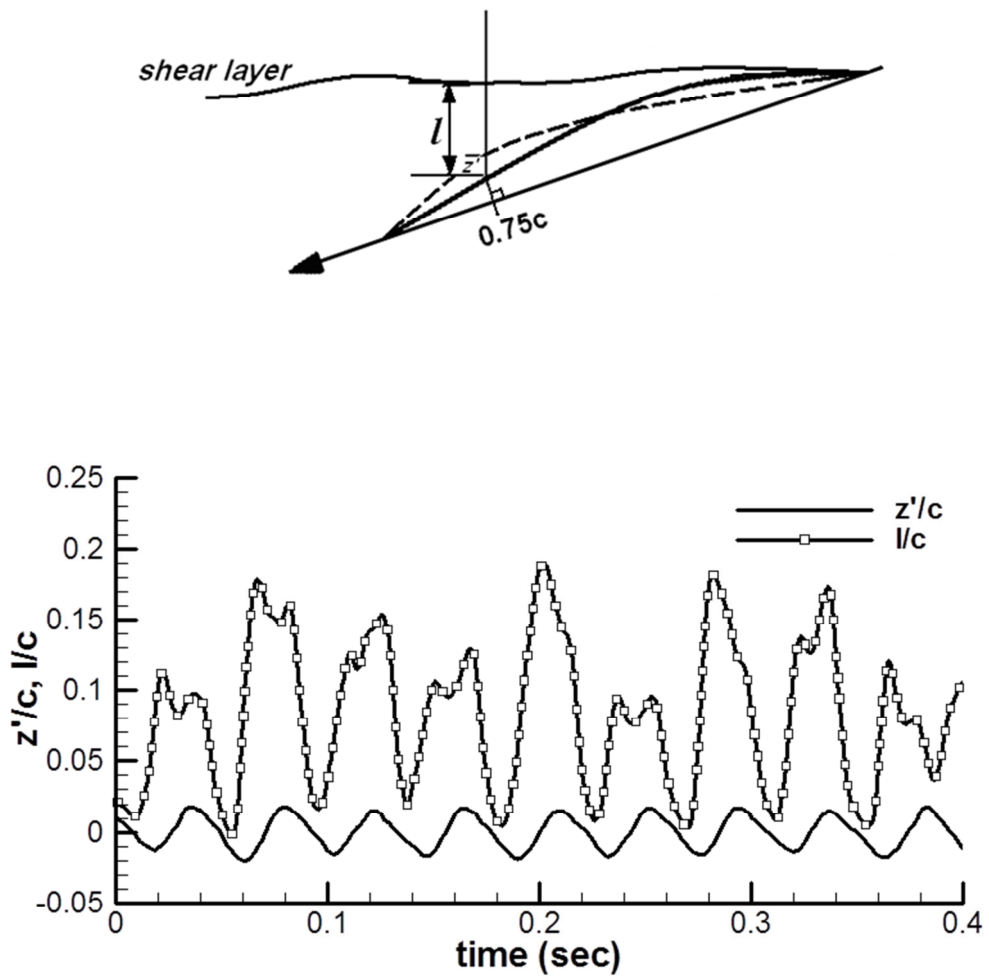
Figure 46: Time history of the locations of the shear layer and membrane as measured at 0.75c (the inset shows the definition of these quantities); U_∞=5 m/s, α = 13°. Flow is from right to left.
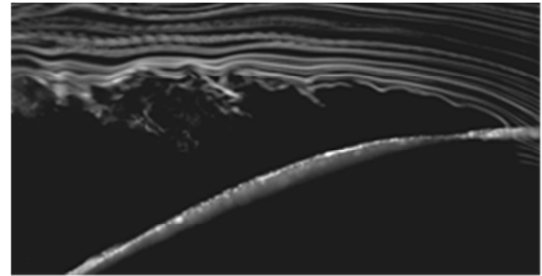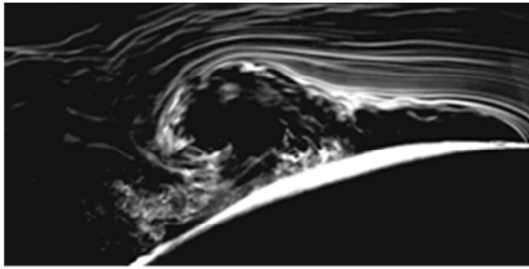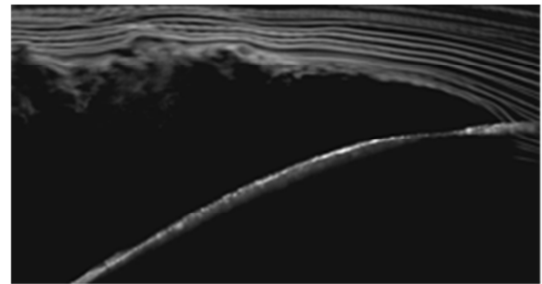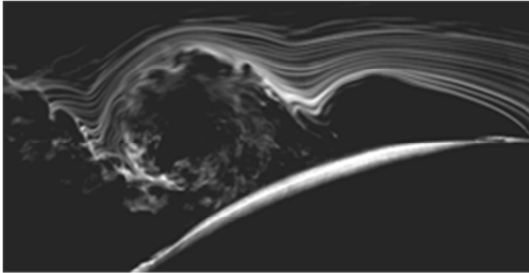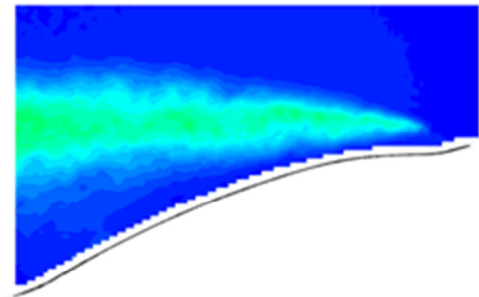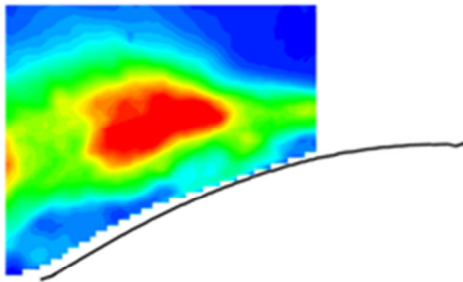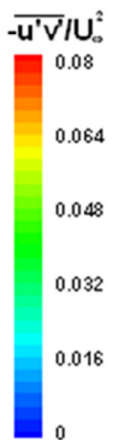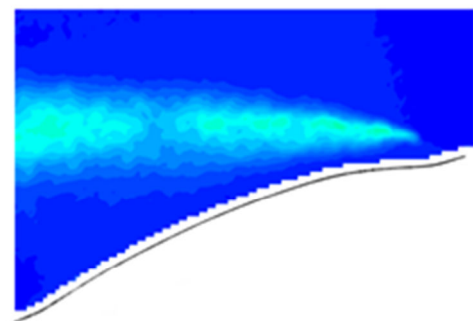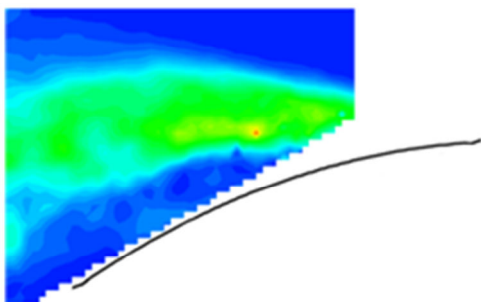
Figure 47: Smoke flow visualization at different incidences for flexible and rigid membrane (top); magnitude of the Reynolds stress for flexible and rigid membranes. Flow is from right to left. U_∞=5 m/s.
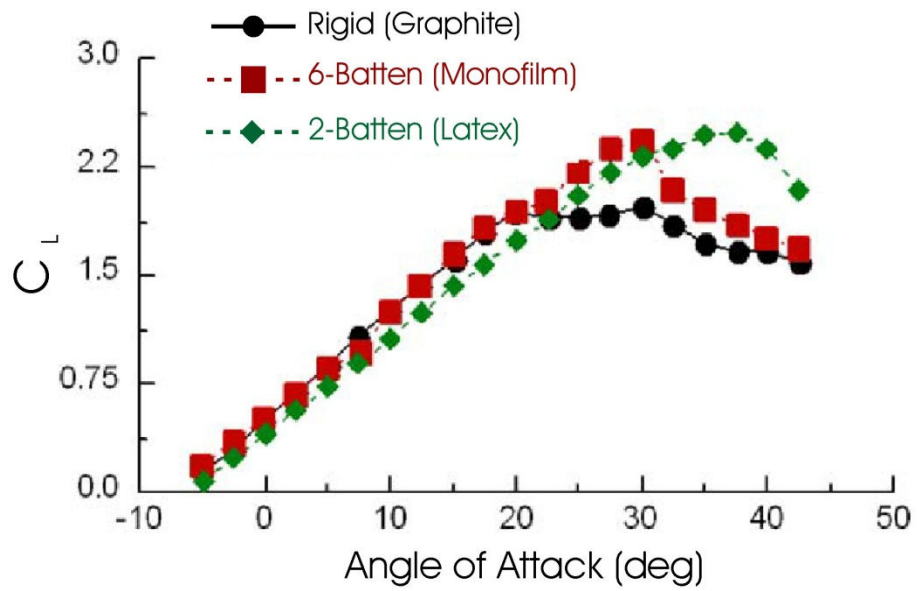
Figure 48: MAV with membrane wing (top); lift coefficient versus angle of attack (bottom) [Lian *et al*. 2003, Progress in Aerospace Sciences].
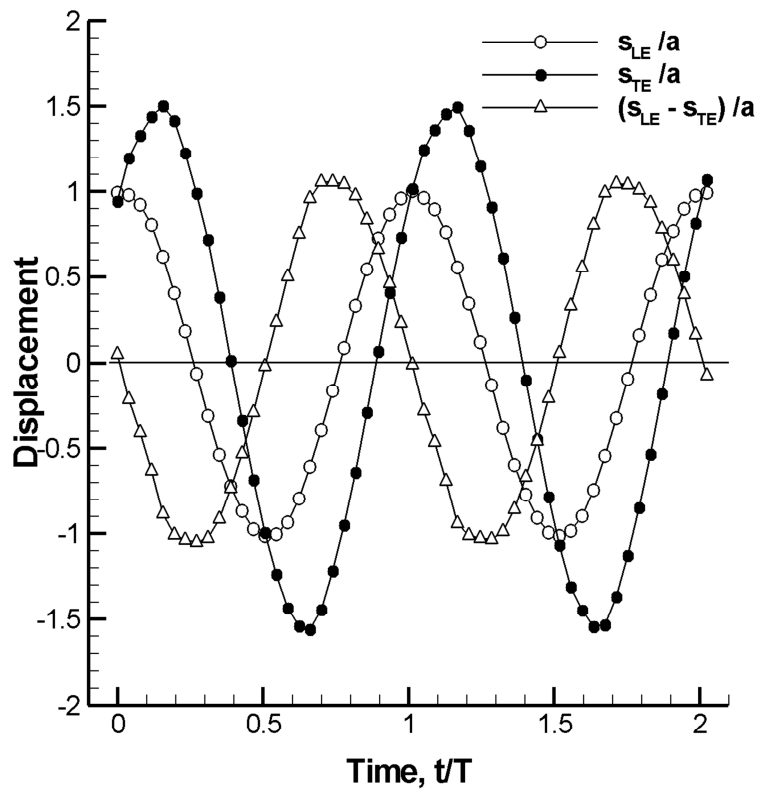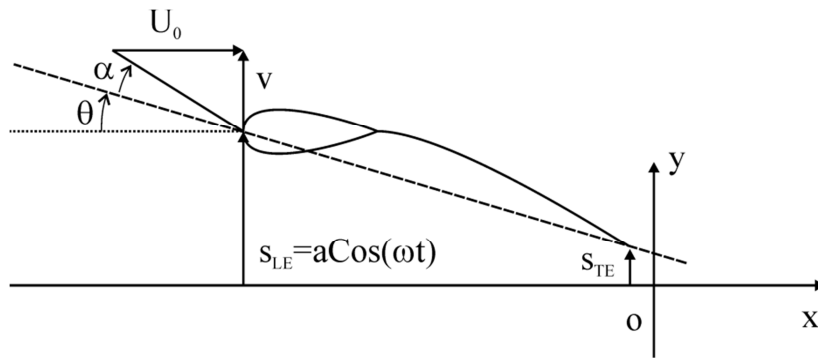
Figure 49: Schematic of the flexible airfoil heaving periodically in the vertical direction (top); leading-edge displacement, trailing-edge displacement, and deformation as a function of time; *Re* = 9,000, *Sr* = 0.34 (bottom).
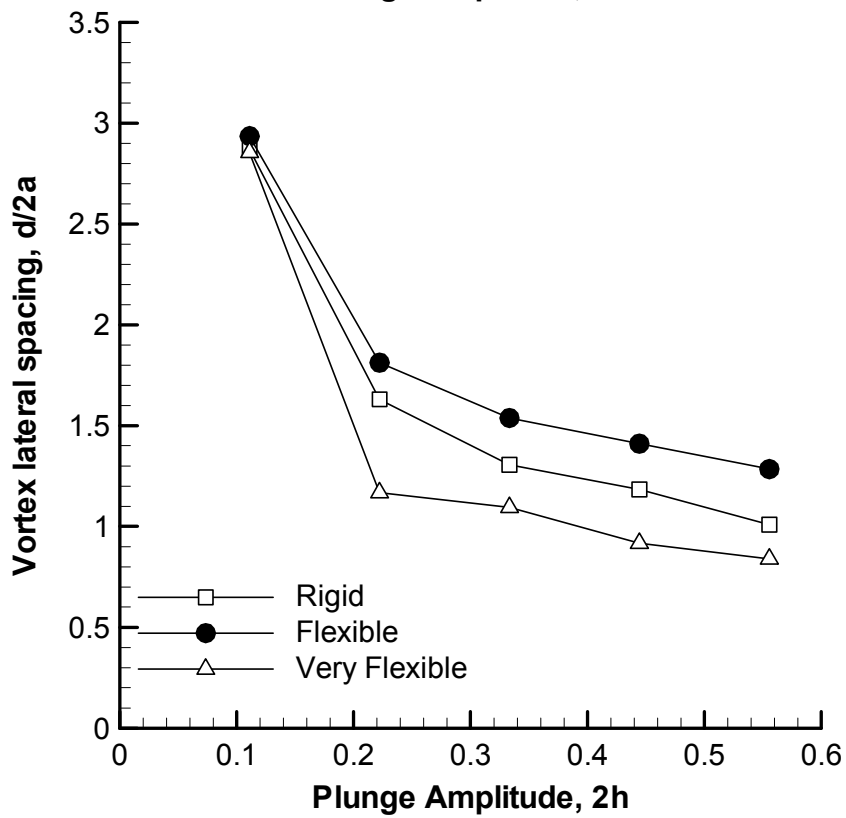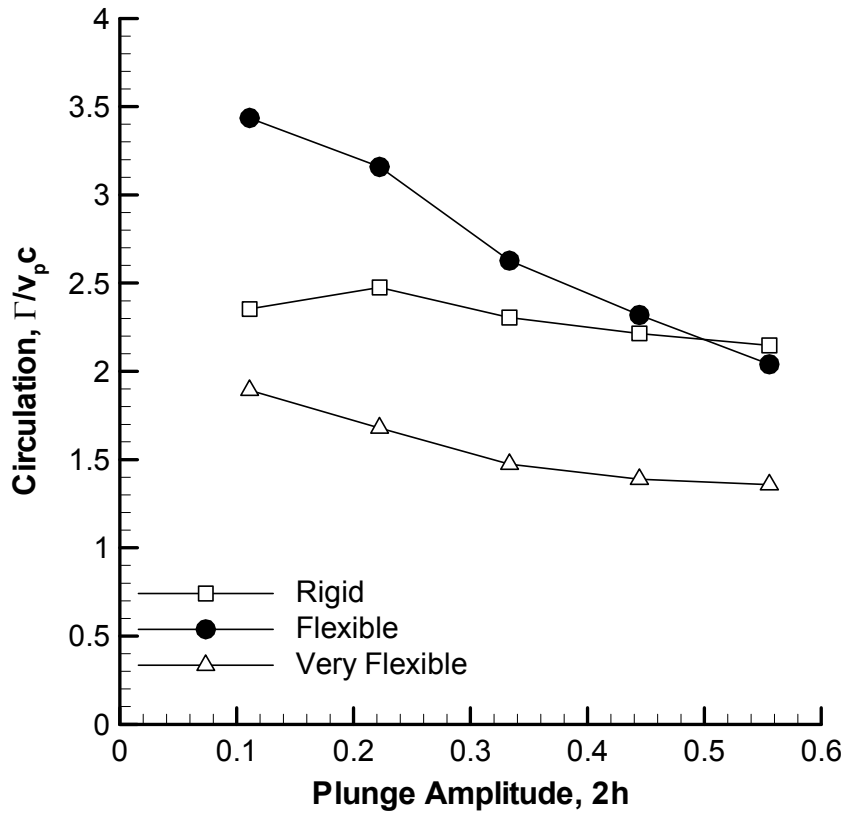
Figure 50: Variation of normalized circulation and lateral vortex spacing as a function of plunge amplitude; zero free stream velocity, Reynolds number based on plunge velocity is *Re* = 16,200.
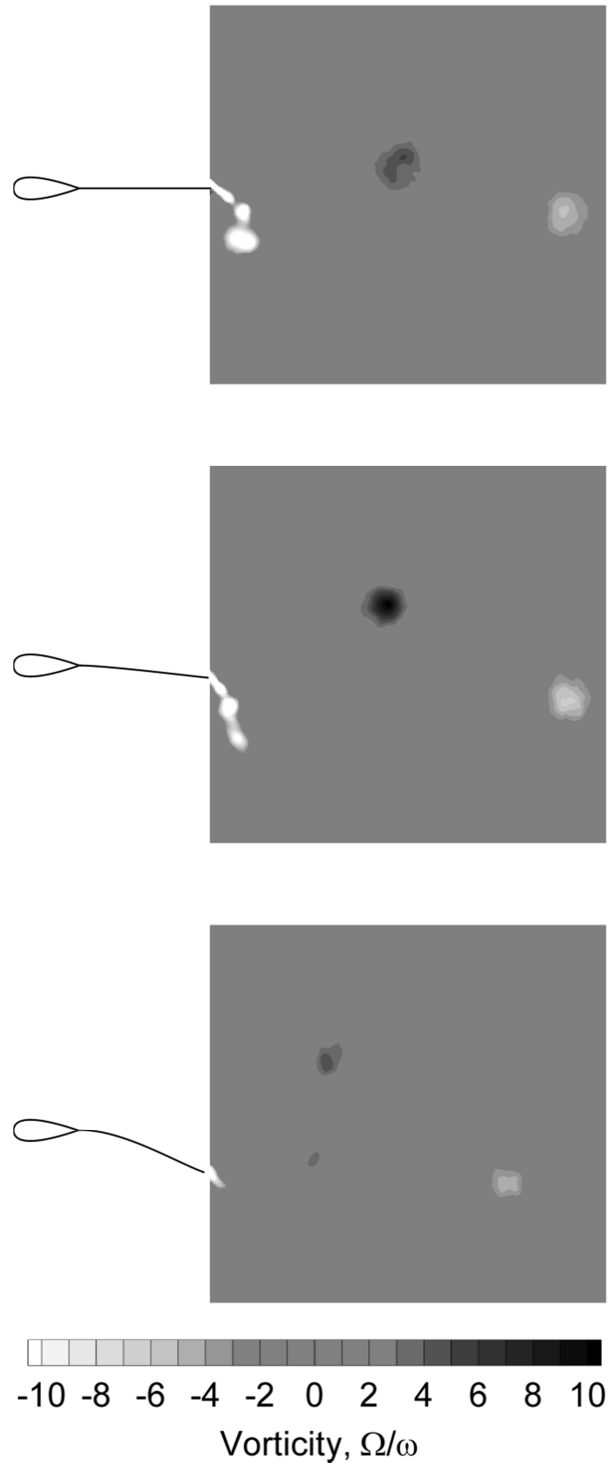
Figure 51: Phase-averaged vorticity fields for three airfoils; *Re*=18,000, *Sr*=0.26; *t/c*=4.23x10^{-3} (top); *t/c*=1.13x10^{-3} (middle); *t/c*=0.56x10^{-3} (bottom). The thrust coefficient is greatest for the intermediate flexibility.
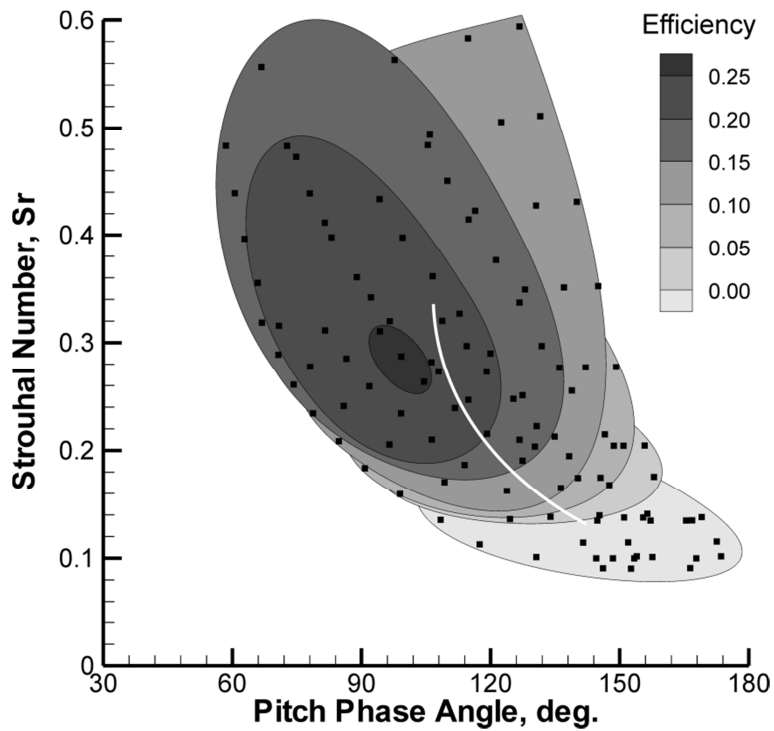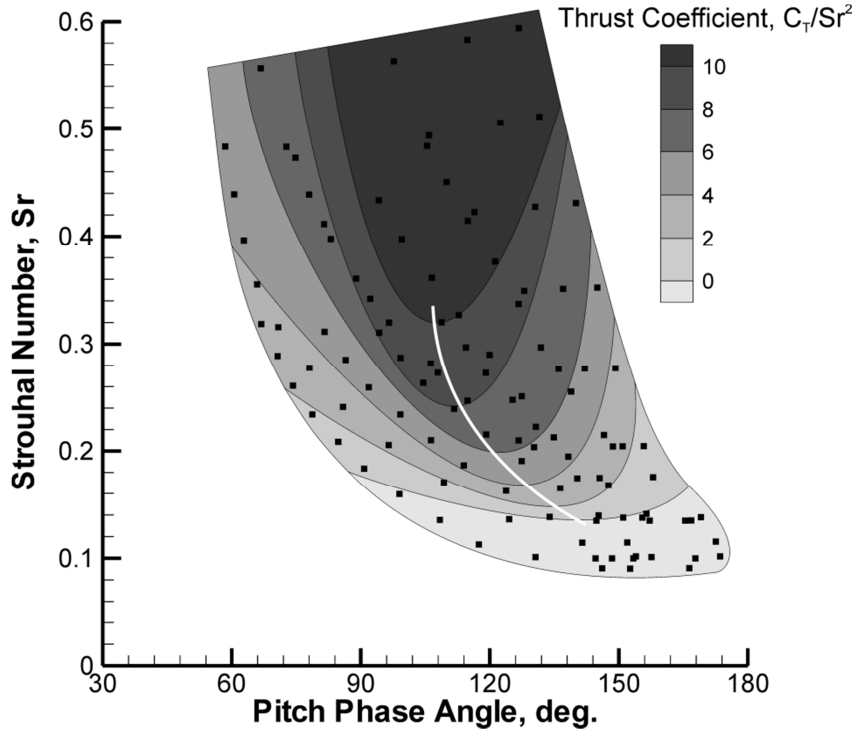
Figure 52: Contours of thrust coefficient and propulsive efficiency, in the Strouhal Number – Pitch Phase Angle plane. Black dots indicate experimental data points. The complete set of data is plotted (all stiffnesses, frequencies and Reynolds numbers). The solid white line indicates the peak thrust coefficient for a given Strouhal number.
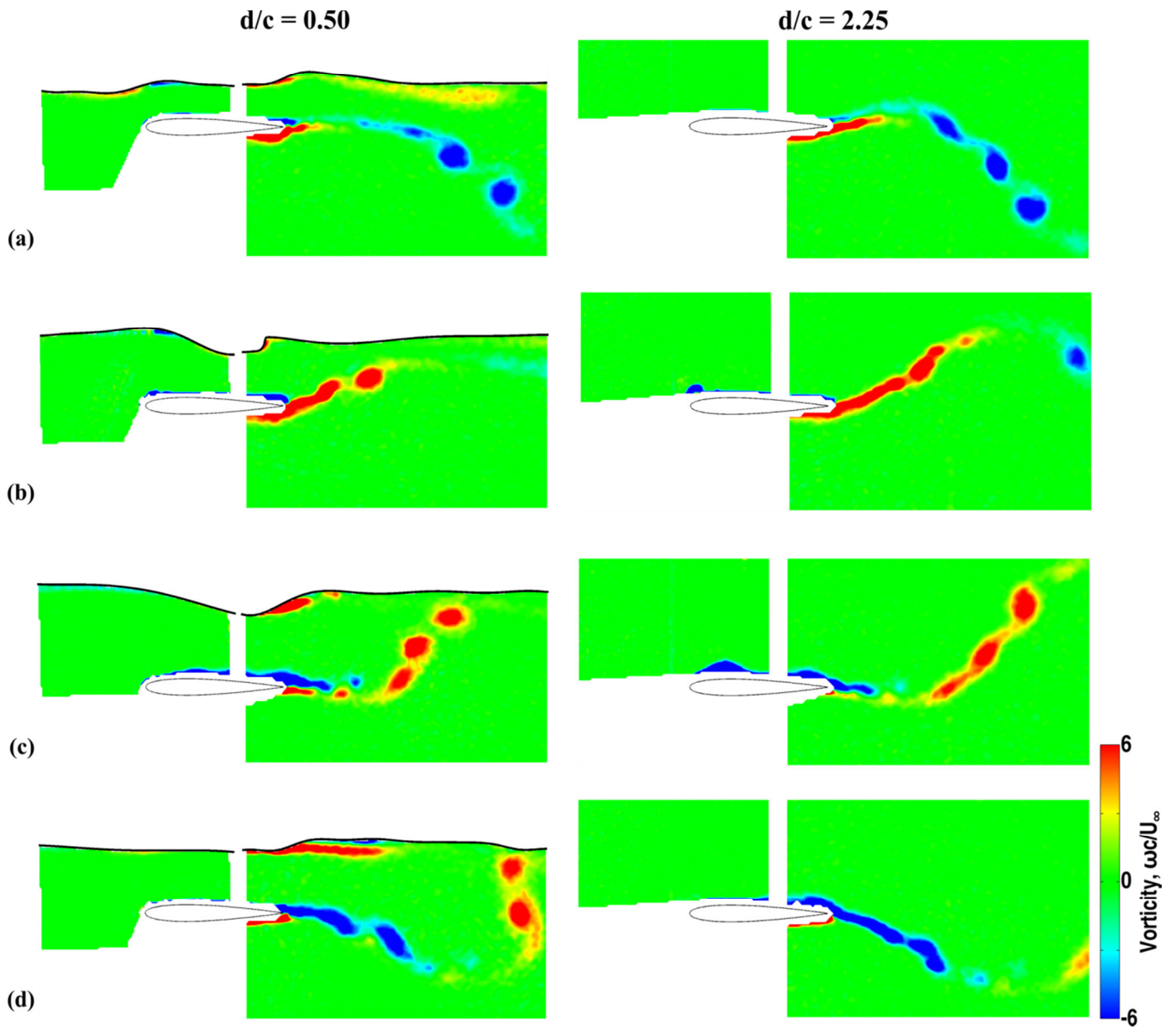
Figure 53: Phase-averaged vorticity contour plots for *a/c* = 0.20, and *Sr$_c$* = 0.30. Left column is *d/c* = 0.50 and right column is *d/c* = 2.25. **a** top, **b** middle (down), **c** bottom, and **d** middle (up) of the motion.
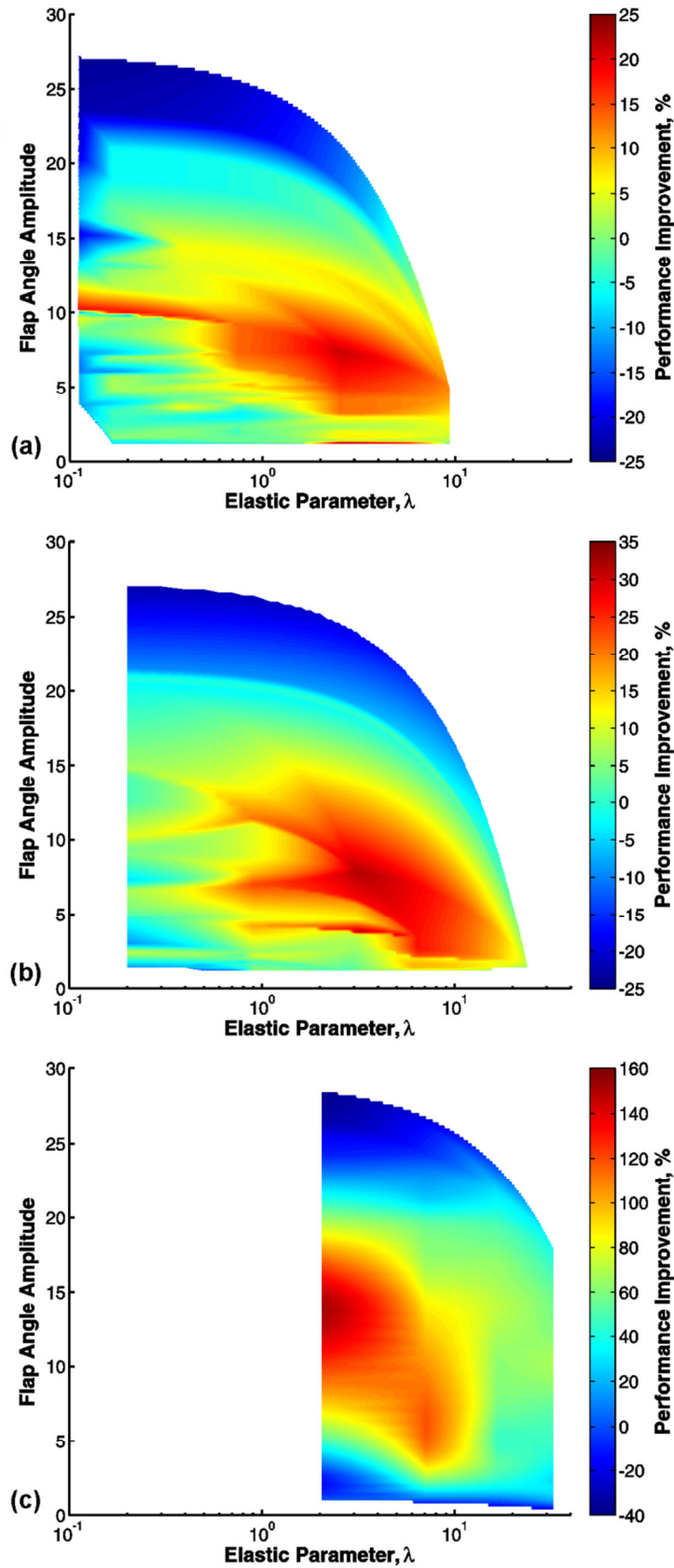
Figure 54: Inset shows schematic of the foil with flexible plate at the trailing-edge. Contour plots of performance improvement due to flexibility as a function of elastic parameter and flap angle amplitude for a) $L_{TED} = 0.2c$, b) $L_{TED} = 0.3c$ and b) $L_{TED} = 2c/3$ from Heathcote *et al*.
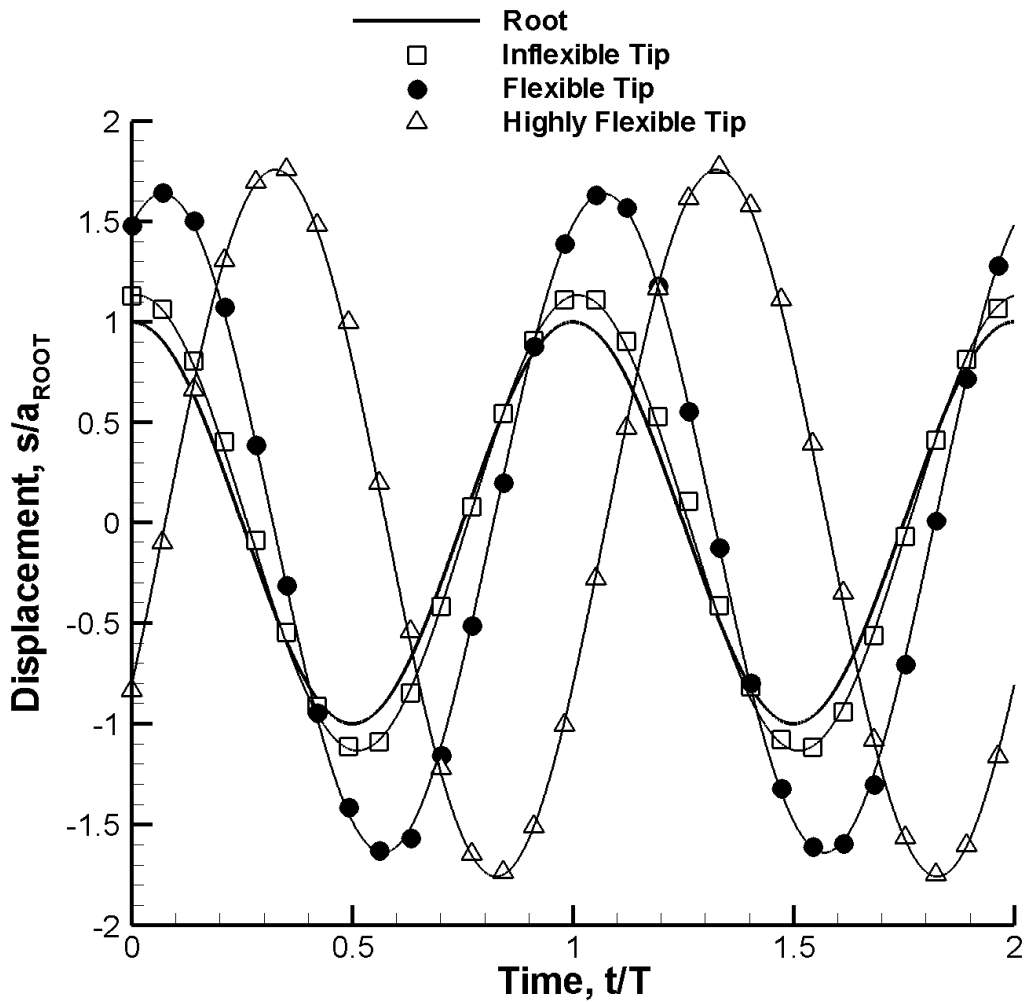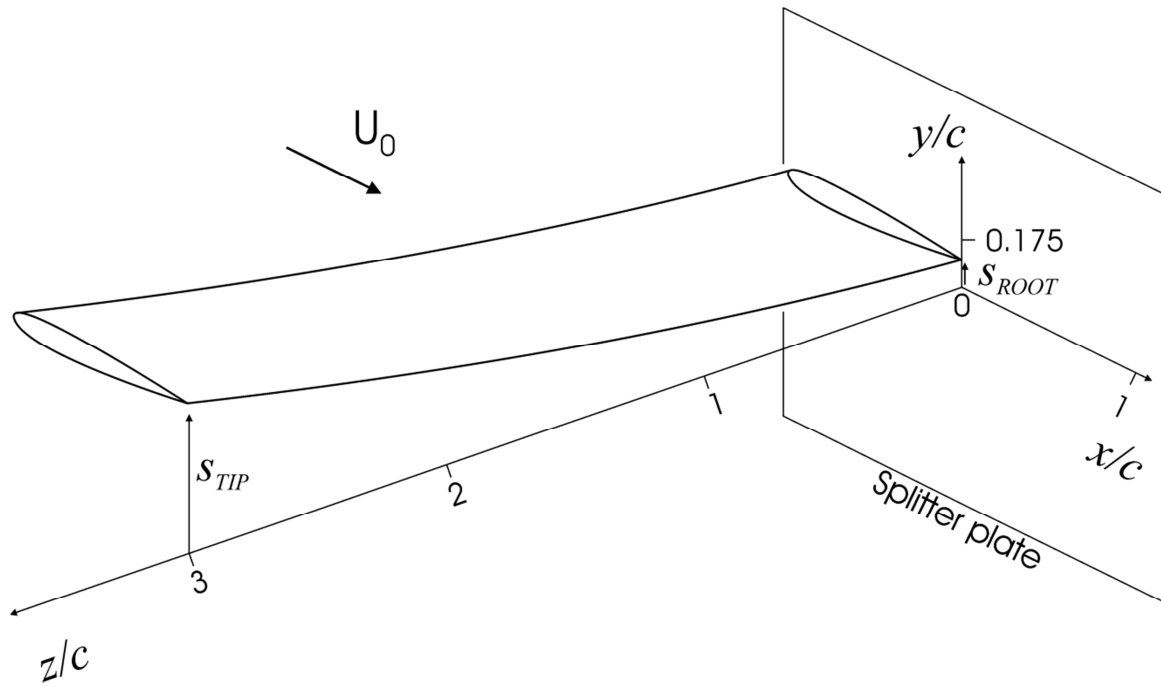
Figure 55: Schematic of the spanwise flexible wing heaving periodically (top); tip displacements for rigid, flexible and highly flexible wings as a function of time, Re = 30,000, k_G=1.82 (bottom).
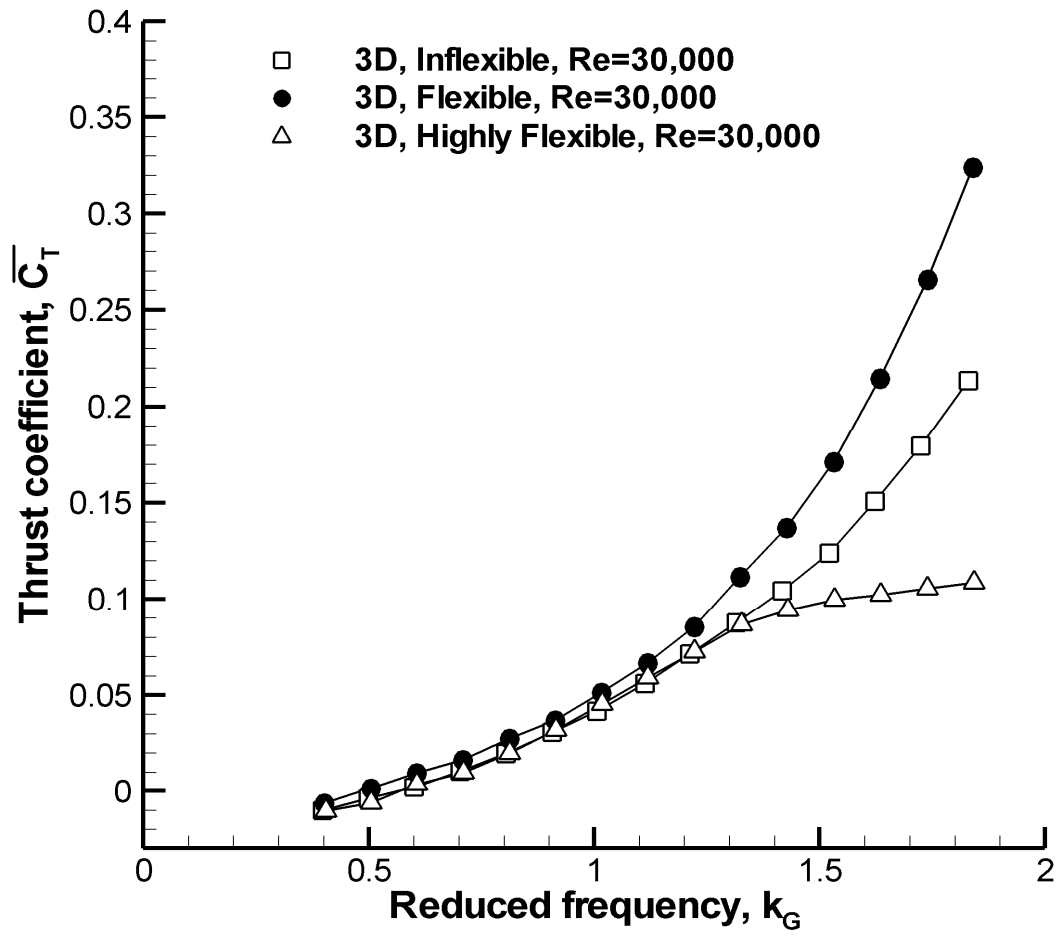
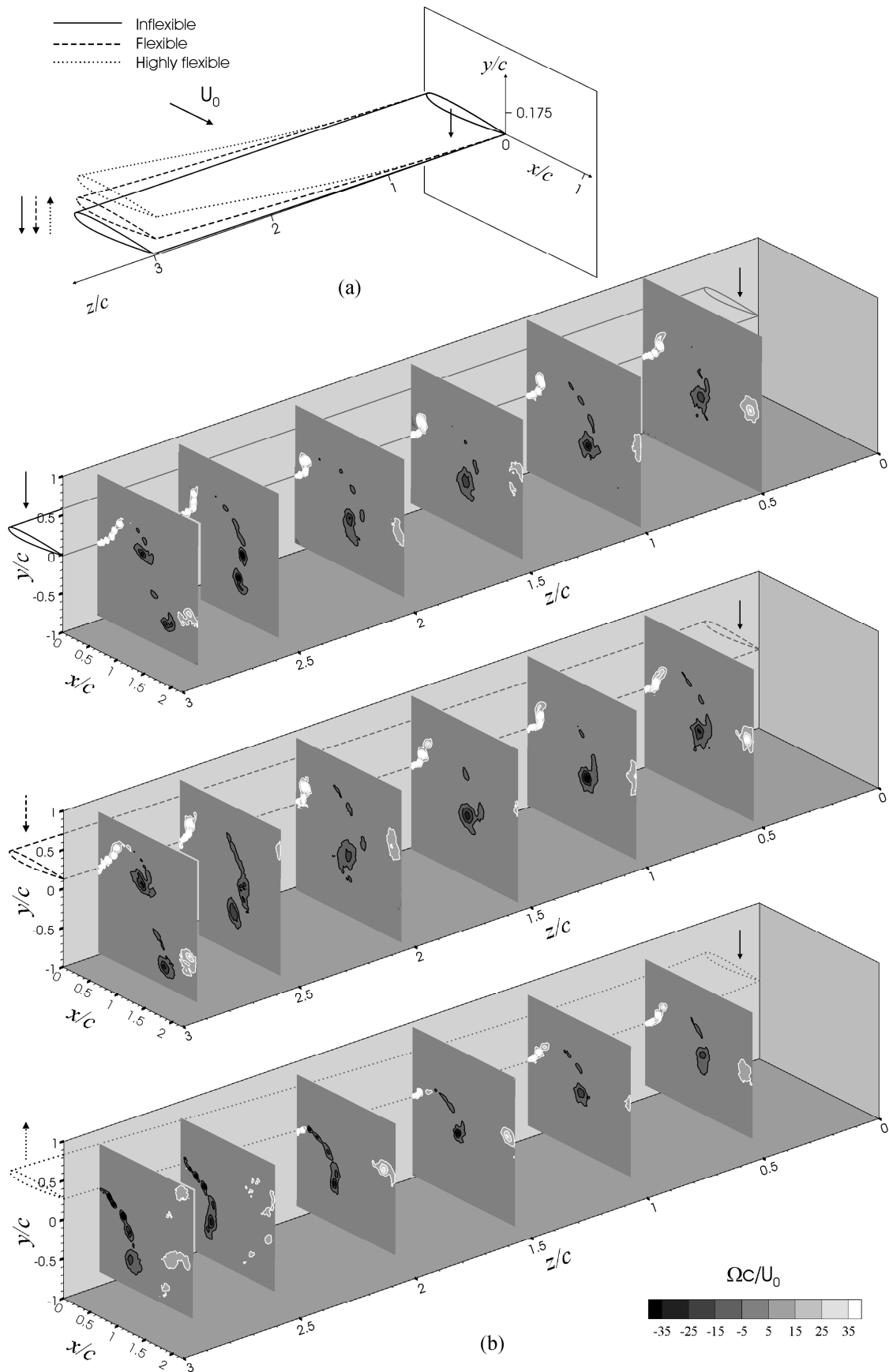Figure 56: Thrust coefficient as a function of Garrick frequency, *Re* = 30,000.

Figure 57: (a) Scale drawing of the Inflexible, Flexible, and Highly Flexible wings; (b) Corresponding vorticity fields downstream of the trailing edge; $Re = 30{,}000$, $k_G=1.82$, $t/T=1/4$. Dimensionless vorticity contours plotted are -35, -25, -15, -5, 5, 15, 25, 35.